Shallow Water Flow Prediction From Analysis of Multicomponent Seismic Data

A Research Report To The U.S. Minerals Management Service

Alan R. Huffman, Seismic Imaging Technology Center, Conoco Inc.
John P. Castagna, School of Geology and Geophysics, University of Oklahoma
Surinder K. Sahai, Seismic Imaging Technology Center, Conoco Inc.
V. Dale Cox, Seismic Imaging Technology Center, Conoco Inc.
Kevin Smith, Seismic Imaging Technology Center, Conoco Inc.
David W. Bell, Seismic Imaging Technology Center, Conoco Inc.

EXECUTIVE SUMMARY

Shallow Water Flows (SWF) are recognized as one of the primary hazards to deepwater drilling operations in the Gulf of Mexico. These hazards have cost the oil industry an estimated $200MM in the last few years. As such, SWF represents a major barrier to the success of deepwater exploration, appraisal, and development. SWF must be managed effectively if deepwater resources are to be brought to market without significantly increased cost and risk.

This report describes the results of a technical evaluation of the potential for using multicomponent seismic data to detect and delineate SWF hazards before drilling commences. The goal was to determine the physical properties of the shallow sediments that produce SWF events and to use these properties in seismic analysis of compressional wave and mode-converted shear wave data sets. The data selected for this study are from the Ram-Powell field in Vioska Knoll and the King Kong prospect in Green Canyon. The multicomponent seismic data were provided by PGS Reservoir Inc., and the well and 2D hazard survey streamer data were provided by Conoco Inc.

The analysis of the data was performed by Conoco scientists at Conoco's Seismic Imaging Technology Center (SITC) in Ponca City and by Dr. John Castagna at The University of Oklahoma (OU) in Norman. Detailed rock physics measurements were performed at the OU Rock Mechanics Institute and the OU Integrated Core Characterization Center in Tulsa. The results included custom reprocessing of the PGS seismic data to better resolve the shallow geology, modeling work to tie the rock physics measurements into the seismic data, and advanced inversion and AVO analysis of the seismic data to detect signatures from the SWF sands.

The results of the study reveal that multicomponent seismic data can indeed be used to detect and delineate SWF hazards in the deepwater environment. Key conclusions of the study include the following points:

1. Rock physics measurements and the resulting seismic models support the contention that SWF sands can be detected using seismic analysis.
2. The seismic data from King Kong revealed several zones where anomalous AVO and inversion signatures are believed to be related to SWF sands. These signatures are consistent with the well results and are quite robust.
3. Seismic data must be processed with a focus on the shallow geology if robust results are to be obtained from seismic analysis methods. Industry standard processing of seismic data for deeper targets is not adequate for this purpose.
4. Shear wave data gathered from multicomponent Ocean Bottom Cable surveys must be treated very carefully as the shear velocities in the shallow sediments are extremely slow and can have large static corrections and time delays associated with them.
5. Positioning of the OBC sensors must be done with significantly greater accuracy because of the slow shear wave velocities in these sediments.
6. Standard industry seismic sources may not always provide sufficient resolution to detect thin SWF hazards. Therefore, it is recommended that a second acquisition using high-frequency source arrays be deployed to assure acquisition of the high frequencies required to image SWF sands in the shallow section.
7. Future studies like this one should be planned at pre-drill locations for new wells so that unpenetrated shallow section may be analyzed and predictions can be made that will later be confirmed by the drill bit and PWD tools.
8. Improved shallow logging and core sampling information will be essential to further progress in understanding SWF as this and most other studies that have been published have all been limited by the paucity of ground truth for calibration of seismic data.

Shallow Water Flow Prediction From Seismic Analysis of Multicomponent Seismic Data

A Research Report To The U.S. Minerals Management Service

Alan R. Huffman, Seismic Imaging Technology Center, Conoco Inc.
John P. Castagna, School of Geology and Geophysics, University of Oklahoma
Surinder K. Sahai, Seismic Imaging Technology Center, Conoco Inc.
V. Dale Cox, Seismic Imaging Technology Center, Conoco Inc.
Kevin Smith, Seismic Imaging Technology Center, Conoco Inc.
David W. Bell, Seismic Imaging Technology Center, Conoco Inc.

INTRODUCTION

Shallow Water Flows (SWF) are recognized as one of the primary hazards to deepwater drilling operations in the Gulf of Mexico. These hazards have cost the oil industry an estimated $200MM in the last few years. Future occurrences have the potential to result in well failures and significant discharges of subsurface fluids into the ocean. At present, most operators choose to drill through these hazards with a modest investment in identification before drilling and mitigate the hazard at significant expense if one is encountered. The occurrence of SWF has been identified as one of the top five challenges being faced in deepwater exploration and production. According to a report from Fugro Geoservices Inc., approximately 70 percent of all deepwater wells have experienced SWF.

A method for pre-drill delineation of sands that are close to failure and thus likely to exhibit shallow water flows would be most advantageous in selecting optimal drilling locations and in developing cost-effective well plans. The current method of identifying SWF involves pre-drill hazard studies utilizing conventional and high-resolution seismic data to identify the zones that might produce SWF. The high incidence of SWF mitigation events in deepwater wells shows that the existing techniques do not provide the needed resolution or accuracy to avoid SWF.

At present, no robust seismic method for accurately identifying and characterizing these hazards exists. Operators do not have the option to avoid the hazard instead of mitigating the problem after it has started. A new seismic analysis method is required that will permit operators to avoid the hazard and decrease the risk of well failures before the well is drilled.

An accurate understanding of the physical properties and deformational behavior of shallow water flow (SWF) sands is essential to the characterization, prediction, and interpretation of these stratigraphic units using seismic data. To date, there have been very few core and log formation evaluation measurements taken in these shallow intervals because they are not of economic interest. The purpose of this report is to address what is currently known about the physical properties and rock mechanics of these very unconsolidated formations and to demonstrate how these properties can be used to identify and characterize SWF intervals pre-drill.

PHYSICAL CONDITIONS OF SWF FORMATION

SWF have been observed in water depths from 1500 to 7000 ft between the seabed and 4000 feet below the mudline. At these depths of burial, the materials are virtually unconsolidated with very high porosities and very low effective stresses. The range of confining and effective stresses for these sands can be estimated from first principles to be between 700-6500 psi and 0-1000 psi, respectively. To put this in perspective, it is valuable to consider a comparison of stress conditions in a shallow water versus a deep water case (Figure 1). In both cases, the effective stress on the formation at the mudline is zero and increases with a gradient of about 0.535 psi/ft if hydrostatic communication is maintained with the ocean water column. In shallow water, the effective stress becomes non-zero at 500 ft below sea level where the total overburden stress is relatively small. At a water depth of 4000 ft, however, the overburden stress is much larger due to the higher water column that is present. However, as long as the pore fluids are in pressure communication, the pore pressure will be increased an equal amount. Thus, the effective stress remains unchanged between shallow and deep water at the same depth below mud line. In this example case, it is possible that an SWF zone could be at a depth below mean sea level of 6000 ft and 2000 ft below mud line and exist at a confining stress of 3100 psi and an effective stress of about 1100 psi. This compares to a shallow water case (water depth of 500 ft) where the confining stress is 4750 psi and the effective stress is 3100 psi at 6000 ft below sea level. Note that the pore pressures that equate to these two cases are 2000 psi for the deep water case and 1650 psi, or a difference of 350 psi, at the same depth relative to sea level. Thus, not only are the sediments in the deep water case less compacted, but they are at relatively higher pore pressures for the same depth below sea level.

In addition to the change in compaction state for deepwater sediments, the severity of SWF may be exacerbated by the presence of structural hyperpressuring, also known as the centroid effect (Traugott and Heppard, 1994). The concept of structural hyperpressuring suggests that a sand body that has been positioned on a structure or slope will develop a pressure gradient that is hydrostatic, even though the gradient in the surrounding sediments is non-hydrostatic (Figures 2 and 3; Stump et al, 1998). This effect produces a condition where the up-dip limb of a sand body with large areal extent may have pore pressures that are much higher than the surrounding shales and can even approach the fracture gradient. The character of the structure (e.g., synclinal versus anticlinal) also determines the reservoir pressure to some extent as shown in Figure 3. For the shallow burial conditions in which SWF occur, the amount of structural hyperpressuring required to cause a seal failure is not very great. Hence, it is easy to picture a situation (Figure 4) where a sand is deposited on the slope with a large down-dip extent and then buried under a finite amount of overburden, producing a structurally hyperpressured reservoir that will result in SWF when penetrated.

PHYSICAL PROPERTIES

To understand the physical properties of SWF sands, one must consider the deposition and burial process. Sands and shales are deposited on the sea bed in a form that resembles a slurry more than a rock. Smith (1974) characterized the behavior of these fine- and coarse-grained sediments using Wood's equation for suspensions (Figure 5). As the materials are buried, they begin to

deviate from the Wood's equation and become load-bearing materials with a granular frame that develops rigidity. The porosity point where sediments begin to behave like load-bearing framework solids was termed the "critical porosity" by Amos Nur (Marion and Nur, 1989; Marion et al., 1992; Dvorkin and Nur, 1996; Nur et al., 1998). This change in behavior (Figure 6) is an important transition because it also signals the point where the effective stress becomes non-zero in value. As effective stress increases, compaction causes the porosity to decrease and the material becomes more rock-like in its behavior. However, the slower rate of increase in the effective stress in deep water conditions also causes the rate of compaction to decrease, causing these materials to have a relatively higher porosity than a shallow water material at the same depth below sea level.

An evaluation of the physical properties that are pertinent for pre-drill seismic characterization of SWF must include the compressional and shear velocities, attenuation character, and densities of the materials, as well as the strength of the sand framework under dynamic loading. A basic understanding of these properties can be estimated from first principles of compaction theory for sediments and soils and from the literature on velocity-effective stress relationships in clastic sediments. If we consider the range of confining and effective stresses under which SWF sands exist, it is recognized that these materials exist in the transition zone between Wood's equation behavior for slurries and porous load-bearing granular materials that can be modeled using Biot theory. At these conditions, the formation should show modest changes in compressional velocity with the observed pore pressure changes. In contrast, small changes in pore pressure will cause large changes in shear wave velocity (Figure 6). As the material moves very close to the critical porosity, the rigidity, or shear strength, of the material rapidly approaches zero. The combination of these two predictions suggests that the Vp/Vs ratio of these sands may change dramatically under small load changes. The predicted loss of rigidity suggests that shear attenuation through these materials may increase dramatically as pore pressure increases, causing large variation in shear attenuation as a function of pore pressure. The loss of rigidity may also be tied back to the strength of the materials and their resistance to liquefaction and formation collapse. Poisson's ratio, the modulus of rigidity and shear wave quality factor (Q or attenuation), will be highly anomalous for sands that are close to failure and prone to SWF.

Castagna et al. (1993) give empirical relationships between compressional-wave velocity (Vp) and shear-wave velocity (Vs), porosity, and effective stress for sands and sandstones (Figure 7). Below a certain effective stress there is a rapid increase in the Vp/Vs ratio (which is directly related to Poisson's ratio) and a rapid increase in shear wave attenuation with very small decreases in effective stress. This occurs because the rock rigidity is approaching zero (i.e., the sediment is becoming more like a two-phase liquid). At higher effective stresses, the rock frame is more rigid and the sediment behaves more like a solid. The region of rapid rigidity loss is a likely candidate for the occurrence of shallow water flows.

Sand-Pack Measurements

To confirm the postulations above, measurements of compressional and shear wave velocities were performed under a range of confining and pore pressure conditions appropriate for SWF problems, porosities of 32-50 percent, shale percentages of 0 and 8 percent, and a range of

frequencies using conventional ultrasonic pulse transmission techniques. These measurements were performed at the new IC^3 facility (the former BP/Amoco rock physics lab) at the University of Oklahoma in Tulsa. The measurements were completed by measuring the dry velocities on a sand pack and then back filling with brine to measure water-saturated properties. Effective stress was varied from 3750 psi to 200 psi in dry samples and down to 400 psi in saturated samples. The shear wave measurements were stopped at these two stresses, respectively, due to loss of coupling of the transducers to the sample and/or increased shear-wave attenuation, either mechanism resulting in the inability to detect the transmitted shear wave.

Clean Sand Pack Dry Results: The clean sand pack had a measured porosity of 34 percent. Frame Vp and Vs measurements were made (Figure 8) under room dry conditions so as to minimize "frame softening" discrepancies between dry and fully water-saturated measurements. The two shear-wave polarizations (S1 and S2) yield almost identical velocities. No shear wave could be detected below 200 psi.

Clean Sand Pack Water-Saturated Results: Fully water-saturated Vp and Vs measurements (Figure 9) yield similar velocities for the two shear-wave polarizations with differences probably attributable to experimental error. No shear wave could be detected below 400 psi. The two shear-wave polarizations were averaged and polynomials were fit to the compressional and shear-wave velocity-pressure dependences (with Vs forced to zero at zero effective pressure) as shown in Figure 10. The presumption is that at zero effective stress, electrochemical repulsion of sand grains will result in effectively zero rigidity and consequently near zero shear-wave velocity. The results of the measurements for clean sands (Figure 11) show that the Vp/Vs ratio responds to changing effective stress qualitatively in the way predicted by Castagna et al. (1993) but with generally higher Vp/Vs ratios at a given effective stress and with the rapid relative loss of rigidity occurring at slightly below 400 psi. It will be seen that the precise pressure at which the rapid rigidity loss occurs is highly dependent on the form of the equation used to fit the data. The polynomial fit gives a transition at higher effective stress than do logarithmic or power law fits discussed below.

Clay-Sand Mixture Results: Velocity measurements were made on mixtures of 8 percent clay and 92 percent sand (by weight) for two clay mineralogies (kaolinite and Ca-montmorillonite). The total porosity was not measured but is presumed to be in the vicinity of 32 percent as the clay is fine grained and presumably primarily fills the open pore space between sand grains. Unfortunately, the addition of even this small amount of clay resulted in complete loss of shear-waves for fully water-saturated experiments (which were repeated twice for each clay type) indicating that a small amount of clay increases shear-wave attenuation or decreases shear-wave transducer coupling dramatically. One of the kaolinite-sand mixtures yielded a very odd decrease of P-wave velocity with increasing pressure which is not understood. The montmorillonite-sand mixtures show more consistent pressure behavior and were considered most applicable for this study. All future reference to clay-sand mixtures refer to the montmorillonite results.

The fully water-saturated P-wave velocities are readily fit by a polynomial (Figure 12); however, shear-wave velocities are more problematic. The dry shear-wave velocities (Figure 13) are also

easily fit with a polynomial, yielding a shear-wave velocity of 610 m/sec at zero effective stress. This appears to be somewhat high for fully water-saturated Vs if our preconceived notion that rigidity should approach zero at zero effective stress is valid. Fluid substitution yields a reduced Vs at zero effective stress, but best polynomial fit results are obtained when the saturated shear modulus is assumed to vary linearly between zero at zero effective stress and the dry shear modulus at 1000 psi and above. This implies additional "frame softening" at low effective stress when the sample is fully saturated. The resulting Vp/Vs versus pressure trend for the clay-sand mixture (Figure 14) indicates that a small percentage of clay does not appear to alter the clean sand trend significantly. We shall see below that the difficulty of high predicted Vs at zero stress can also be alleviated by using a power law fit to the measured velocities with the result that clean sands and clay-sand mixtures do exhibit observably different Vp/Vs behavior as a function of effective pressure.

Power Law Pressure Dependence: Velocities measured with bender bar transducers for sediments at low effective pressure (Figure 15 after Bell; 1979) validate the hypothesis that Vs approaches zero as effective pressure goes to zero. We compiled water-saturated Vp measurements from this study, Bell (1979) and Domenico (1977), and fit them (Figure 16) with equations of the form:

$$V = a + b\,P^{c}$$

where a is constrained by Wood's equation at zero effective stress for P-wave velocities and is taken to be zero for shear-wave velocities in clean sands. The empirical coefficients b and c are then obtained by curve fitting the data. It is obvious by inspection of Figure 16 that the data can only be approximately fit by equations of this form as the coefficients will vary with porosity and composition. However, when taking the ratio of Vp to Vs much of the scatter is reduced (Figure 17) and a remarkably good fit results. The data of Prasad (in press) has also been added to Figure 17 showing general agreement with the Vp/Vs trend but higher Vp/Vs ratios (we suspect this is due to significantly higher porosities in Prasad's samples). This can be readily seen in Figures 18 and 19 which are plotted on a logarithmic pressure scale to emphasize differences between the trend from this study and Prasad's results. The spread in the data indicates that local well-log calibration of Vp/Vs trends for specific sites may be critical to future efforts to identify and characterize SWF.

Dispersion: Additional uncertainty in Vp/Vs trends results from possible velocity dispersion between ultrasonic laboratory measurements and seismic velocities. If we make the reasonable assumptions that (1) room dry velocities have negligible dispersion and (2) "frame softening" does not occur when an initially room dry sample is fully water-saturated, the amount of dispersion can be estimated by comparing ultrasonic water-saturated velocities to predicted water-saturated velocities using room dry velocities and Gassmann's (low frequency) equations as shown in Figure 20. The low frequency P-wave velocities are lower than the measured velocities while the measured and predicted shear-wave velocities are in good agreement. This suggests that seismic Vp/Vs ratios will be lower than ultrasonic Vp/Vs ratios (Figure 21).

Power Law Pressure Dependence in Clay-Sand Mixture: If we perform a similar fluid substitution on room dry shear-wave velocities (assuming rigidity is unaffected by saturation), a power law pressure dependence can be used to fit the 8 percent clay-sand velocity data (Figures 22 and 23). Surprisingly, the resulting Vp/Vs trend (Figure 24) exhibits lower Vp/Vs than the clean sand trend from this study and Prasad's trend. It is possible that these low Vp/Vs ratios result from the assumption of no frame softening of the rigidity. Alternatively, it is possible that clays may act to bind the loose sand grains, thereby effectively increasing the frame rigidity and decreasing Vp/Vs.

Summary of Velocity-Pressure Equations

Although new laboratory methods are required to confirm the predicted behavior at very low stresses, the observed and extrapolated behavior can be used to model the seismic response of an SWF reservoir to changes in effective stress. The equations for these behaviors are shown below.

Clean Water-Saturated Sands (This Study)

$$V_p \text{ (m/sec)} = 1700 + 200P_e^{0.22}$$

$$V_s \text{ (m/sec)} = 270P^{0.26}$$

Shaley Water-Saturated Sands (This Study)

$$V_p \text{ (m/sec)} = 1640 + 180P^{0.26}$$

$$V_s \text{ (m.sec)} = 160 + 210P^{0.30}$$

Water-Saturated Sands (Prasad, in press)

$$V_p/V_s = 5.6014P^{-0.2742}$$

MODELS FOR SWF SEISMIC RESPONSE

The laboratory measurements of compressional and shear wave velocities associated with pressure changes in the sands were used to generate a series of seismic model responses. The models were comprised of multiple layers of shale with montonically increasing velocity and density with an imbedded sand layer representing the SWF reservoir unit.

The model results suggest that the large changes predicted in V_s and V_p/V_s ratio will result in significant changes in the AVO response of the SWF sand units. The P-wave gathers (Figure 25) show a modest change in reflectivity and a significant change in the AVO response of the reservoir as a function of effective stress. Likewise, the mode-converted S-wave gathers, or P-S events (Figure 26), show a dramatic change in reflectivity and a change in polarity as a function of effective stress. The P-S reflection gathers also show a significant amount of attenuation on

the low effective stress models that is not present on the higher effective stress models. Furthermore, the large changes in attenuation exhibited by these sands will also cause significant frequency loss on seismic data. The seismic responses from these models indicate that high-resolution AVO and inversion methods should be able to resolve the changes in pressure and failure state that are related to the SWF problem. Analysis of the attenuation properties also suggests that changes in attenuation should be observed below sands that are abnormally pressured and prone to SWF, as evidenced by the loss of reflectivity at low effective stresses in Figure 26. It is also highly likely that, given multi-component seismic data, Poisson's ratio, modulus of rigidity and shear wave quality factor, can be extracted with greater resolution and accuracy than from conventional seismic data. The attenuation should be detectable particularly on multicomponent data by analysing the P-wave reflections from the SWF zone and mode converted shear wave reflections from SWF intervals and below them. Attenuation of both P and S reflections that have traveled through the SWF zone should be significant and should allow these zones to be mapped.

GULF OF MEXICO CASE STUDIES

To determine whether real multicomponent data can resolve the changes in physical properties associated with SWF conditions, Conoco worked with Dr. John Castagna of The University of Oklahoma and PGS Reservoir to evaluate the value of these data for shallow hazard analysis. Two sites were selected from the Gulf of Mexico (GOM) where PGS has acquired 2D multicomponent seismic data. These two locations, Green Canyon 472-473 (also known as King Kong) and Vioska Knoll 912-956 (also known as Ram-Powell), each have multiple well penetrations where SWF occurrences have been reported during well operations. The multi-component seismic data were tied to the drilling locations that encountered SWF and were analyzed using AVO, pre-stack attribute analysis, and pre-stack inversion.

REPROCESSING FOR SHALLOW HAZARD ANALYSIS

In general, exploration and production seismic data are processed for targets that are much deeper than the SWF zones. Therefore, most of these data are not suitable for detection of SWF occurences. In addition to processing, there are seismic acquisition issues that need to be addressed so that the shallow subsurface is imaged properly for SWF prediction. In particular, the correct positioning of sources and receivers is important to make sure that the geometry is applied properly to the data. The following sections discuss these issues as well as processing considerations to enhance imaging of the shallow section.

Survey Positioning

Figure 27 is a cartoon showing a source at two different shot points on either side of a horizontal inline receiver on the ocean bottom. If the first arrival signal recorded for a shot to the left of the receiver has the polarity indicated, then the first arrival polarity recorded for a shot on the right of the receiver will have the opposite polarity. The first arrival signal recorded for a source directly

above the receiver should be a null. This characteristic can be used to indicate whether the receiver position has been accurately determined.

Figure 28 is a typical receiver profile for the inline geophones for the Ram Powell data set. The flag indicates the zero offset as determined from the geometry. Notice the phase reversal of the first break wavelet as we go from negative to positive offset. However, the null is not at "zero offset" but occurs about 2 shot points towards negative offset indicating a problem with the geometry. A typical receiver profile for the King Kong data set is shown in Figure 29. The null and "zero offset" are displaced by at most 1 shot point.

Figure 30 is a plot of the King Kong source and receiver lines, as determined from the geometry, in the original acquisition coordinate system. The plot has about a 2 to 1 exaggeration in the South-North direction. At this scale some variation in the lines can be detected. Figure 31 is a plot of the source and receiver lines in an inline-crossline coordinate system, where the inline direction was determined by fitting a line to all of the source lines. The exaggeration in the crossline direction is very large. The nominal shot and receiver spacing is 25 m and 50 m, respectively. This figure shows that the displacement of the actual positions of the source and receivers from their desired positions are of the order of the shot/receiver spacing.

These "errors" in positioning affect the quality of stacked data. The effect is more pronounced in the shallow section than in the deeper section. Therefore, it is important to improve the accuracy of source and receiver positioning for shallow water flow prediction from seismic data.

Processing Considerations

The prediction of shallow water flows from seismic data requires that special attention be paid to enhance the shallow seismic section. Typical processing for oil and gas objectives focuses on the deeper section, which usually compromises the quality of the shallow section. In this study, our first task was to improve resolution in the shallow section for both the PP and PS data. This was accomplished by the following: (1) we processed the data at 2 msec sample rate instead of the 4 msec rate previously used by PGS, (2) our velocity analyses were done to specifically target the shallow section, and (3) the processing parameters/flow were selected to enhance resolution in the shallow section even if it meant sacrificing image quality in the deeper section.

One of the critical differences between the SITC processing flow and the PGS original processing was the application of wave equation datuming. Since the sources were at or near sea level and the receivers were on the sea floor, PGS applied wave equation datuming to bring the sources closer to the sea floor. SITC's experience with wave equation datuming suggests that the shallow section is adversely affected by it. This may be due to the large water depth (~3850 ft) in the King Kong area. Figure 32 shows a comparison of the P-P stack for King Kong data with and without wave equation datuming. Clearly, with wave equation datuming we would not have been able to image potential shallow water flow zones in the shallow section. This is not to say that some type of correction is not needed to account for the elevation differences between the

sources and receivers. SITC will be experimenting further with wave equation datuming and other techniques to correct the data.

CASE HISTORY FROM RAM-POWELL SEISMIC DATA

The Ram-Powell field (Figure 33) in Viosca Knoll 912, 956, and 957 is located in 3200 ft of water about 50 miles east of the Mississippi river mouth. The field is on the continental slope between the Mississippi and DeSoto canyons. Sediment deposited within the upper several hundred ms of the water bottom consists mainly of Pleistocene-age hemipelagic muds (Galloway and others, 1991). Benthic forams from borings north of Ram-Powell suggest that these shallow sediments were deposited on the east flank of a late Wisconsin-age depositional thick in a middle/outer neritic to bathyal environment (Moore et al, 1979). Interpretation of these data indicates sediments of this age are roughly 100 to 150 m thick around Ram-Powell. A thin veneer of post-glacial sediments, less than 5 m thick, occurs just below the water bottom. Based on the multicomponent seismic line through the area (Figure 34), the seismic facies in the upper several hundred milliseconds consists of mainly parallel, continuous reflectors with variable amplitude strengths. There is evidence of channel cuts in some places, but these are probably mainly shale filled. The lack of higher energy chaotic facies is consistent with the sand poor depositional setting.

Seismic Data for the Ram Powell Location

During the last few years, numerous multicomponent seismic surveys have been acquired in the Gulf of Mexico. Figure 35 shows the location of the surveys acquired by PGS. A 4-component, ocean-bottom cable (OBC) survey was acquired by PGS in the Ram Powell area. Figure 36 shows the location of the PGS line. Since we did not have access to hazard data or shallow well log data for the Ram Powell area, we could do only a limited amount of work with the multicomponent seismic data. However, the following results show that we were able to greatly enhance the quality of shallow seismic data which allowed us to determine the variation of Vp/Vs ratio in this area.

Results with the Multicomponent Data

PGS did the initial processing on multicomponent data with the objective of enhancing the deeper prospective horizons. Figures 37 and 38 show the compressional wave (PP) and converted wave (PS) sections, respectively, as a result of the initial processing. It is clear that the sections generated by PGS did not provide adequate resolution in the shallow section for the SWF study. Therefore, our first task was to improve resolution in the shallow section for both the PP and PS data. This was accomplished by following the precedures recommended earlier in our discussion of "processing considerations." Figures 39 and 40 show our processing results for the PP and PS sections, respectively. It is clear from Figures 39 and 40 that the major reflectors on the compressional wave and converted wave sections can be more easily correlated than on the sections shown in Figures 37 and 38. Therefore, it should be easier to calculate the Vp/Vs ratio from these sections.

Vp/Vs Analysis of the Multicomponent Data

Figure 41 shows the Vp/Vs ratio obtained by correlating horizons on the PP and PS sections. Even though the resolution of the data is not sufficient to identify changes in the Vp/Vs ratio for a particular horizon, we can confirm that the trend within a layer encompassing several horizons is consistent with expectations. Here Vp/Vs within a layer clearly increases with water depth. Therefore, we can conclude that the Vp/Vs anomalies are potentially related to pore pressure which also increases with increasing water depth.

Fluid Factor AVA (FFAVA)

The Fluid Factor Amplitude versus Angle (FFAVA) plot is a screening tool for locating AVA anomalies in seismic data. The concept is to highlight deviations in AVA behavior from a background "fluid trend," assumed to consist of reflections from water-saturated rocks. The "fluid factor" idea was introduced by Smith and Gidlow (1987) and refined by Gidlow, Smith, and Vail (1992).

Figure 42 shows the FFAVA plot for the Ram Powell line. The FFAVA anomalies in a layer are generally marked by a negative impedance contrast at the top the layer and a positive impedance contrast at the bottom (blue/red). It is apparent from Figure 42 that the anomalies are mainly confined to the very shallow portion of the section, especially just below the sea floor. Moreover, the anomalies are not very robust, indicating that the anomalous zones are very thin. This is consistent with minor SWF occurences observed just after commencement of drilling in the Ram Powell area wells.

CASE HISTORY FROM THE KING KONG AREA

The King Kong deepwater discovery (GC 472-473) is located in southeastern Green Canyon roughly 125 miles south-southwest of the Mississippi River mouth (Figure 33). These blocks are in a slope setting with average water depths of around 3800 ft. The region is characterized by salt withdrawal minibasins within an extensive allocthonous salt canopy. The shallow stratigraphic section of interest in this study consists of very young hemipelagic and turbidite deposits. Paleocontrol from Weimer et al (1998) indicates the age of these deposits is much less than 0.5 Ma. Several different seismic facies have been identified, some of which are interpreted to be sand-prone.

Seismic Data For The King Kong Location

The seismic data for this study were selected from the Green Canyon Block 473 where Conoco drilled well GC 473-1 in 1991 in the King Kong prospect and encountered a shallow water flow. The SWF occurred away from the wellbore when the 20" casing was cemented at a depth of 5950 ft, approximately 2100 ft below the mud line. Since the SWF did not actually occur in the wellbore, there is a strong indication that it could have originated from a depth much shallower than where the 20" pipe was set.

In 1998, PGS acquired a 4-component, ocean-bottom cable (OBC) survey on Green Canyon Blocks 471, 472, and 473. Figure 43 shows the location of the PGS line, which crosses well locations GC 473-1 and GC 472-1 in the NW-SE direction. In addition to the PGS line, SITC had access to the hazard data, which was acquired for Conoco in 1990 by Marine Technical Services, Inc. These data consist of seventeen E-W lines and five N-S lines on Block 473 (Figure 44). Figure 44 also shows the PGS line cutting across Block 473 in relation to the hazard data and the well location 473-1.

Well Log Data For King Kong

In the Conoco well GC 473-1, conventional wireline logs (e.g., sonic, density, resistivity) were run from about 6970 ft to a TD of 14368 ft MD. Since this zone is well below the depths where SWF were reported, these logs were not incorporated into our study. However, ExLog MWD gamma ray and resistivity logs (Figure 45) were available from 4154 to 7063 ft MD and were used for lithologic determination and correlation to the 2D shallow hazard Seismic Line 107 (Figure 46). Emphasis was placed on the stratigraphic section above the 20-inch casing shoe (5950 ft MD, 2070 ms TWT) because flows were reported from somewhere above that depth. The MWD gamma ray and resistivity logs acquired were the only log data available to characterize the shallow section.

The MWD gamma ray log was used as a lithology (sand/shale) indicator. However, lithologic interpretations were hindered by fairly poor log quality. Although a shale baseline could not be established with confidence, relatively sandy intervals at 4430-4630 ft, 4750-4800 ft, and 5150-5280 ft MD were noted. The poor MWD gamma ray log quality hindered attempts to identify shale-prone intervals that could act as pressure seals.

A zero-offset synthetic was created to tie these sandy intervals to the 2D shallow hazard seismic line 107 at the well location (Figure 47). The synthetic impedances were based on compressional wave velocities and densities derived from transformation of the resistivity log.

The compressional velocities were derived from the MWD resistivity log using Faust's relationship and calibrated to the shallow hazard 2D seismic stacking velocities (Figure 48). The expression used was

$$V_p = 3300(Z\rho)^{0.09}$$

where V_p is the calculated compressional wave velocity in ft/s, Z is the depth below mudline in ft, and ρ is the measured MWD resistivity.

The densities were derived from the calculated velocities using Gardner's relation

$$\rho_{\text{bulk density}} = 0.2303V_p^{0.25}$$

where $\rho_{\text{bulk density}}$ is the calculated bulk density and V_p is taken from the preceding equation. Although the entire sonic log was calibrated, only the part down to the 20-inch casing shoe was used. Figure 45 shows the calculated V_p, density, and impedances used to create the zero-offset synthetic.

The well tie (Figure 49) was marginal given that the correlation coefficient between the seismic and synthetic was only about 0.53 over the fairly short 440 ms correlation window. The calculated impedances failed to capture much of the high frequency character of the seismic reflectivity. But, even though the synthetic did not have high fidelity, the depths of the sandy intervals identified on the log were determined with greater certainty. This was because the low frequency velocity trend that governed the time-to-depth relationship was fairly similar to the trend expressed by the stacking velocities used to process the seismic.

The sandy intervals identified on the gamma log (see discussion above) were interpreted to occur at 1730-1760 ms, 1780-1800 ms, and 1890-1915 ms, respectively, on Seismic Line 107.

Shallow Hazard 2D Seismic

The high-resolution 2D seismic survey was interpreted for SWF at GC 473. Seismic facies analysis and standard interpretation techniques were used to help identify which stratigraphic intervals had the highest potential for SWF. An interval about 700 ms below the water bottom was considered.

The three key geologic criteria for high potential of SWF are:

- A high-porosity, high-permeability, sand-prone aquifer.
- A mechanism to pressurize the aquifer.
- A competent seal.

Seismic facies analyses helped identify shale/sand prone stratal packages. The analysis was based in part on reflector amplitude, geometry, and continuity. Three seismic facies were identified in the GC 473 area (Figure 50):

- High amplitude, parallel, and continuous reflectors. Interpreted as shale-prone section.

- Low amplitude, discontinuous reflectors. Interpreted as relatively uniform shale-prone pelagic deposits that may contain thin sandy layers.

- High amplitude, discontinuous reflectors. Interpreted as sand-prone, possible channel-levee deposits.

Based on these three facies groups, the shallow section from about 2.3 s up to the water bottom was grouped into 4 intervals (Figure 50):

- The deepest interval was about 150 ms thick and consisted of moderate-high amplitude continuous reflectors bounded on the top by Horizon C. This interval was interpreted to be shale-prone.

- A roughly 200-250 ms thick interval, with variable amplitudes having poor lateral continuity. This interval was bounded on top by Horizon B. This interval was interpreted as a channelized sand-prone zone.

- A 150-200 ms thick interval with low amplitude, discontinuous reflectors. This interval was bounded on top by Horizon A. Lack of internal reflectivity suggested this interval had more uniform lithology and was probably less sandy than the high amplitude, discontinuous facies.

- The shallowest interval was about 150 ms thick and was characterized by high amplitude, continuous reflectors that extend up to the seafloor.

The water bottom time structure map (Figure 51) was also studied to characterize the SWF potential of the study area. Often examination of the water bottom reveals expulsion features (e.g., mud mounds), sea-floor scarps, faults, and anomalous amplitudes that indicate flowage to the seafloor has occurred.

The water bottom was at a depth of 3855 ft at GC 473-1. The water bottom map showed a relatively uniform S dip with a linear structural high in the SE corner of the survey between Cross Lines 114 and 117. This structural high may be fault related.

The interval between Horizons B and C (Figure 50) was interpreted to have potential for SWF. Evidence for sand was based on the high amplitude, discontinuous seismic facies and to a limited extent on the identification of sandy zones in the MWD gamma ray log. However, poor log quality precluded heavy reliance on the gamma ray log. Seismic mapping showed the GC 473-1 well was proximal to a NNW-SSE trending channel. The channel down-cut hundreds of ms into the surrounding sediment. A continuous sub-regional reflector above the interval was interpreted to be a seal (Figure 50). This reflector separated the sand-prone facies from a shalier facies overlying it. Lateral seals were not interpreted. Isochrons of the overlying section indicate depositional thicks in the eastern part of the study area may have provided a pressurization mechanism via the asymmetrical sediment load (Figure 52). Figure 53 shows that the chronostratigraphic relationship between the three geologic criteria was appropriate for the creation of SWF conditions in the interval between Horizons B and C.

Results with the Multicomponent Data

Figures 54 and 55 show the compressional wave (PP) and converted wave (PS) sections, respectively, with the original PGS processing. As in the Ram Powell case, it is clear that the sections generated by PGS did not provide adequate resolution in the shallow section for the SWF study. SITC enhanced processing led to significant improvement in data quality in the shallow section. Figures 56 and 57 show the PP and PS seismic sections, respectively, after

changes in the processing flow were made to improve the shallow section. It is clear from Figures 56 and 57 that the major reflectors on the compressional wave and converted wave sections can be more easily correlated than the sections shown in Figures 54 and 55. Therefore, it should be easier to calculate the Vp/Vs ratio from these sections. In comparing Figures 54-57, one should note the time shift between the PGS and Conoco processed data because of different bulk shifts that were applied to the data in each processing scheme. Since the water depth at well GC 473-1 is 3855 ft, the water bottom should actually occur at about 1.59 sec, assuming a constant water velocity of 4850 ft/sec.

The hazard data mentioned earlier show even higher resolution in the shallow section because of the higher frequency source used to acquire these data. These data were acquired with a sample rate of 1 msec and a total recording time of 3 sec. Therefore, it should be sufficiently deep to encompass the shallow water flow encountered in the Conoco well GC 473-1. Line 107 (Figure 46) which passes through well GC 473-1 shows the quality of hazard data after the SITC processing to improve resolution in the shallow section. Earlier discussion on data interpretation focused on how the hazard data were used in conjunction with well log data to arrive at preliminary interpretation of SWF zones in the King Kong prospect area.

Vp/Vs Analysis of the Multicomponent Data

Figure 58 shows a stacked PP section with picked horizons. These horizons were correlated to the PS (Figure 59) section using the mudrock trend as a guide for PP to PS time conversion and basing final picks on character and interpreted geology. Note that the slope of the fault as interpreted on the PP and PS sections is internally consistent with the mudrock trend. Significant uncertainty in correlation remains, however.

Vp/Vs ratios calculated from PP and P-S travel times are very high (over 10) near the water bottom, decrease rapidly with increasing depth (Figure 60), and are generally close to the mudrock trend. However, lateral variations in Vp/Vs are not obvious due to the large range of Vp/Vs ratios observed. To aid in SWF interpretation, the fractional change in Vp/Vs with respect to the mean Vp/Vs in each layer is displayed in Figure 61. Significant lateral variations are now apparent with some probably due to picking uncertainties. Other variations are presumably related to pore pressure or lithologic changes. At the well location (about CDP 700), anomalously high Vp/Vs ratios are observed in the first (near surface) and third (sandy) intervals and anomalously low Vp/Vs are observed in the second interval which is presumably shale. This unusual behavior could be an artifact of picking errors or may perhaps be related to slower rates of deposition that are associated with shale-prone section.

FFAVA and Prestack Inversion

Figure 62 shows the FFAVA plot for the King Kong data. An expanded version of this plot in Figure 63 shows more clearly the FFAVA anomalies in the vicinity of well GC473-#1. For example, there are three distinct anomalies at ~0.9, 0.96, and 1.08 seconds (blue/red) which could be due to overpressured sand bodies or SWF sands which flowed near this well. Since the

sand flow occurred some distance from the well location, it is highly likely that the sands at 0.9 and/or 0.96 seconds were responsible for SWF at King Kong area. The zero-offset reflectivity plot in Figure 64 also confirms reflections at these times from the top and bottom of a low impedance zone embedded in high impedance sediments.

Figures 65 and 66 represent relative changes in Poisson's ratio for the King Kong area and help narrow our search for the SWF sand. The sand at ~0.9 seconds has a higher Poisson's ratio than the background while the sand at 0.96 sec has a smaller Poisson's ratio. Since the SWF sands should have low rigidity and thus high Poisson's ratio, it is very likely that the SWF sand in the King Kong area is the one identified at 0.9 seconds. Thus, the source of the flow is just below the seafloor.

MECHANICAL FAILURE

At very low effective stresses, the physical conditions in these SWF sands are such that they are close to critical porosity with porosities from 38-50 percent according to the sorting and shaliness of the specific stratigraphic unit. The high porosities and uncemented, unconsolidated nature of these sands, along with the very low effective stresses, also suggest that they should have very low failure strengths and may exist in a state of incipient failure that allows them to flow into a wellbore when penetrated by the drill bit. SWF sands often are abnormally pressured up to 200 psi above the surrounding sediments, which may increase the mechanical instability that leads to significant flows. In a relative sense, the actual pore pressure difference in these sands is very small, often being less than 100 psi. However, such small changes in pressure at these shallow depths of burial can lead to significant water flows that can cause formation collapse and massive sanding into a well. The unconsolidated state of these sediments also provides sufficient formation porosity such that the volume of producible water can be quite large. When an SWF sand has an extensive down-dip extent, the volume of producible water and the hydrostatic support available to maintain the flow for long periods of time can be severe.

One of the major questions regarding SWF is the cause of failure. At present, there are two likely possibilities. First, it is possible that these materials are already in an incipient state of failure and that the act of drilling simply initiates the flow by dynamic loading of the sediments at the wellbore interface. The analog for this type of failure is well known in the earthquake literature and is called liquefaction. Liquefiable materials documented from earthquake studies (Richart et al, 1970) tend to be high porosity and of a coarse granular nature, very similar to SWF sands. These failures are caused by the rearrangement of grains due to dynamic loading that causes the local pore pressure to increase dramatically as the material attempts to compact under the loading. Such materials have been documented to flow to the surface and vent spectacularly as has been observed in some SWF case studies.

Second, it is possible that these materials are so cohesionless that the mere flow of formation water into the wellbore causes the sand to flow as well and that the sustained flow of formation water eventually destabilizes the entire formation and results in a total collapse of the SWF interval. Effectively, this is a type of catastrophic sanding problem. The difference between these two failure modes is significant in that catastrophic sanding can likely be mitigated by

changes in drilling fluid pressure and properties while liquefaction must be mitigated by decreasing the dynamic loading induced by the drilling operation so that the formation does not "feel" the drillbit passing through it. More direct measurements of SWF zones while drilling are needed to determine which of these failure modes are occurring. It is possible that both failure modes are present, but the data available to date are insufficient to distinguish between them.

CONCLUSIONS

The physical properties of SWF sands are very different from most reservoir and seal rocks that are studied for petroleum purposes. These materials exist near the transition between rocks and sediments and possess physical properties that can be used to identify them using seismic data. The results of this study suggest that the physical properties of SWF sands are amenable to a seismically derived prediction methology that includes inversion, seismic attributes, and attenuation analysis. Combining these methods with high-resolution multicomponent seismic acquisition and processing should help to avoid these costly hazards and prevent costly well failures in the future.

The results of the study reveal that multicomponent seismic data can indeed be used to detect and delineate SWF hazards in the deepwater environment. Key conclusions of the study include the following points.

1. Rock physics measurements and the resulting seismic models support the contention that SWF sands can be detected using seismic analysis.

2. The seismic data from King Kong revealed several zones where anomalous AVO and inversion signatures are believed to be related to SWF sands. These signatures are consistent with the well results and are quite robust.

3. Seismic data must be processed with a focus on the shallow geology if robust results are to be obtained from seismic analysis methods. Industry standard processing of seismic data for deeper targets is not adequate for this purpose.

4. Shear wave data gathered from multicomponent Ocean Bottom Cable surveys must be treated very carefully as the shear velocities in the shallow sediments are extremely slow and can have large static corrections and time delays associated with them.

5. Positioning of the OBC sensors must be done with significantly greater accuracy because of the slow shear wave velocities in these sediments.

6. Standard industry seismic sources may not always provide sufficient resolution to detect thin SWF hazards. Therefore, it is recommended that a second acquisition using high-frequency source arrays be deployed to assure acquisition of the high frequencies required to image SWF sands in the shallow section.

7. Future studies like this one should be planned at pre-drill locations for new wells so that unpenetrated shallow section may be analyzed and predictions can be made that will later be confirmed by the drill bit and PWD tools.

8. Improved shallow logging and core sampling information will be essential to further progress in understanding SWF as this and most other studies that have been published have all been limited by the paucity of ground truth for calibration of seismic data.

REFERENCES

Bell, D. W., 1979. Shear Wave Propagation in Unconsolidated Fluid Saturated Porous Media. Ph.D thesis, University of Texas at Austin.

Bouma, A. H., Roberts, H. H., and Coleman, J. M., 1992. Late Neogene Louisiana Continental Margin Construction Timed by Sea-Level Fluctuations in: Watkins, J. S., Zhiqiang, F., and McMillen, K. J. (eds.). Geology and Geophysics of Continental Margins, AAPG Memoir 53, p. 334.

Castagna, J. P., Batzle, M. L., and Kan, T. K., 1993. Rock Physics-The link between rock properties and AVO response: in Castagna, J. P., and Bachus, M. M. *Offset-Dependent Reflectivity- Theory and Practice of AVO Analysis,* DEG Publication.

Domenico, S. N., 1977. Elastic properties of unconsolidated porous sand reservoirs. Geophysics, 42, No. 07, 1339-1368.

Dvorkin, J., and Nur, A., 1996. Elasticity of high-porosity sandstones: Theory for two North Sea data sets. *Geophysics*, v. 61:1363-1370.

Galloway, W. E., Bebout, D. G., Fisher, W. L., Dunlap, J. B., Jr., Cabrera-Castro, R., Lugo-Rivera, and Scott, J. E., 1991. Cenezoic, in: Salvador, A., ed. The Gulf of Mexico Basin: Boulder Colorado, Geological Society of America, The Geology of North America, pp. 270, 289.

Gidlow, P. M., Smith, G. C., and Vail, P. J., 1992. Hydrocarbon detection using fluid factor traces: a case history; in Robinson, J. H., ed., How Useful is Amplitude-Versus-Offset Analysis? Technical Program and Abstracts, Joint SEG/EAEG Summer Research Workshop, Aug 9-14, Big Sky, Montana.

Marion, D., and Nur, A., 1989. Percolation of electrical and elastic properties of granular materials at the transition from a suspension to a loose packing. *Physica A*, v. 157:575-579.

Marion, D., Nur, A., Yin, H., and Han, D., 1992. Compressional velocity and porosity in sand-clay mixtures. *Geophysics*, v. 57:554-562.

Moore, G. T., Woodbury, H. O., Worzel, J. L., Watkins, J. S., and Starke, G. W., 1979. Investigation of Mississippi Fan, Gulf of Mexico. Geological and Geophysical Investigations of Continental Margins. AAPG Memoir 29., p. 399.

Nur, A., Mavko, G., Dvorkin, J., and Galmudi, D., 1998. Critical Porosity: A key to relating physical properties to porosity in rocks. *The Leading Edge*, v. 17, n. 3: 357-362.

Prasad, M., 2000. Acoustic Measurements in Sands at Low Effective Pressure: Overpressure Detection in Sands. Geophysics, in press.

Richart, F. E. Jr., Woods, R. D., and Hall, J. R. Jr., 1970. *Vibrations of Soils and Foundations*, Prentice Hall, Englewood Cliffs, NJ, 414 pages.

Smith, D. T., 1974. Acoustic and mechanical loading of marine sediments. *Physics of Sound in Marine Sediments,* edited by L. D. Hampton, Plenum Press, New York.

Smith, G. C., and Gidlow, P. M., 1987. Weighted stacking for rock property estimation and detection of gas. Geophysical Prospecting, 35, 993-1014.

Stump, B. B., Flemings, P. B., Feinbeiner, T., and Zoback, M. D., 1998. Pressure differences between overpressured sands and bounding shales of the Eugene Island 330 Field (Offshore Louisiana, USA) with implications for fluid flow induced by sediment loading, in Mitchell, A., and Grauls, D., editors. Overpressures in Petroleum Exploration, Memoire 22, Elf EP Editions, pp. 83-92.

Traugott, M. O., and Heppard, P. D., 1994. Prediction of pore pressures before and after drilling-Taking the risk out of drilling overpressured prospects, in: Abnormal Pressures in Hydrocarbon Environments. Petroleum Geologists Hedberg Conference, Golden CO, June 8-10, AAPG Bulletin.

Weimer, P., Crews, J. R., Crow, R. S., and Varnai, P., 1998. Atlas of Petroleum Fields and Discoveries, Northern Green Canyon, Ewing Bank, and Southern Ship Shoal and South Timbalier Areas (Offshore Louisiana), Northern Gulf of Mexico. AAPG Bulletin V. 82, No. 5B, p. 881.

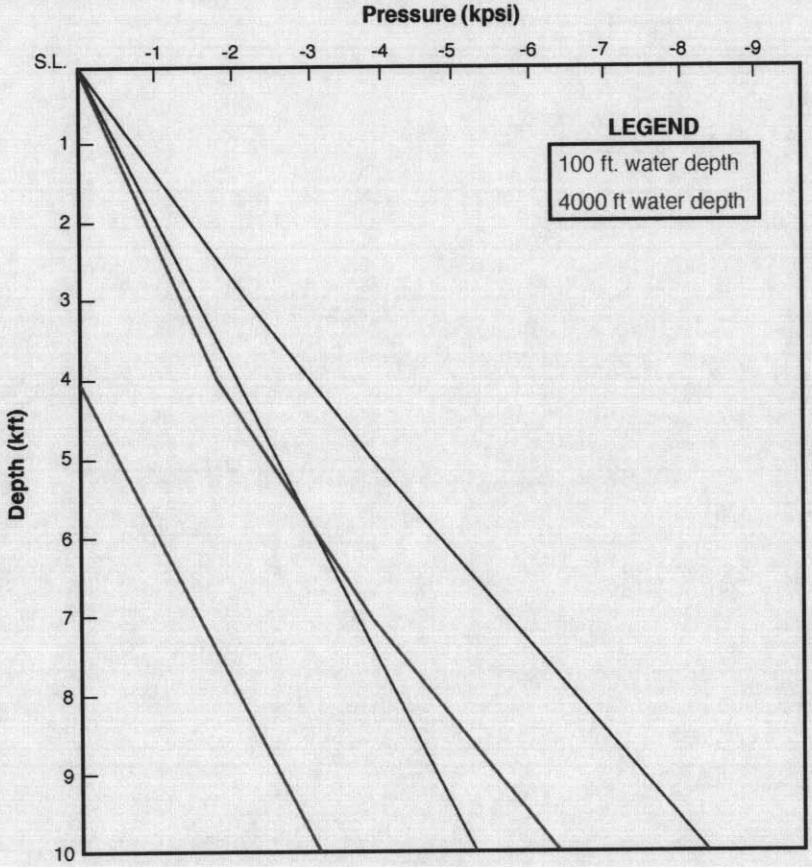

Figure 1. Examples of confining stress and effective stress from shallow water (blue curves) and deep water (red curves) showing the contrast in loading conditions. Note that the difference between the red curves between 4000 and 7000 feet depth, which represents the pore pressure, is much larger than the difference between the blue curves at the same depth.

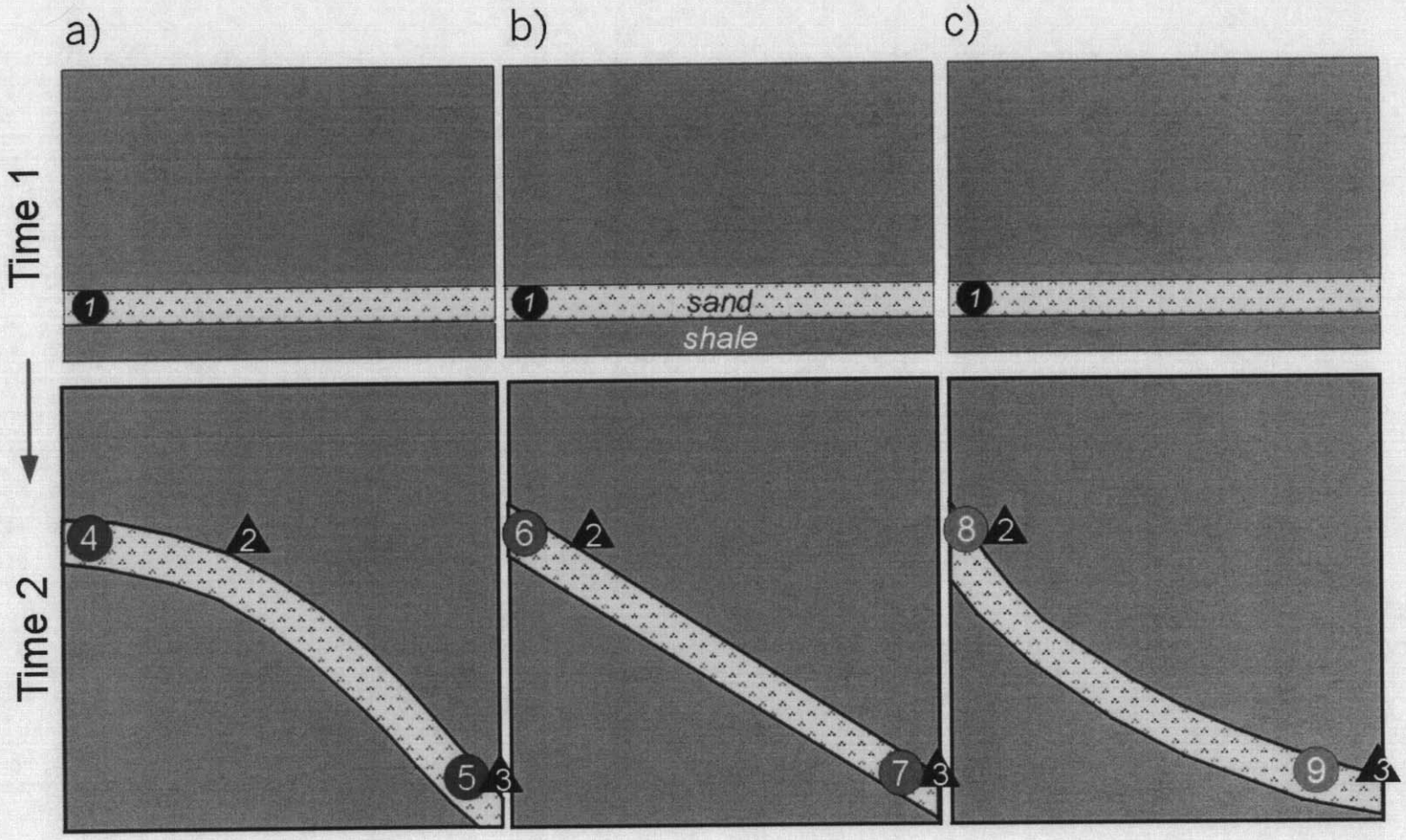

Figure 2. Model of a sand that is deposited on a flat surface and then positioned structurally to create a hyperpressured reservoir. At time 1, the sand is in equilibrium with all pressures equal. At time 2, the sand pressures are different with respect to each other and with respect to the pressures in the adjacent shales and are affected by the type of structure. Figure taken from Stump et al. (1998).

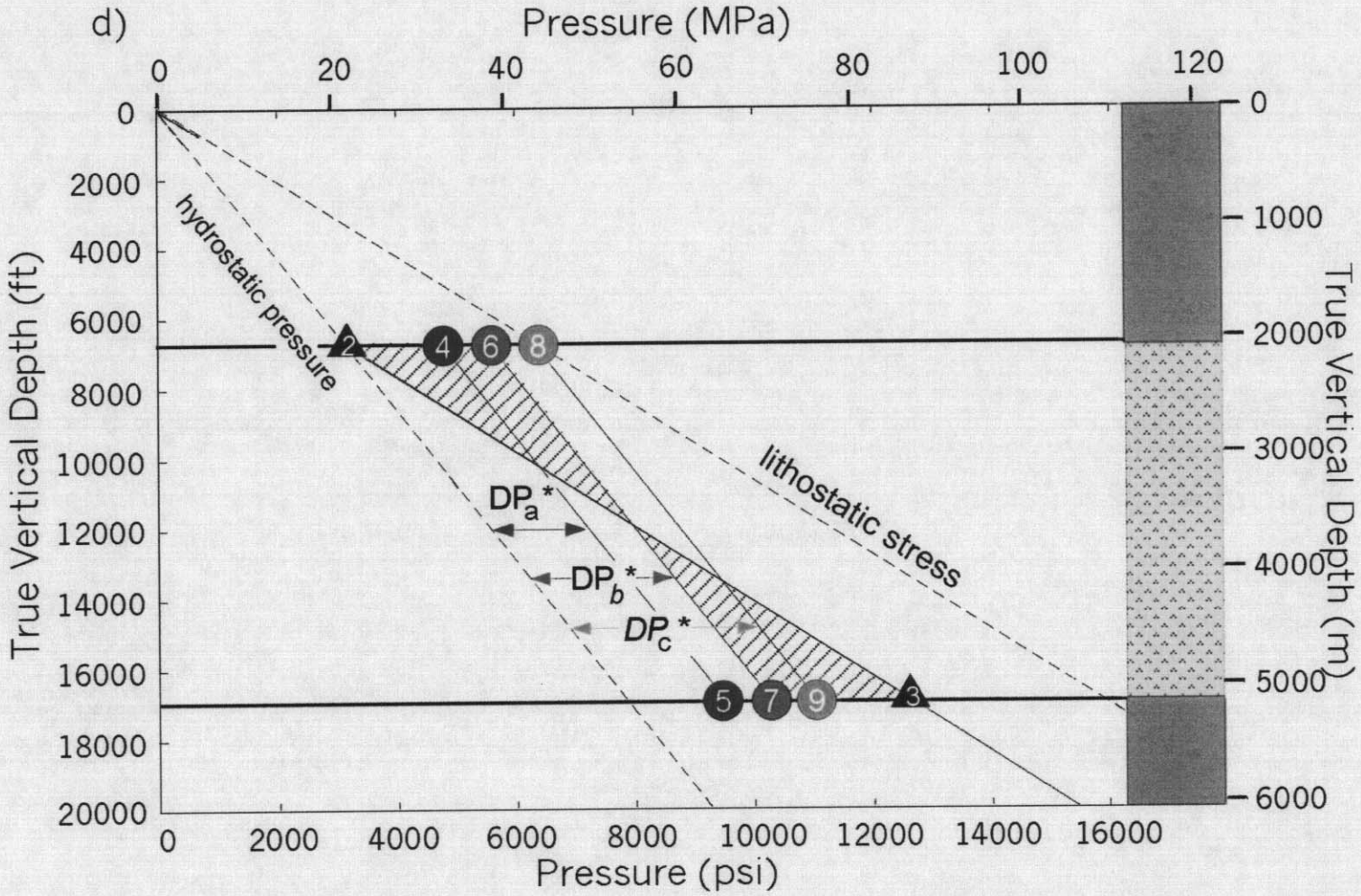

Figure 3. Pressure diagram showing the relationship between the structurally hyperpressured sand shown in Figure 2 and the surrounding shales. The numbers correspond to the numbers defining structural position of each sand in Figure 2. The numbers 4, 6, and 8 represent the pressure at the top of the sand body, and the numbers 5, 7, and 9 represent the pressures at the bottom of the sand. The numbers 2 and 3 are the pressures at the top and bottom of the shale. The centroid of each sand is the point where the reservoir pressure intersects the shale pressure. Figure taken from Stump et al. (1998).

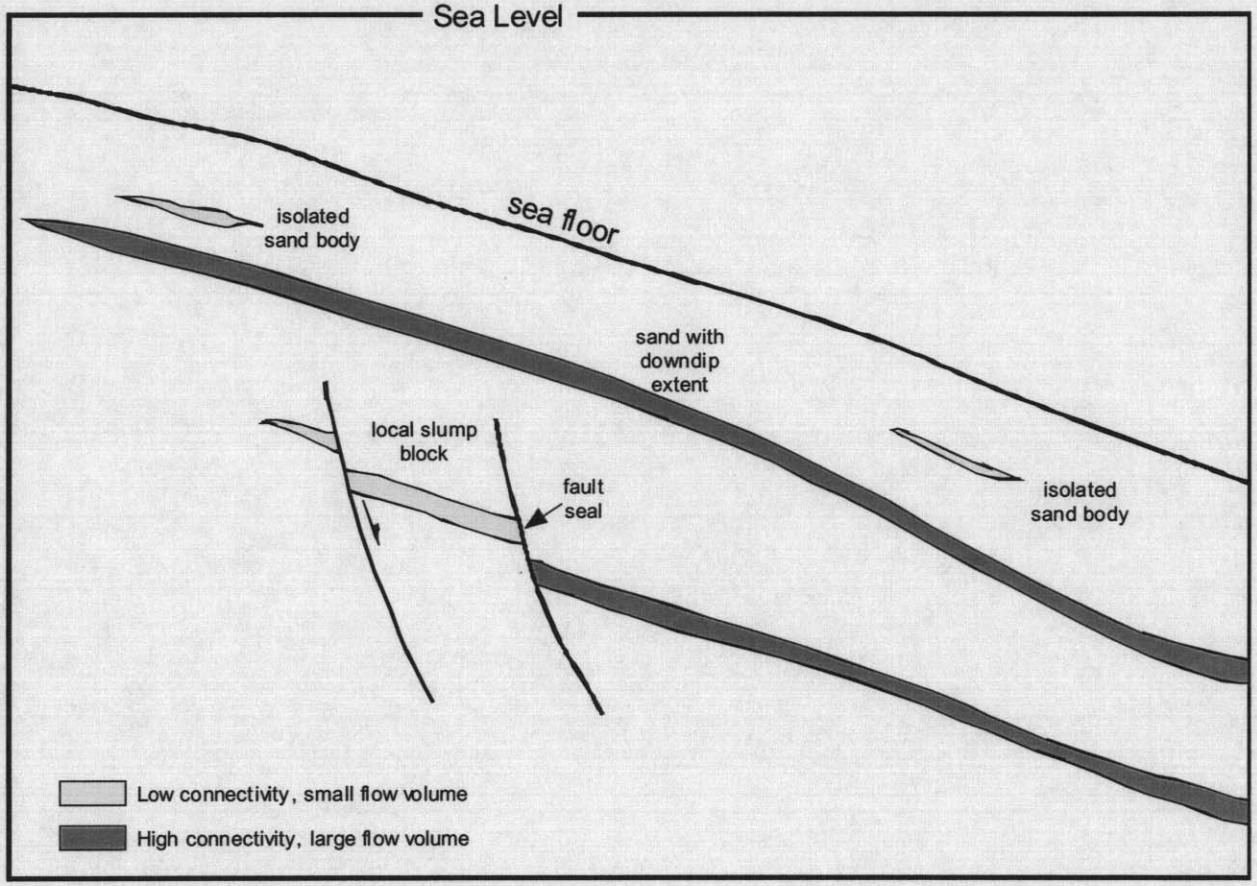

Figure 4. Diagram showing the types of shallow flowing sands characterized by their hydrologic continuity and ability to produce a given volume of fluid. Note the large volume of water that can be produced by the sands that have large down-dip extents and structural hyperpressuring (red) versus those with small extent (yellow).

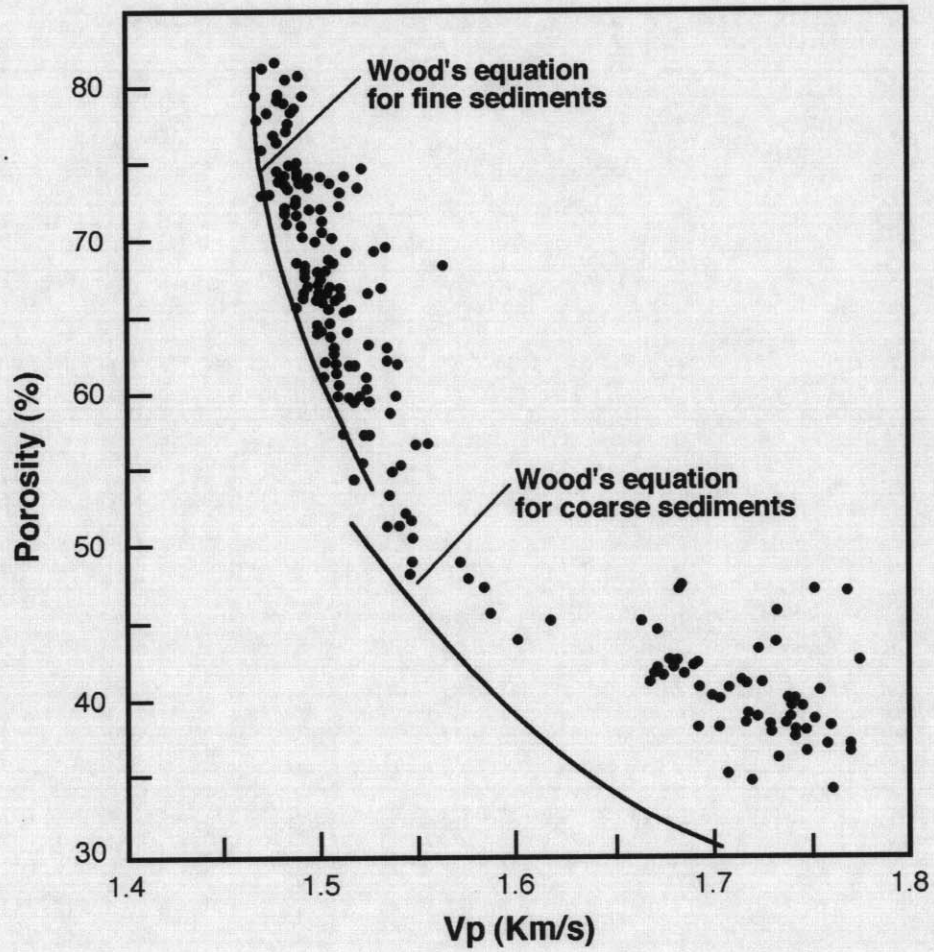

Figure 5. Porosity velocity relationships observed in marine sediments. Note the differences between the measurements and the curves for Wood's equation which are probably due to dispersion effects. Figure is after Smith (1974).

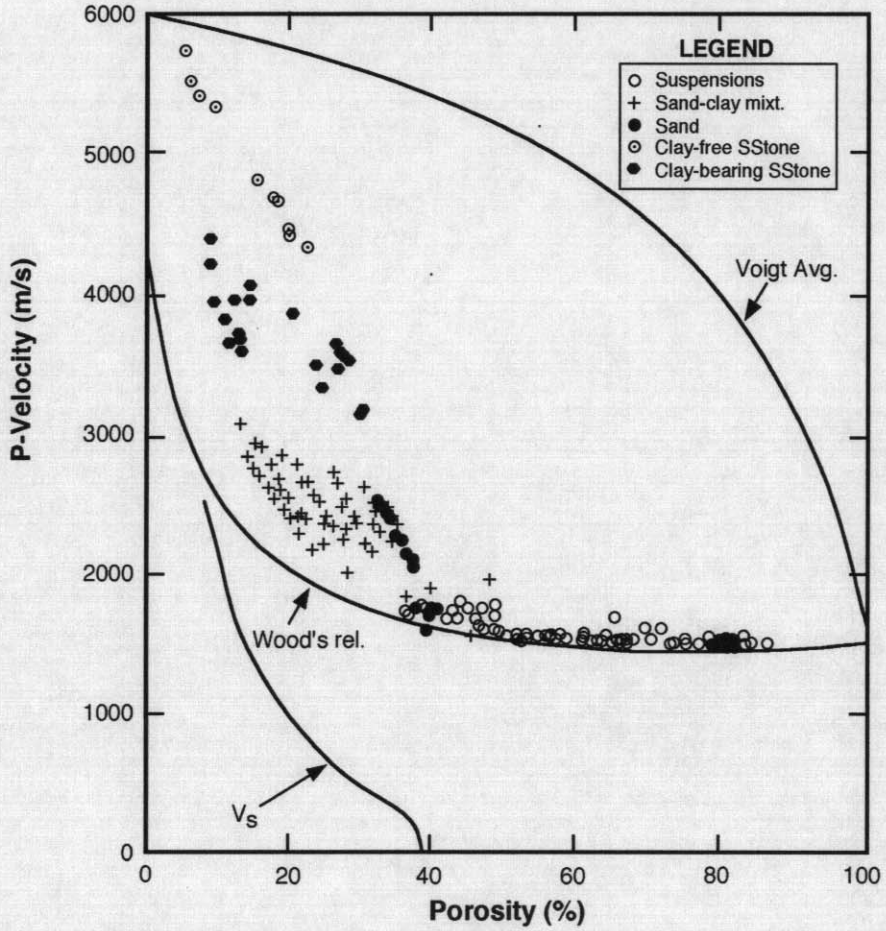

Figure 6. Velocity-porosity relationships in clastic sedimentary materials. Note the change in behavior caused by the inception of load-bearing capability at the critical porosity point. At porosities less than critical porosity, the material behaves like a Voight-Reuss material. Also note the shear wave behavior and how rapidly it changes at the critical porosity. Figure after Marion et al. (1992).

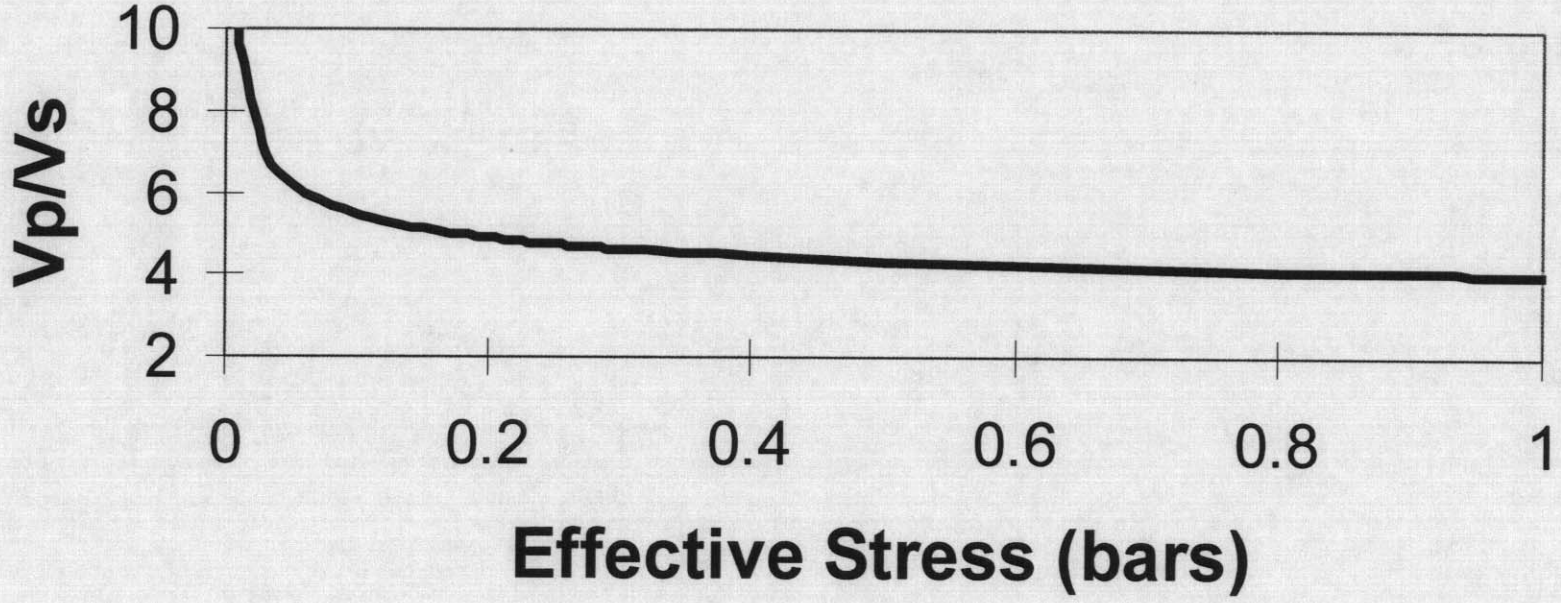

Figure 7. Relationship between Vp/Vs and effective stress for a 42 percent porosity sand pack predicted from empirical equations given by Castagna et al. (1993).

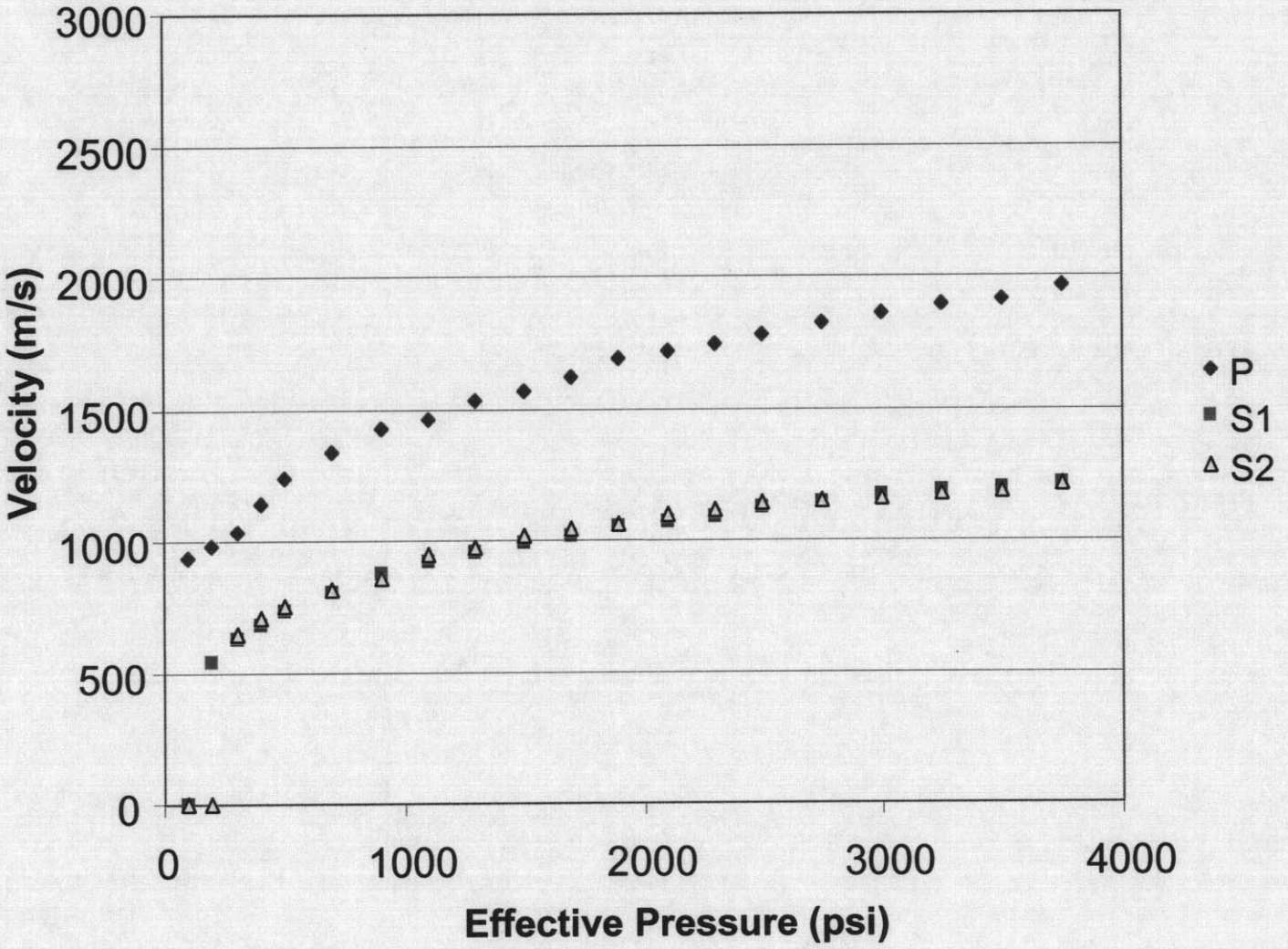

Figure 8. Room dry Vp and Vs measurements for a clean sand pack. Two shear-wave polarizations (S1 and S2) yield almost identical velocities. No shear wave could be discerned below 200 psi.

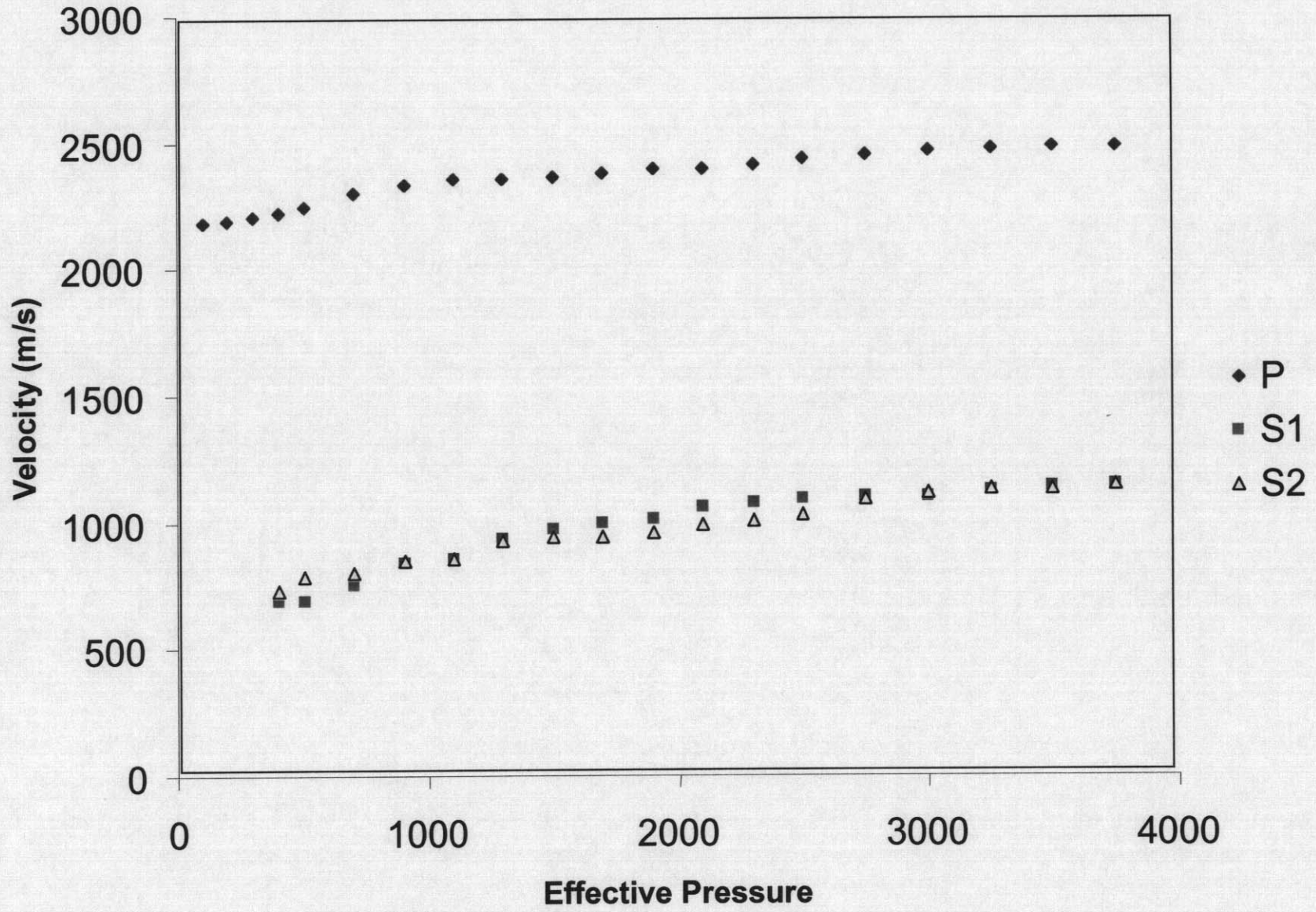

Figure 9. Fully water-saturated Vp and Vs measurements for a clean sand pack. Two shear-wave polarizations (S1 and S2) yield almost similar velocities with differences that are probably not significant. No shear wave could be discerned below 400 psi.

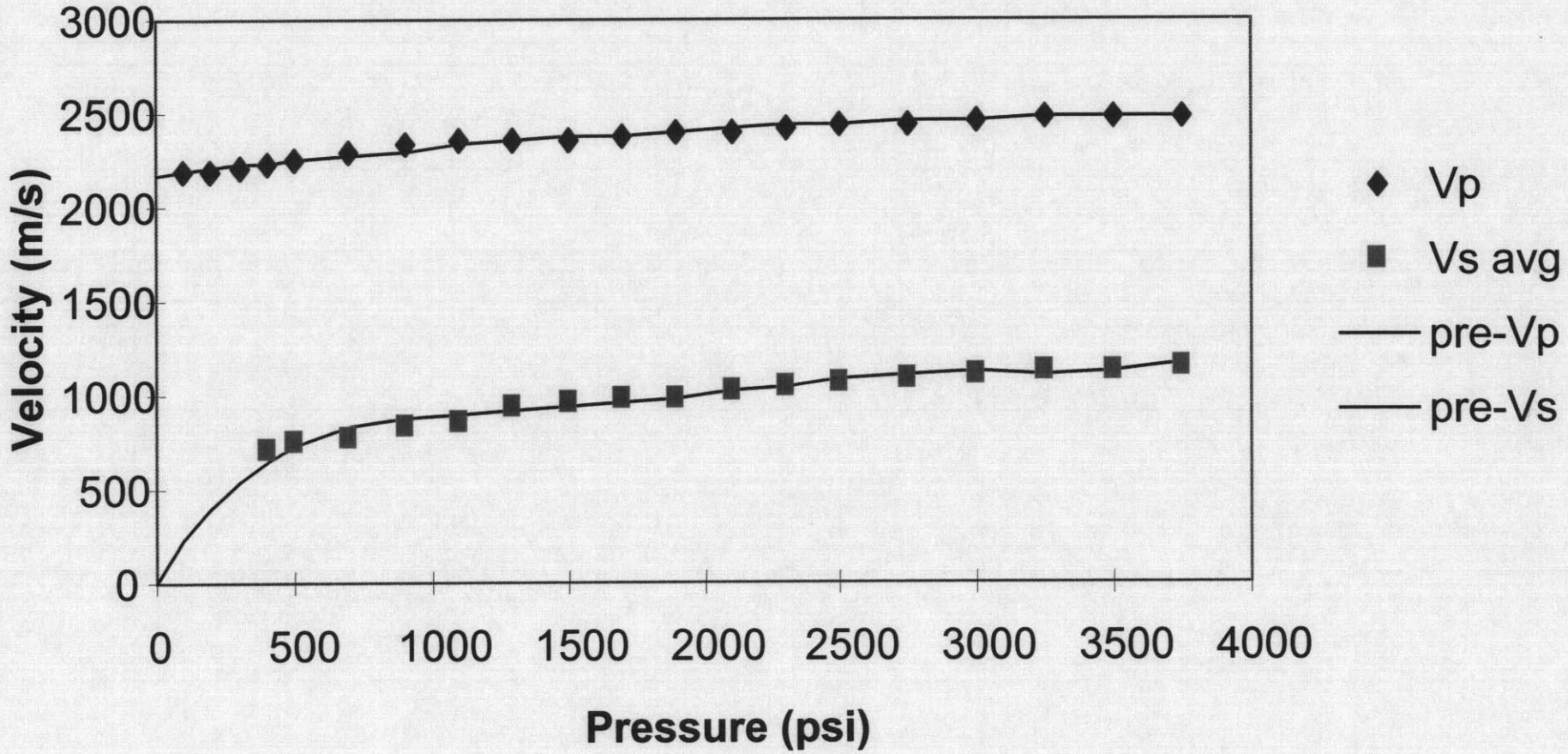

Figure 10. Brine-Saturated Sand Pack: Polynomial fits to water-saturated velocities versus effective pressure. The shear-wave velocity fit is constrained to go through zero velocity at zero effective pressure. The shear-wave polarizations are averaged to give a single velocity at each pressure.

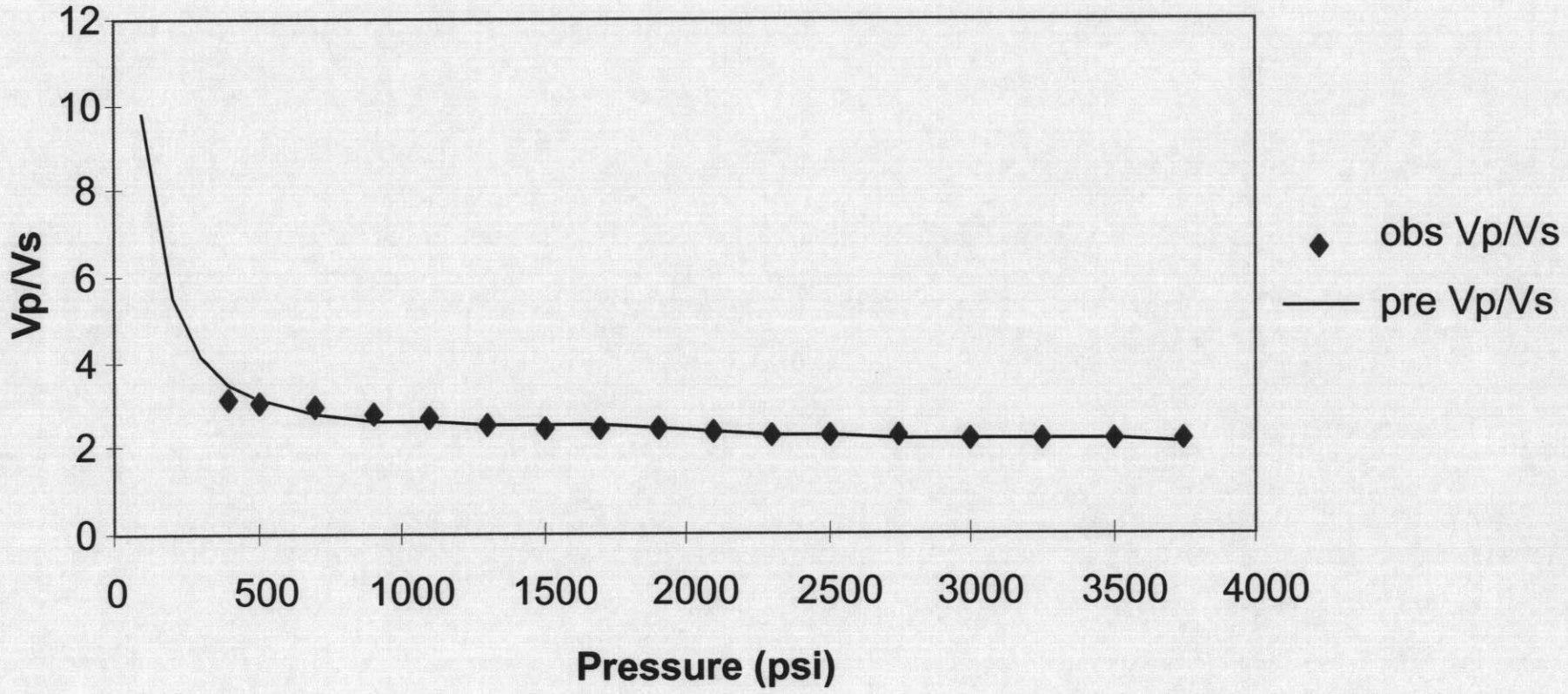

Figure 11. Brine-Saturated Sand Pack: Vp/Vs from Vp and Vs polynomial fits to clean sand pack data. Note that Vp/Vs increases dramatically below 400 psi which is also the lower limit of the shear-wave velocity measurements. Thus, the location of the Vp/Vs increase is governed by the polynomial fit (constrained by Vs = 0 at zero pressure) and not the data in this range.

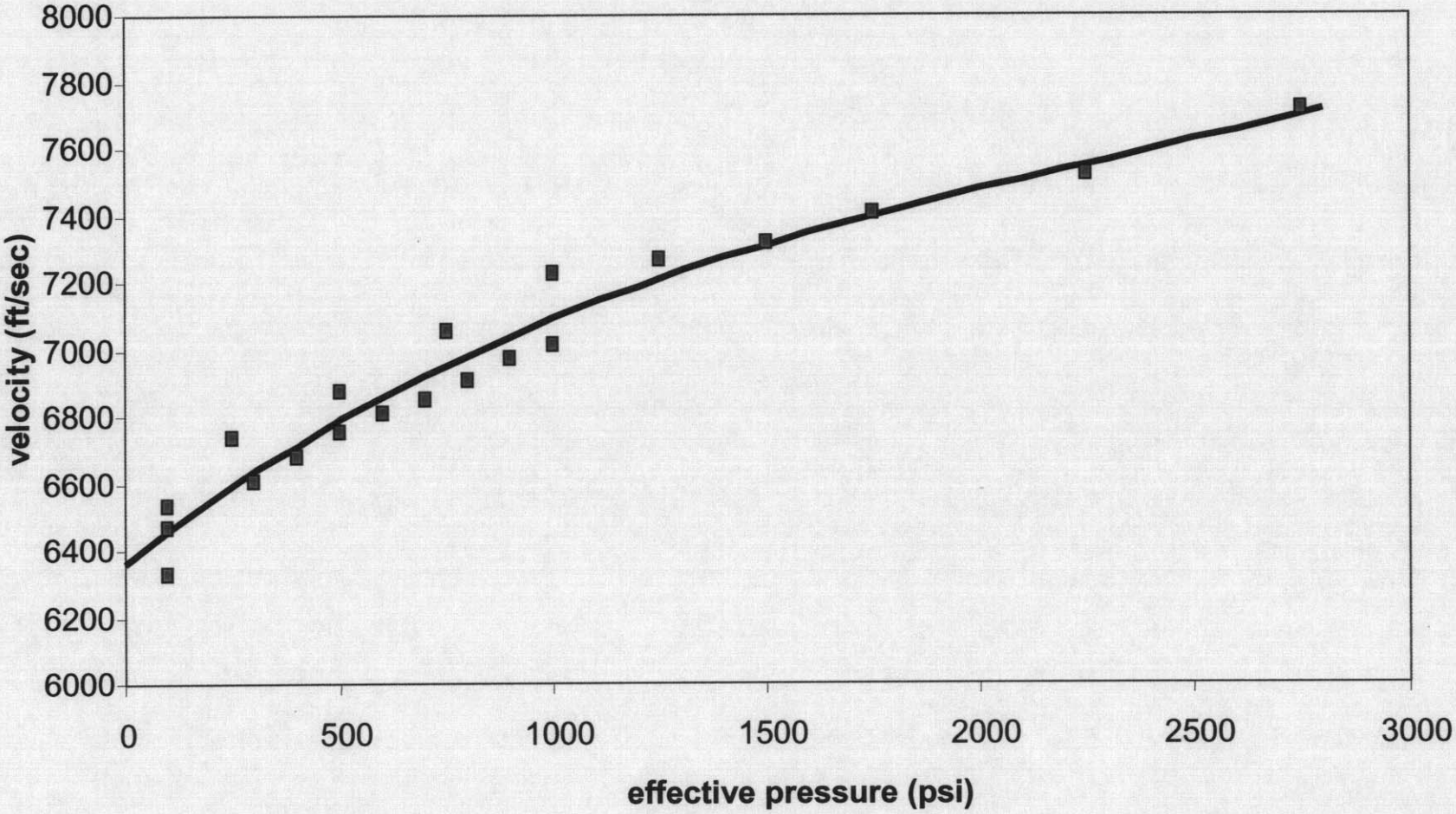

Figure 12. Saturated Vp: Saturated P-wave velocity measurements for 8 percent montmorillonite-sand mixtures and polynomial fit.

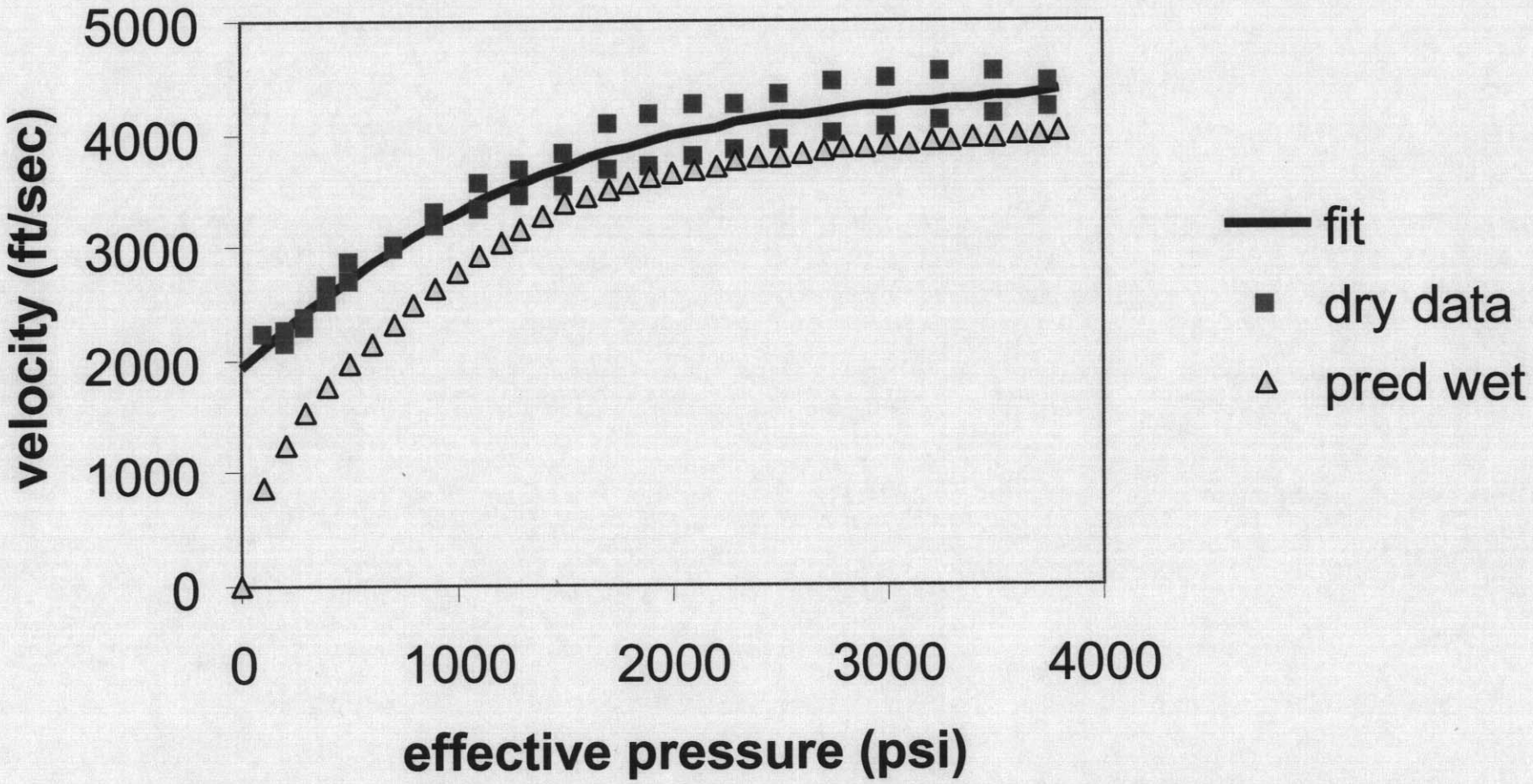

Figure 13. Predicted Vs: Predicted saturated shear-wave velocities using dry measurements and fluid substitution. The saturated modulus is assumed to vary linearly between zero at zero effective stress and the dry shear modulus at 1000 psi and above.

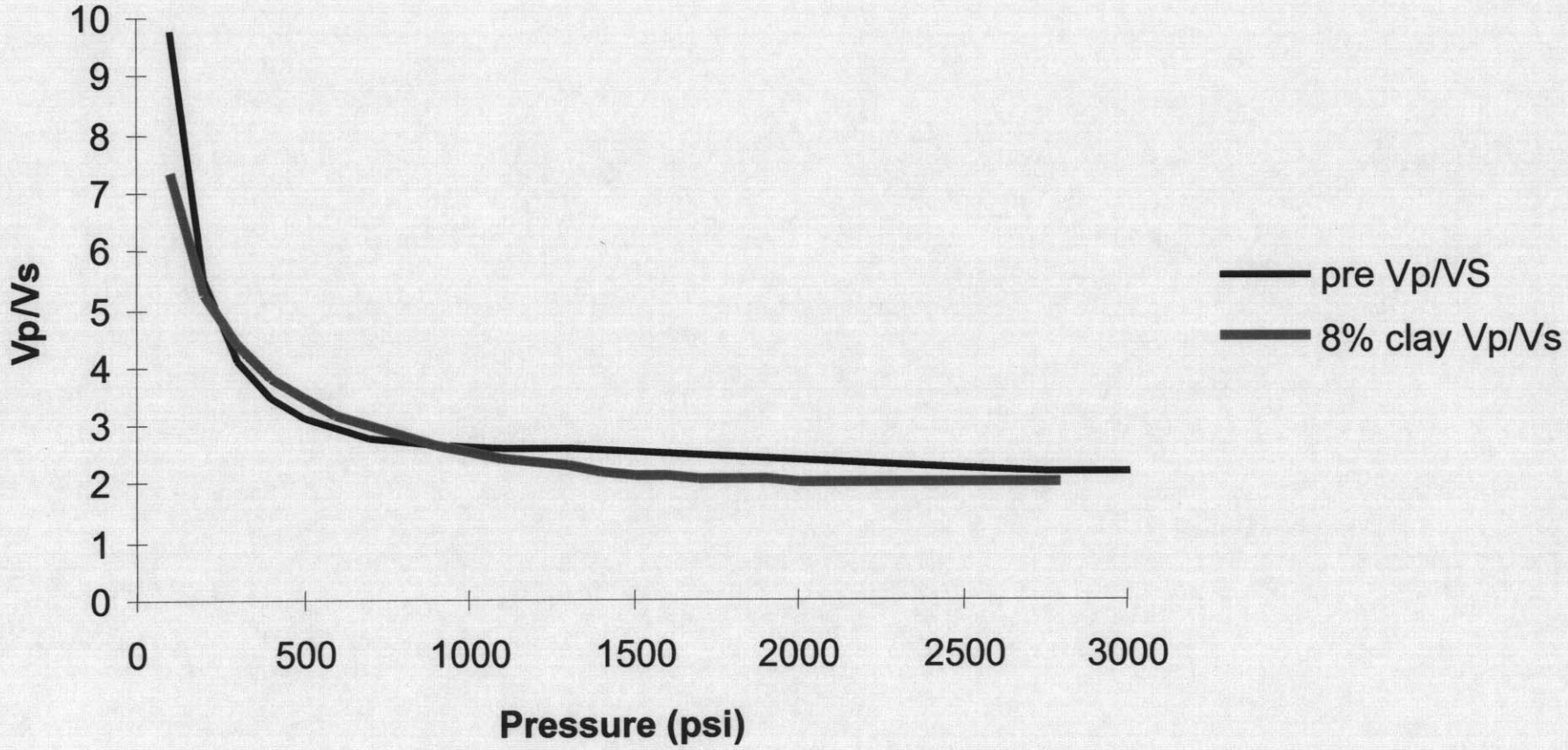

Figure 14. Brine-Saturated Clean and Dirty Sand Packs: Derived Vp/Vs versus pressure trend for clay mixture compared to clean sand trend. A small percentage of clay does not appear to change the trend significantly.

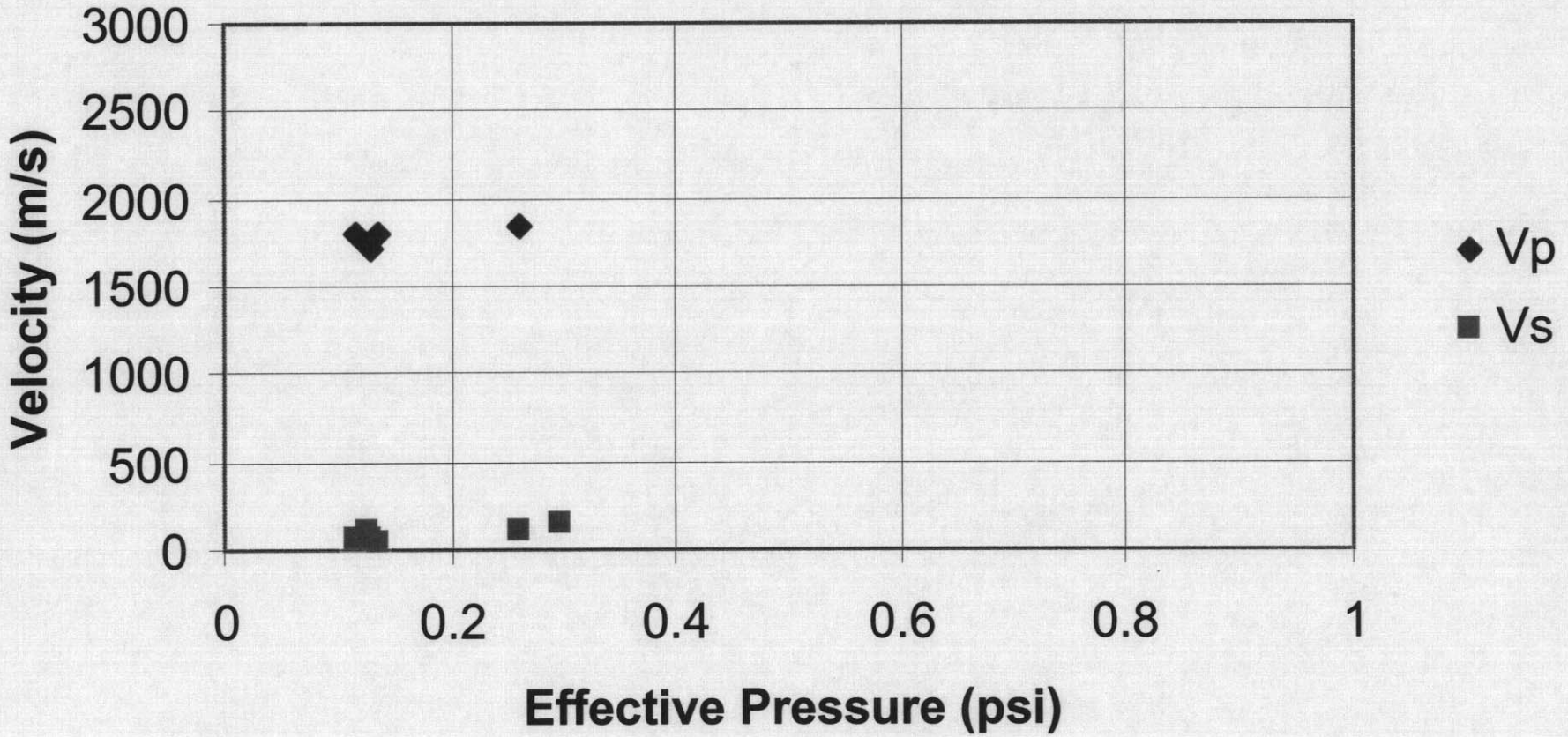

Figure 15. Bender Data: Velocities measured with bender bar transducers for sands at low effective pressure (from Bell, 1979).

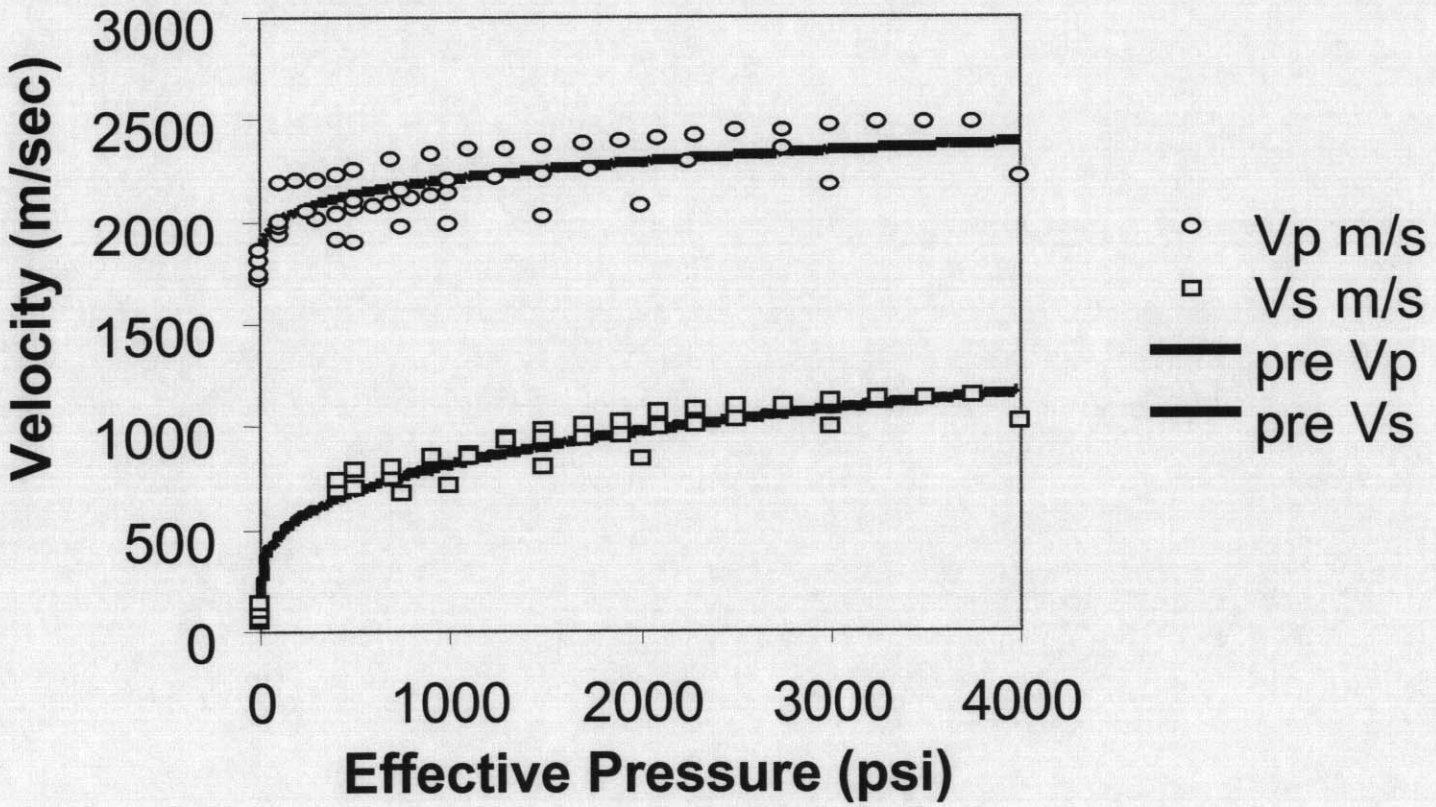

Figure 16. Saturated Sand Velocity Measurements: Compilation of fully water-saturated Vp and Vs measurements from this study and from the literature. Measurements at nearly zero effective stress are from Bell (1979). Domenico's (1977) measurements are included. Power fits are forced through Wood's equation and Vs=0 at zero effective pressure.

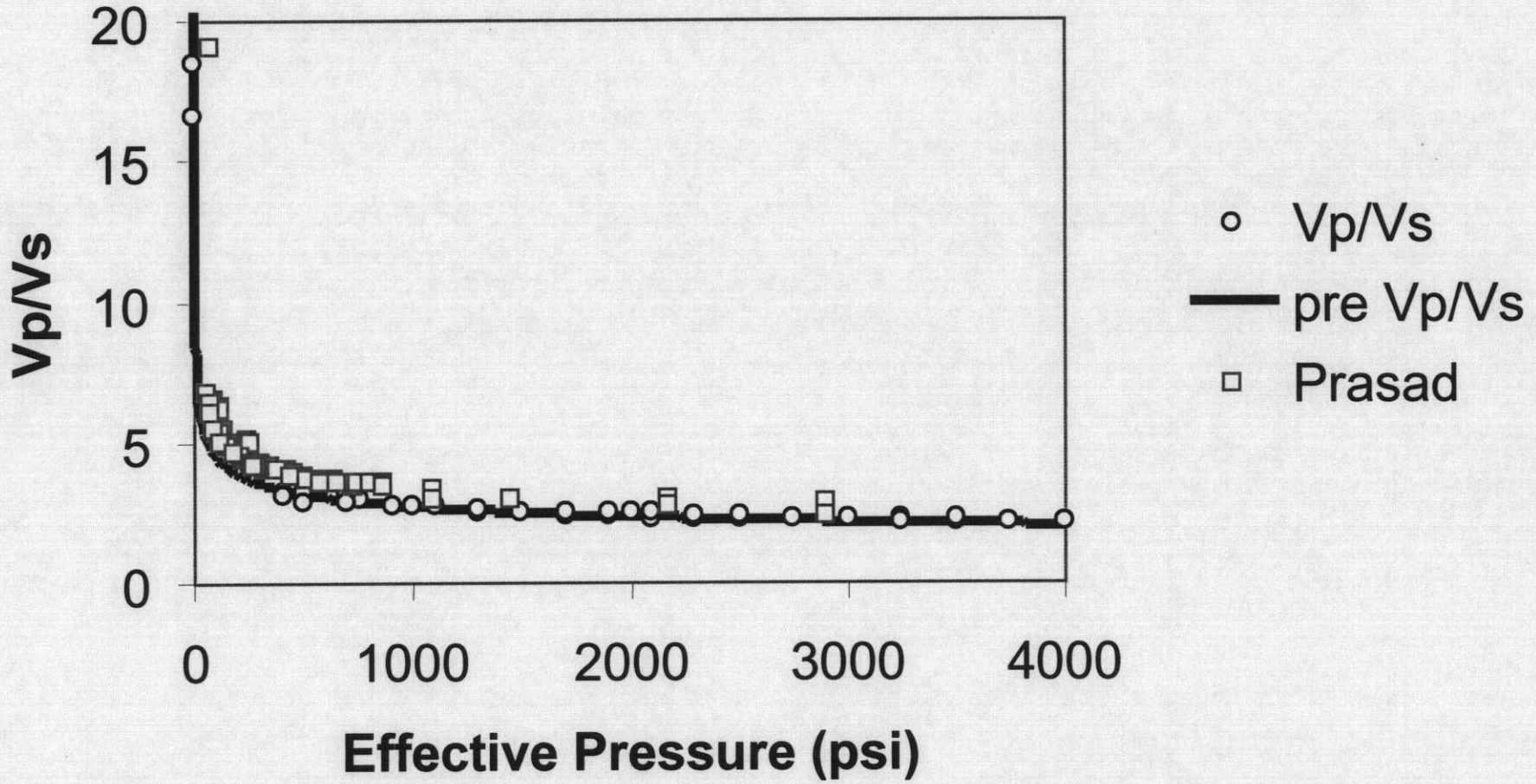

Figure 17. Saturated Vp/Vs for Sand Packs: Water-saturated Vp/Vs measurements, power fit, and data of Prasad (in press).

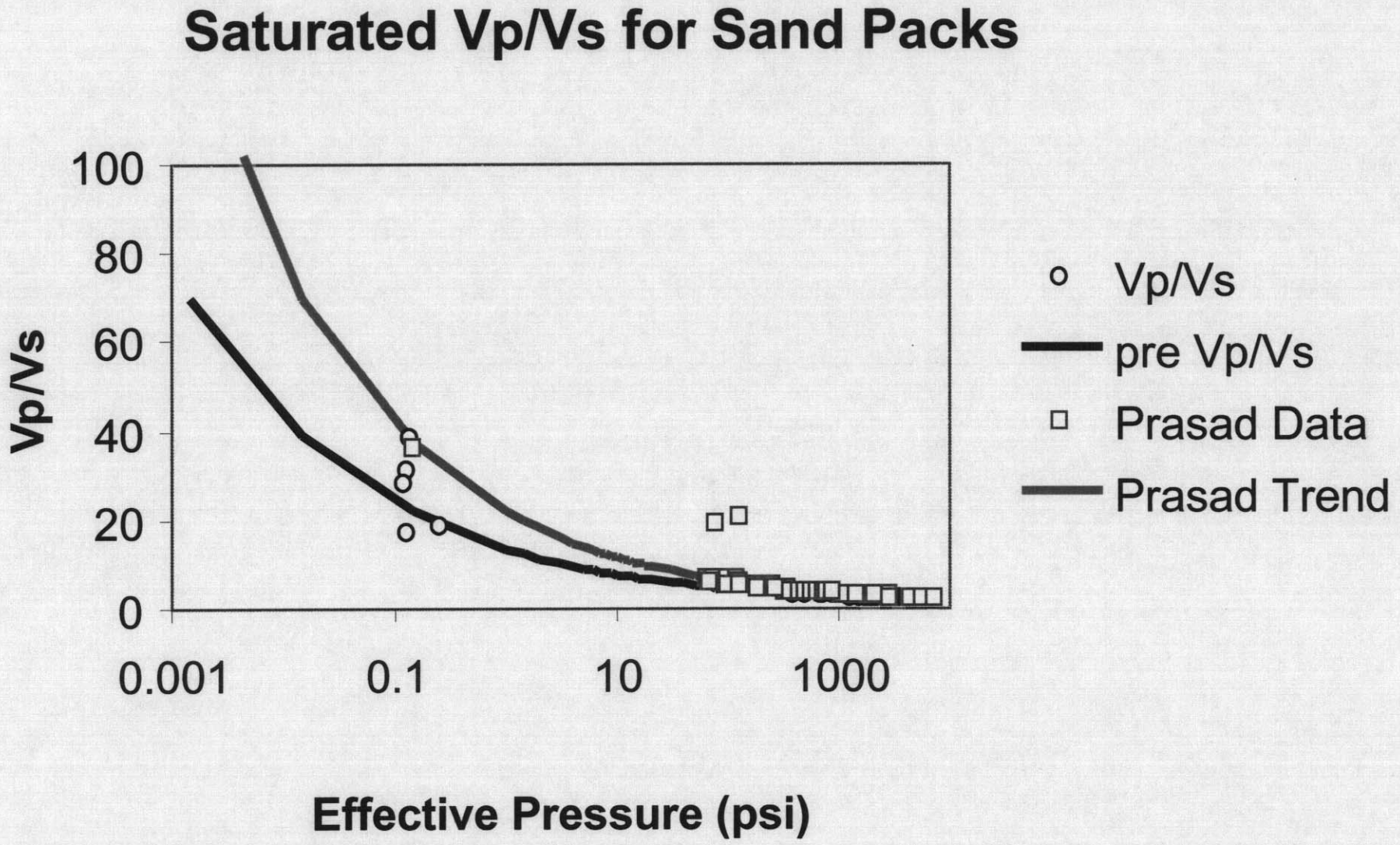

Figure 18. Saturated Vp/Vs for Sand Packs: Logarithmic pressure scale for data in Figure 17 emphasizes difference between power fit and Prasad trend at low effective pressure.

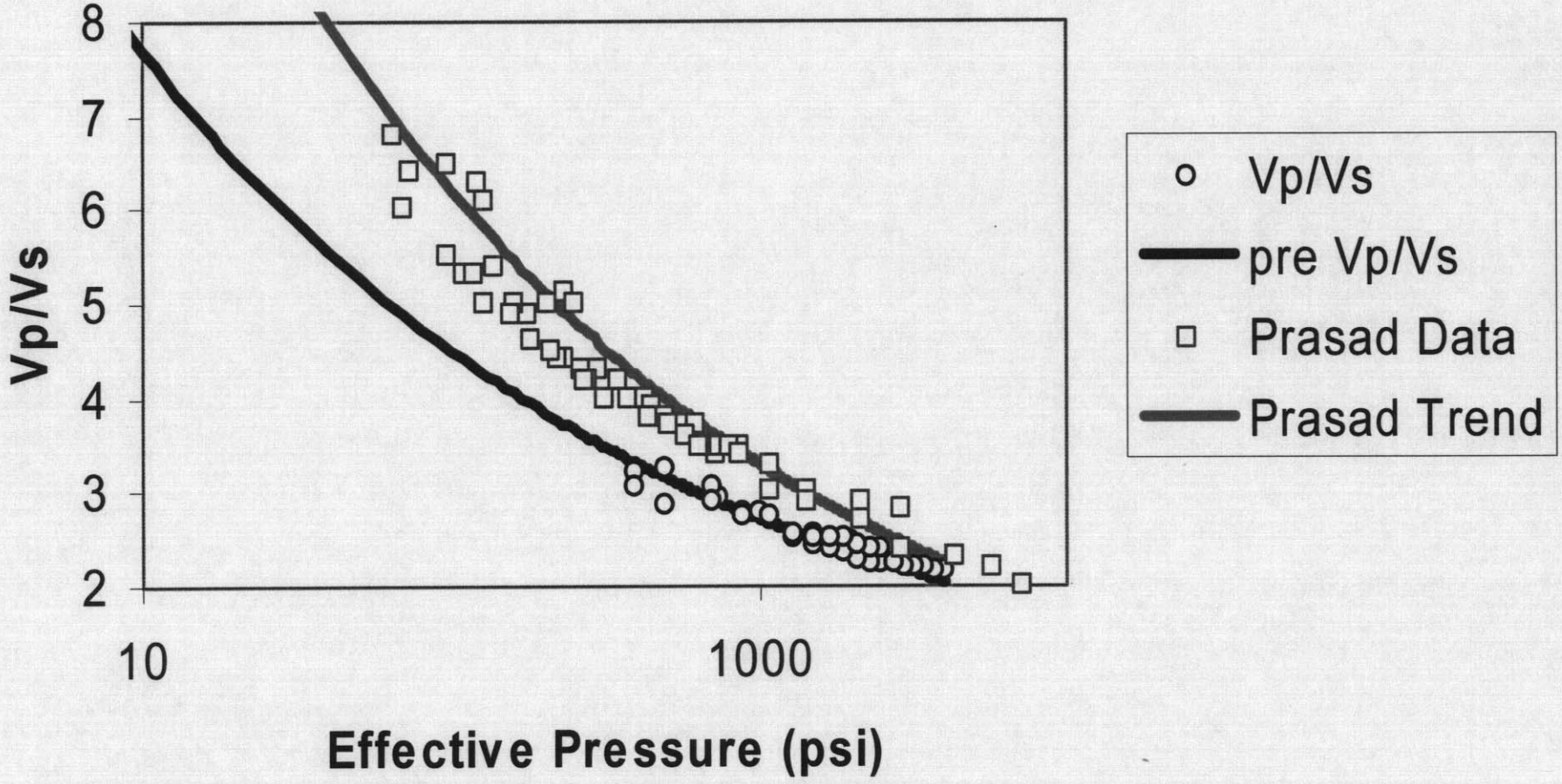

Figure 19. Saturated Vp/Vs for Sand Packs: Expanded scale version of Figure18 shows large uncertainty in Vp/Vs trends at a given effective pressure. The Prasad trend is dominated by a few high Vp/Vs ratios shown in Figure18. Note that Prasad's data show a higher Vp/Vs at a given pressure suggesting that the samples from this study may represent more compact mixtures.

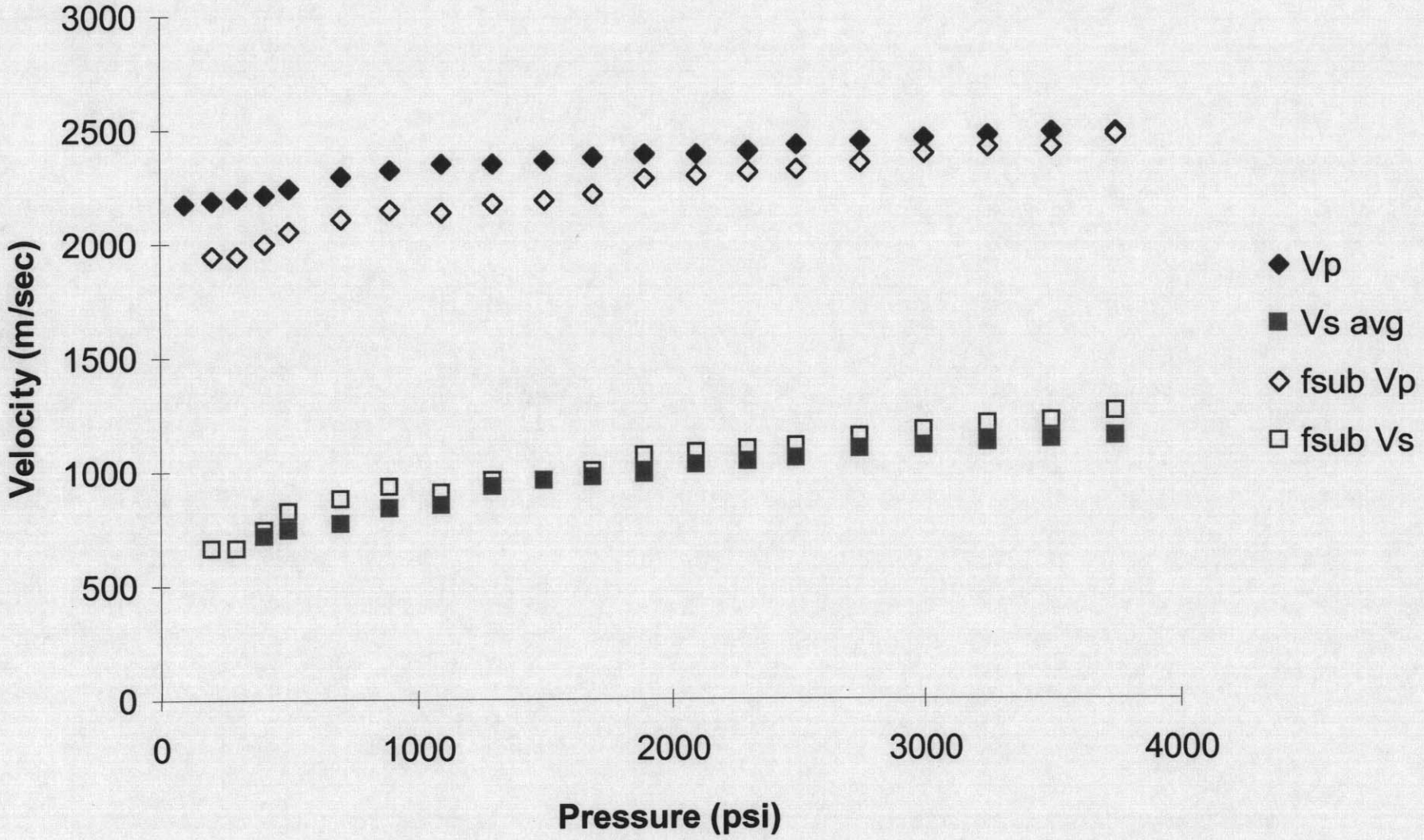

Figure 20. Fluid Substitution for Clean Sand Pack: Measured water-saturated velocities and fluid-substituted velocities from dry measurements for clean sand pack. Although the observed and predicted shear-wave velocities agree well, the measured P-wave velocities are higher suggesting dispersion or frame modulus changes with saturation. The fluid substituted velocities indicate a lower Vp/Vs ratio than do the measured velocities.

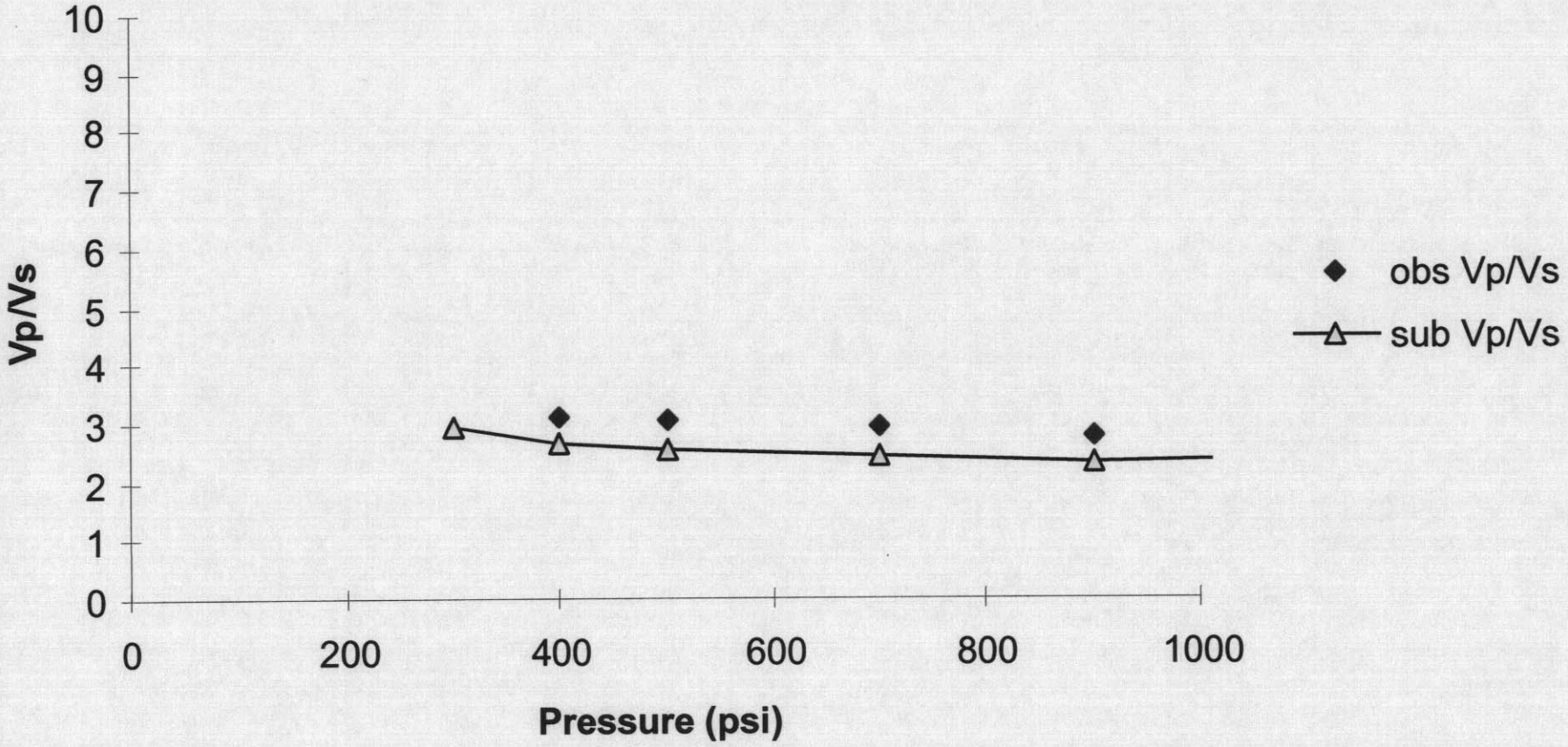

Figure 21. Brine-Saturated Sand Pack: Measured (blue symbols) and fluid-substituted (yellow triangles) Vp/Vs ratio for clean sand pack. The fluid substitution gives a lower Vp/Vs ratio.

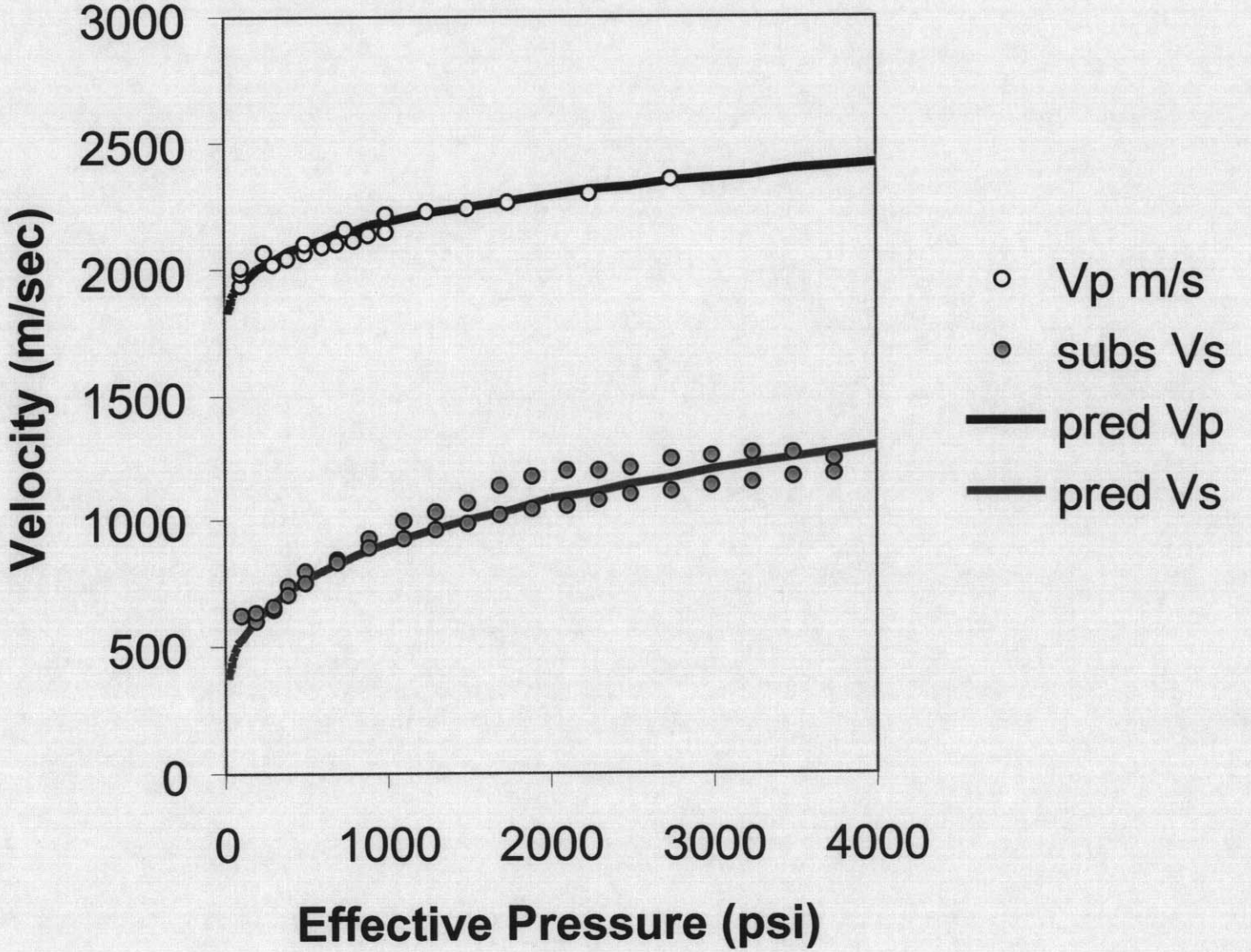

Figure 22. Saturated Velocity Measurements 8 Percent Clay-Sand Mixture Power law fits for 8 percent montmorillonite-sand mixtures for fully water-saturated Vp measurements and fluid substituted Vs from room dry measurements.

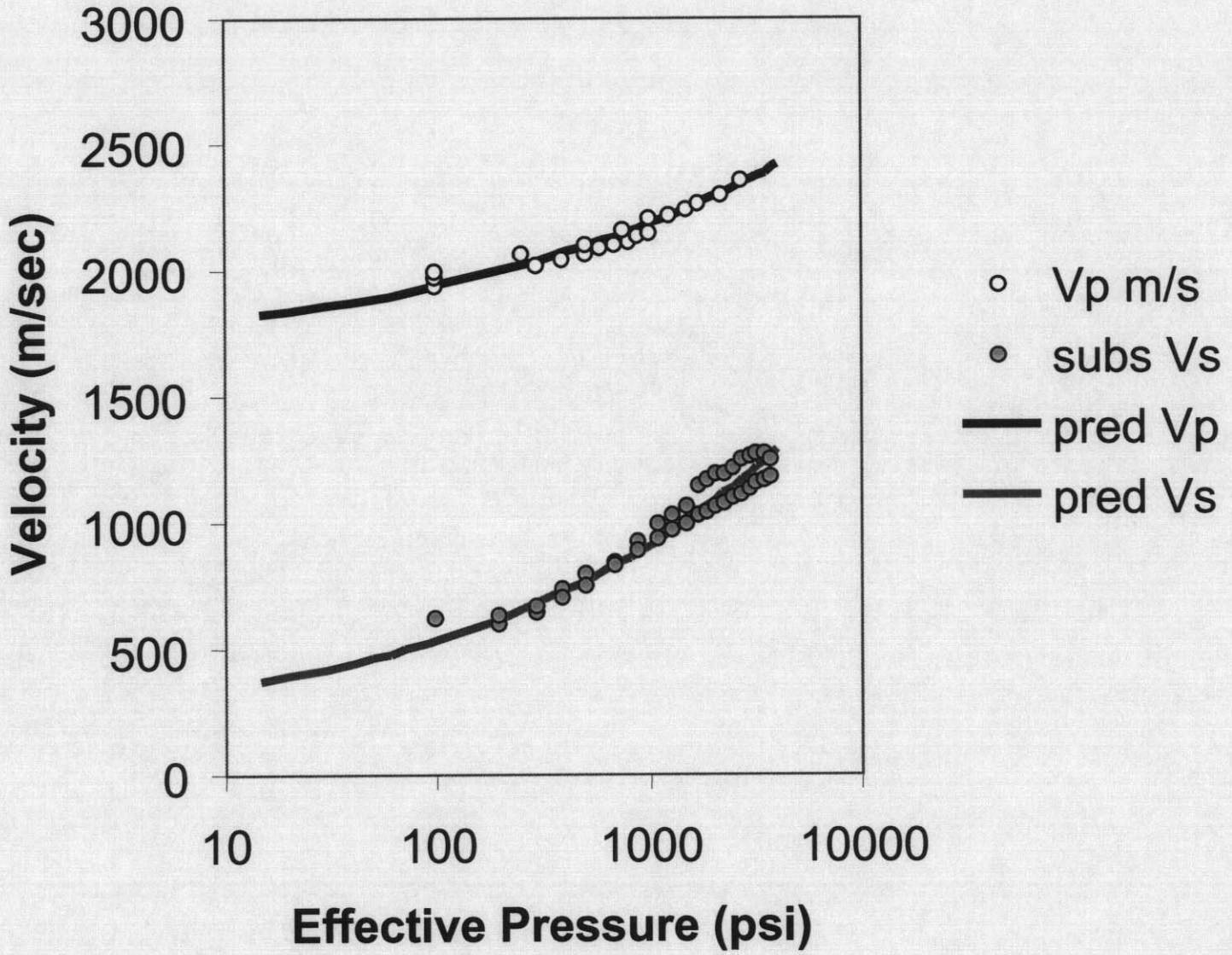

Figure 23. Saturated Velocity Measurements 8 Percent Clay-Sand Mixture: Figure 22 plotted with a logarithmic pressure axis.

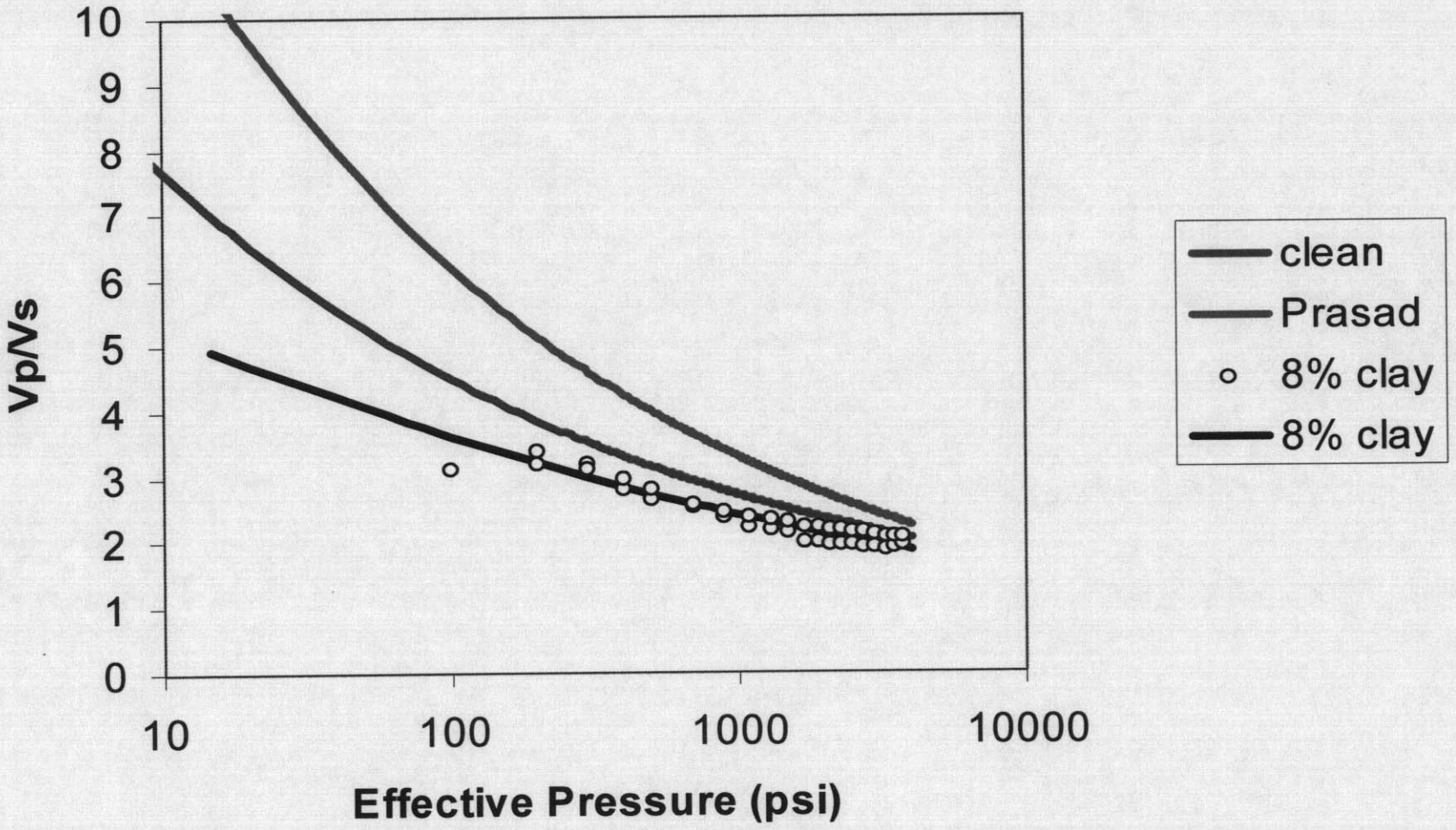

Figure 24. Saturated Vp/Vs for 8 percent sand-clay mixture determined from Vp and Vs power law fits to clay-sand mixture measurements shown in Figures 22 and 23. Note that the clay reduces Vp/Vs at a given pressure.

Figure 25. PP reflection cdp gathers for a 50 ft shale layer and 5 different SWF sands. The SWF sands have the properties appropriate for the indicated effective stress.

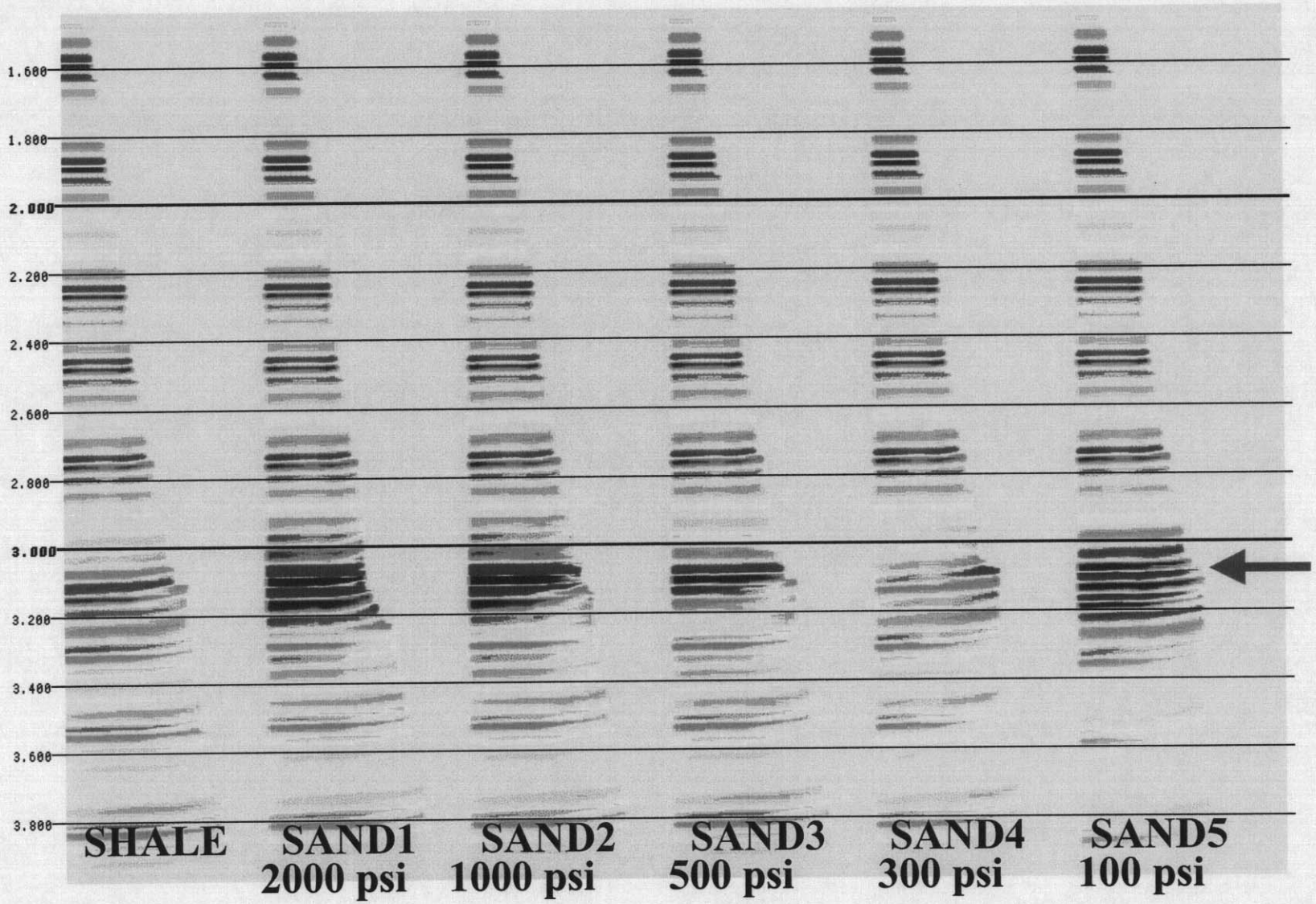

Figure 26. PS reflection cdp gathers for the 50 ft shale layer and 5 different SWF sands. The SWF sands have the properties appropriate for the indicated effective stress.

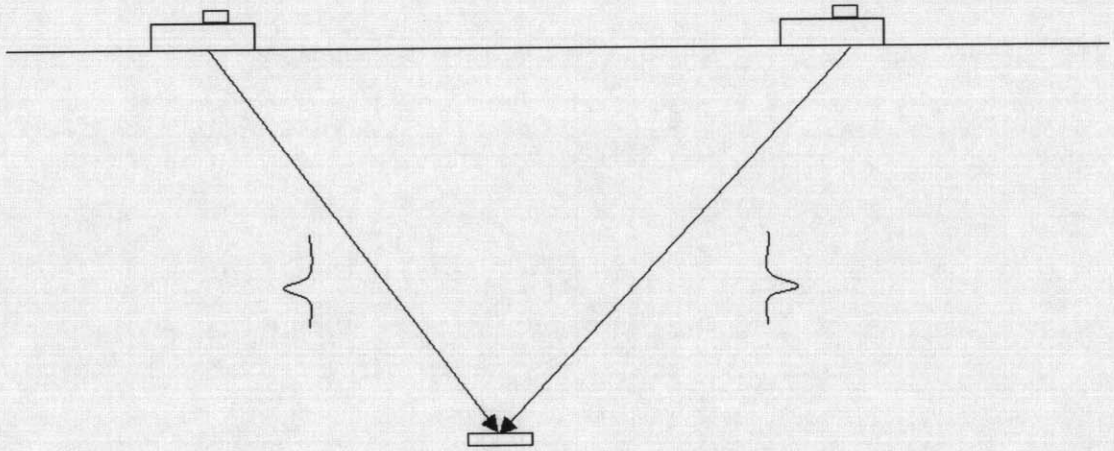

Figure 27. This cartoon shows that shots on the opposite side of an inline geophone will produce opposite polarity signals.

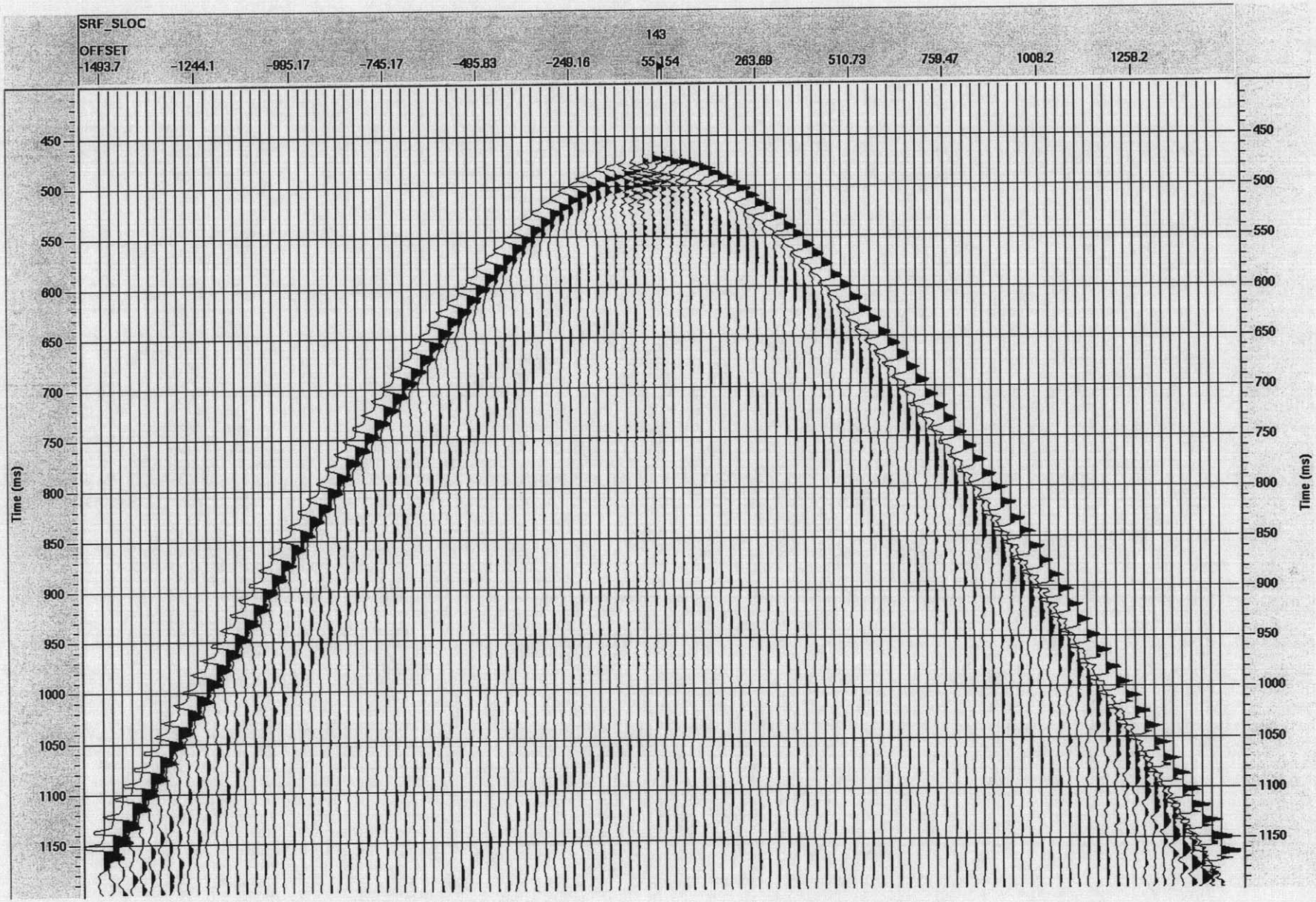

Figure 28. Ram Powel common inline receiver gather showing the reversal of polarity as the offset changes from positive to negative. The null point is two shots from the zero offset from the geometry.

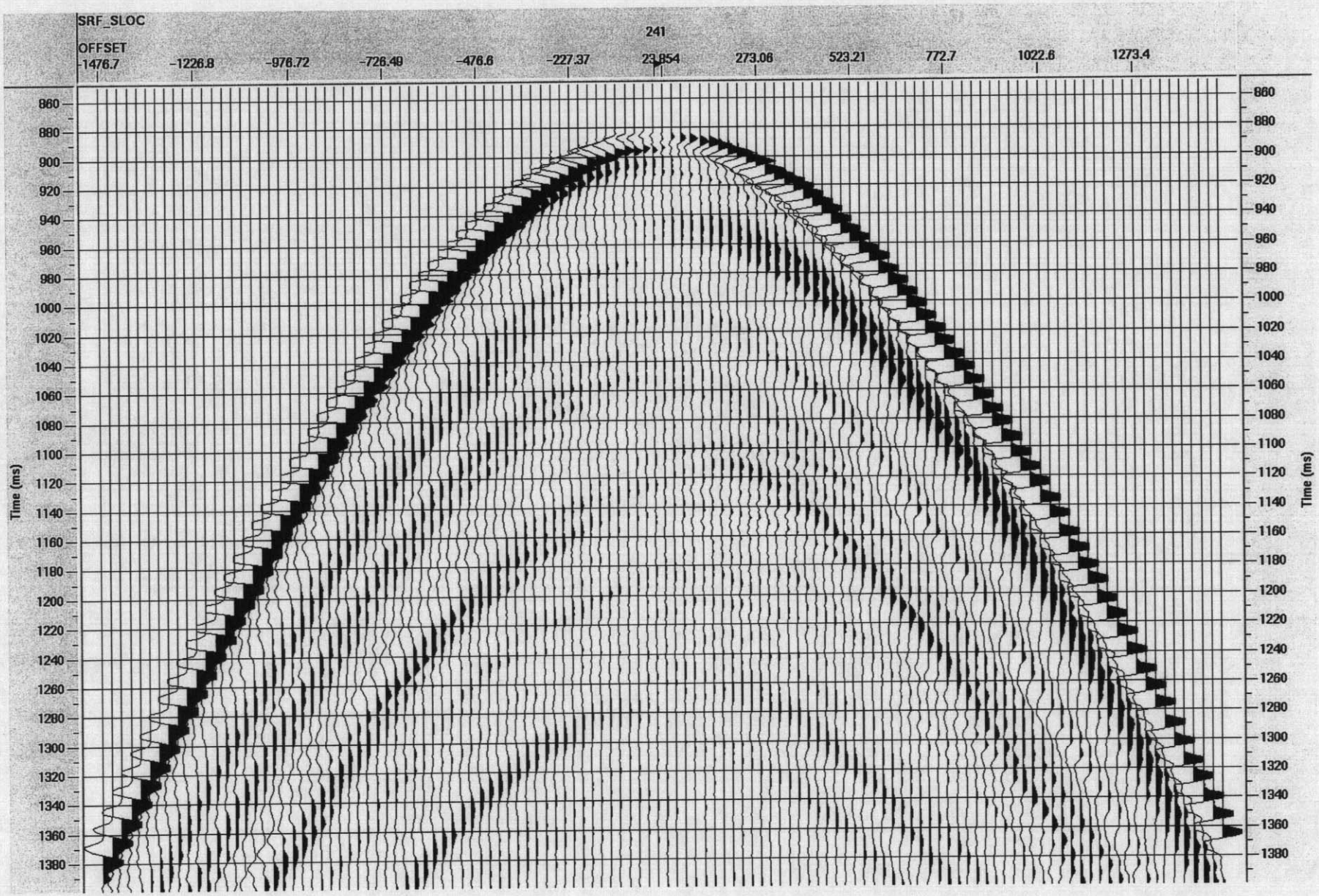

Figure 29. King Kong common inline receiver gather showing the reversal of polarity as the offset changes from positive to negative. The null point is less than one shot from the zero offset from the geometry.

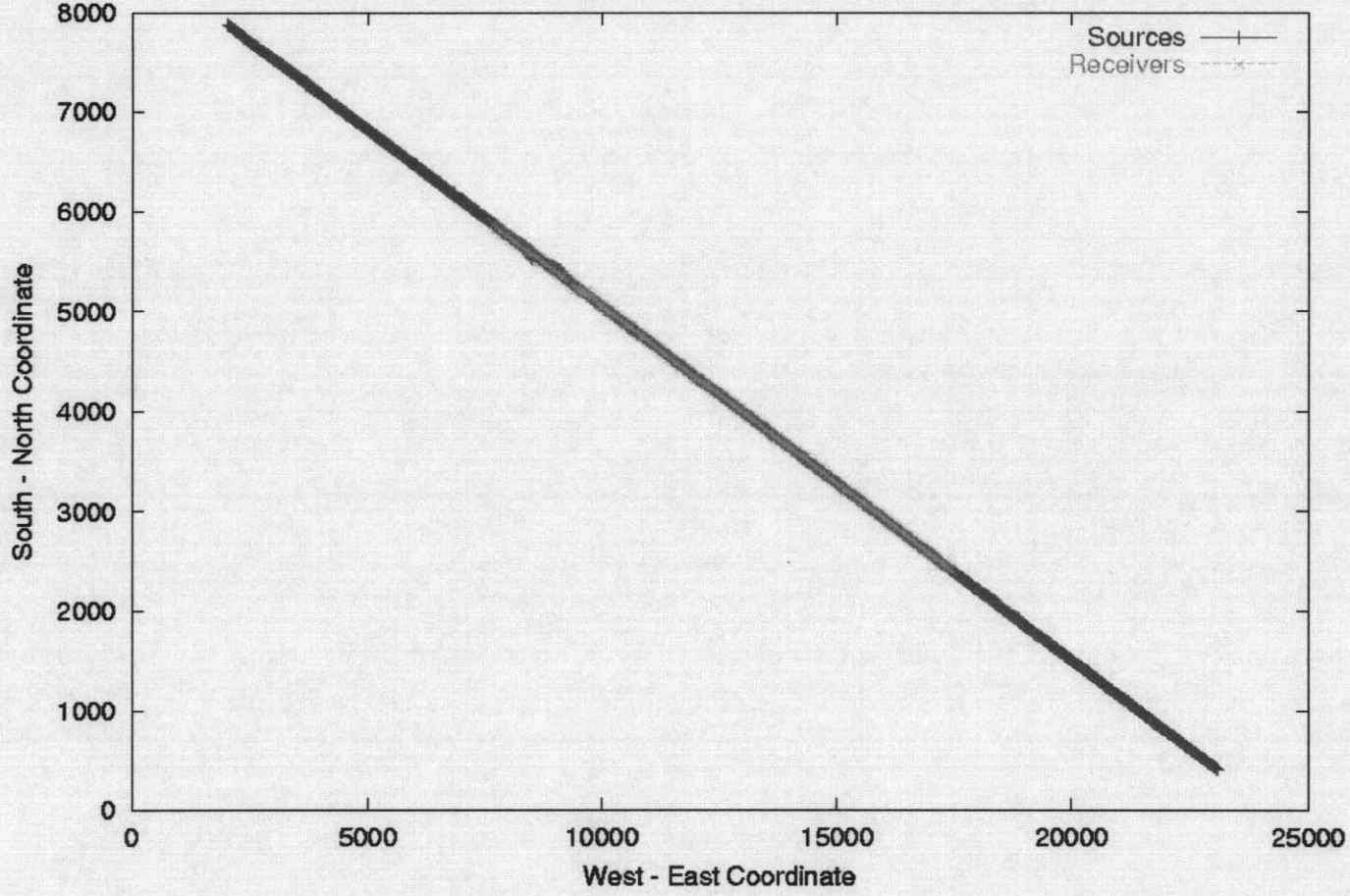

Figure 30. King Kong Geographic Coordinates: Plot of the King Kong source and receiver lines, as determined from the geometry, in the original acquisition coordinate system.

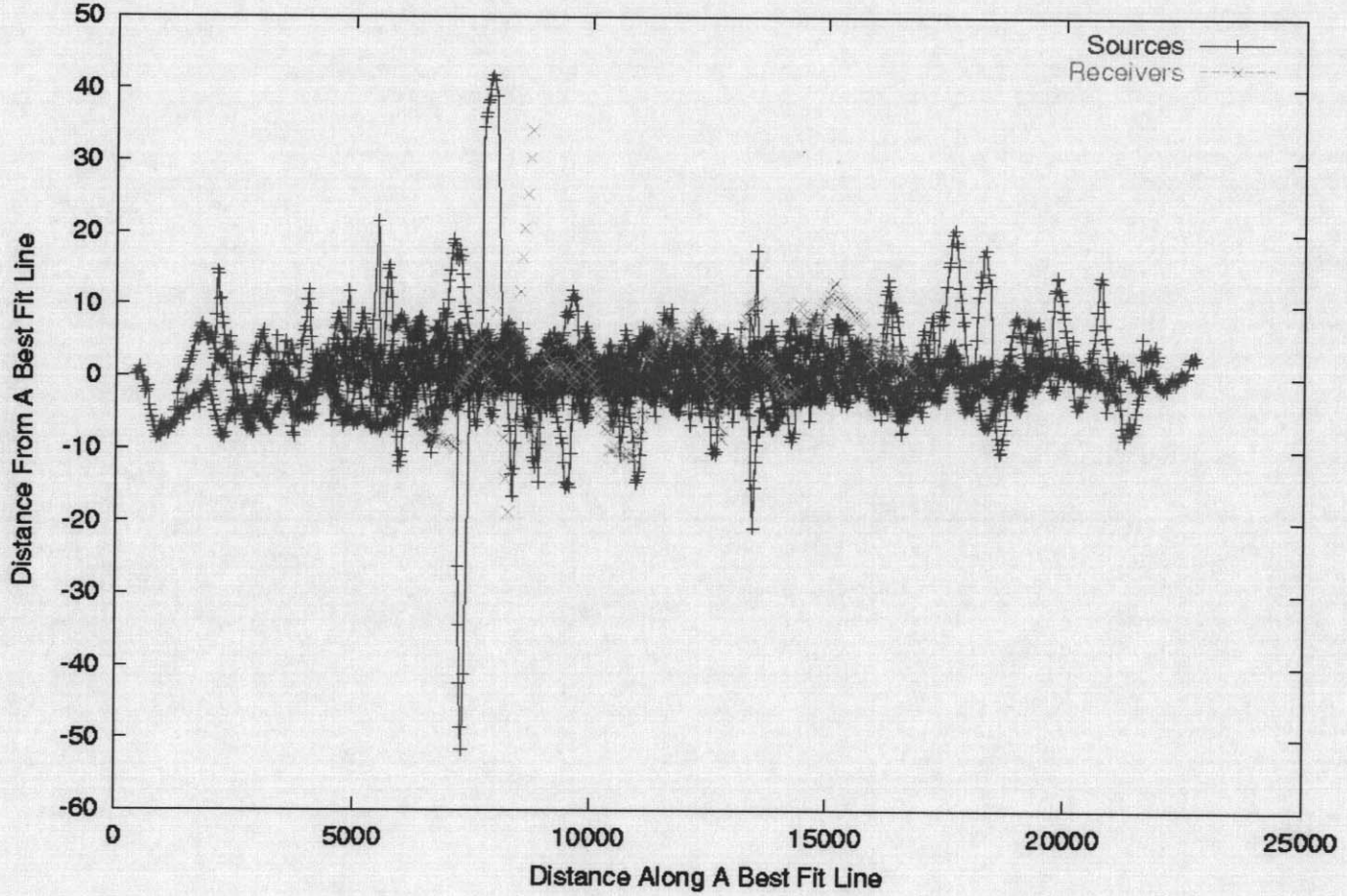

Figure 31. King Kong Inline Coordinates: Plot of the King Kong source and receiver lines in an inline-crossline coordinate system. The inline direction was determined by fitting a line to all of the source lines.

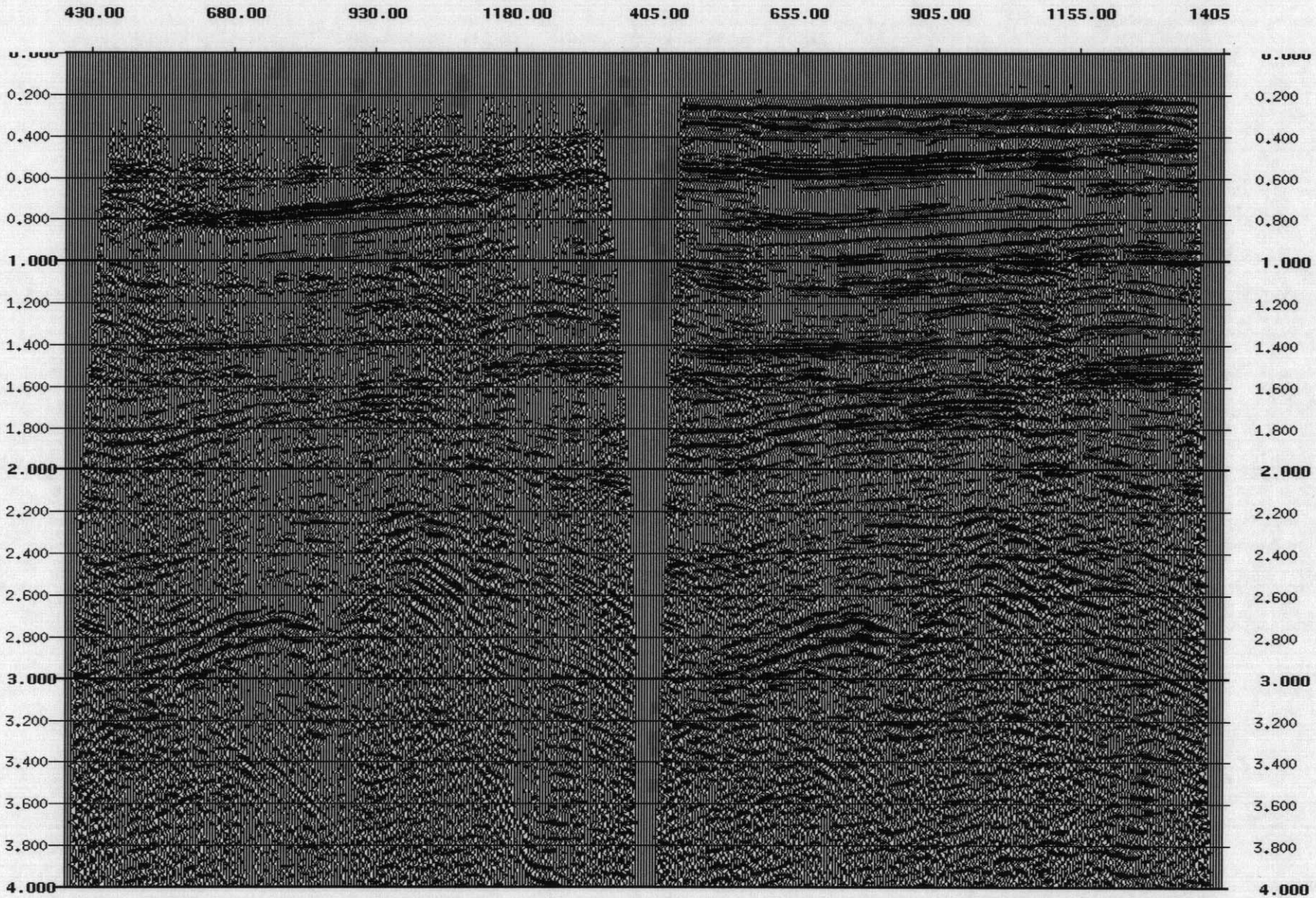

Figure 32. Comparison of King Kong p-p stacked data with and without wave equation datuming correction. Wave equation datuming was applied to the section on the left before NMO and stack. The section on the right was stacked and a bulk time shift was applied to the data to match the times in both sections.

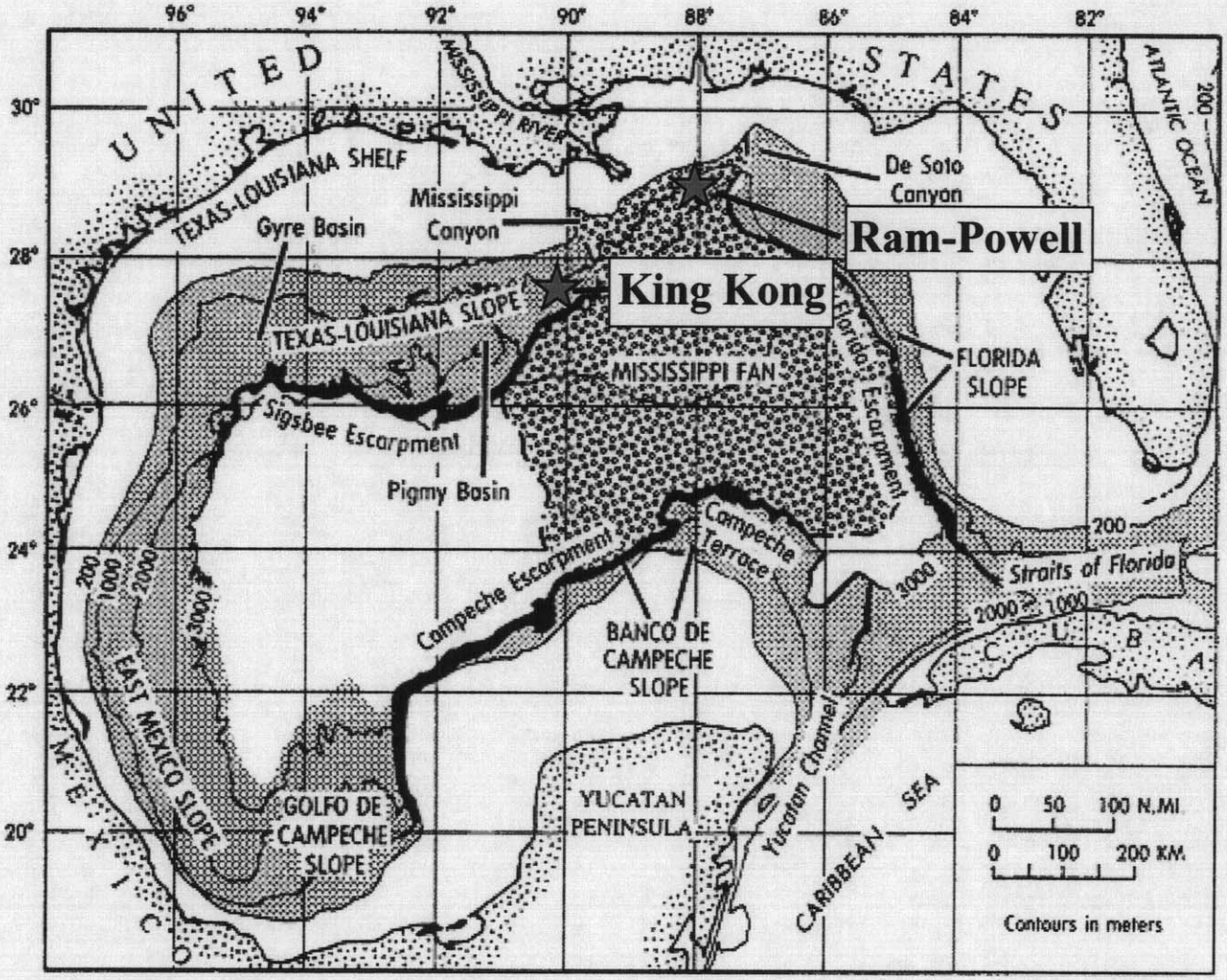

Figure 33. Physiographic setting of King Kong and Ram-Powell, the two Gulf of Mexico SWF sites (modified from Bouma et al, 1992).

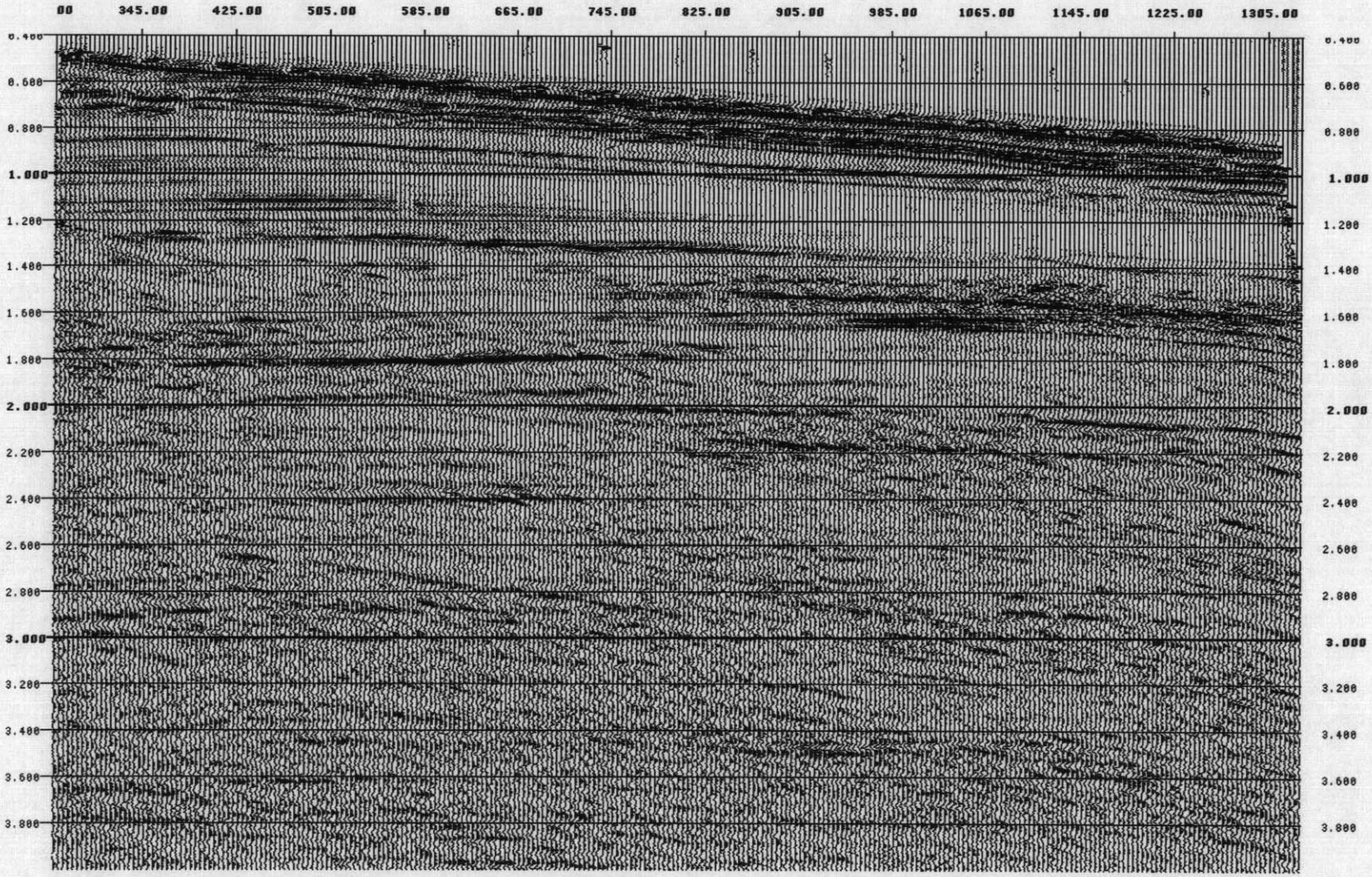

Figure 34. PP seismic data for the Ram Powell area. Notice the lack of chaotic facies in the shallow section indicates sand poor depositional setting.

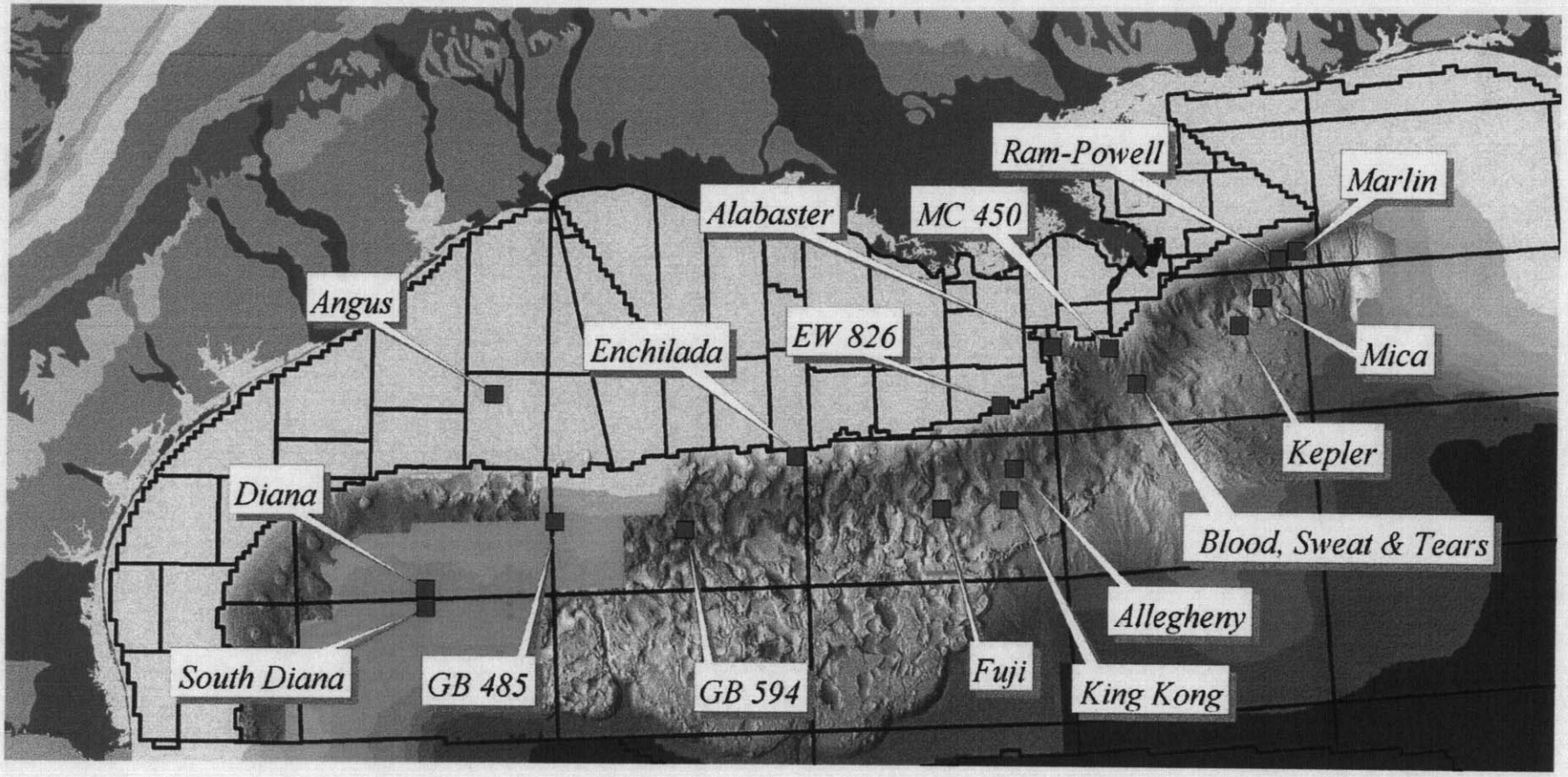

Figure 35. Gulf of Mexico Multicomponent Sites: Location map of the PGS multicomponent surveys acquired in the Gulf of Mexico.

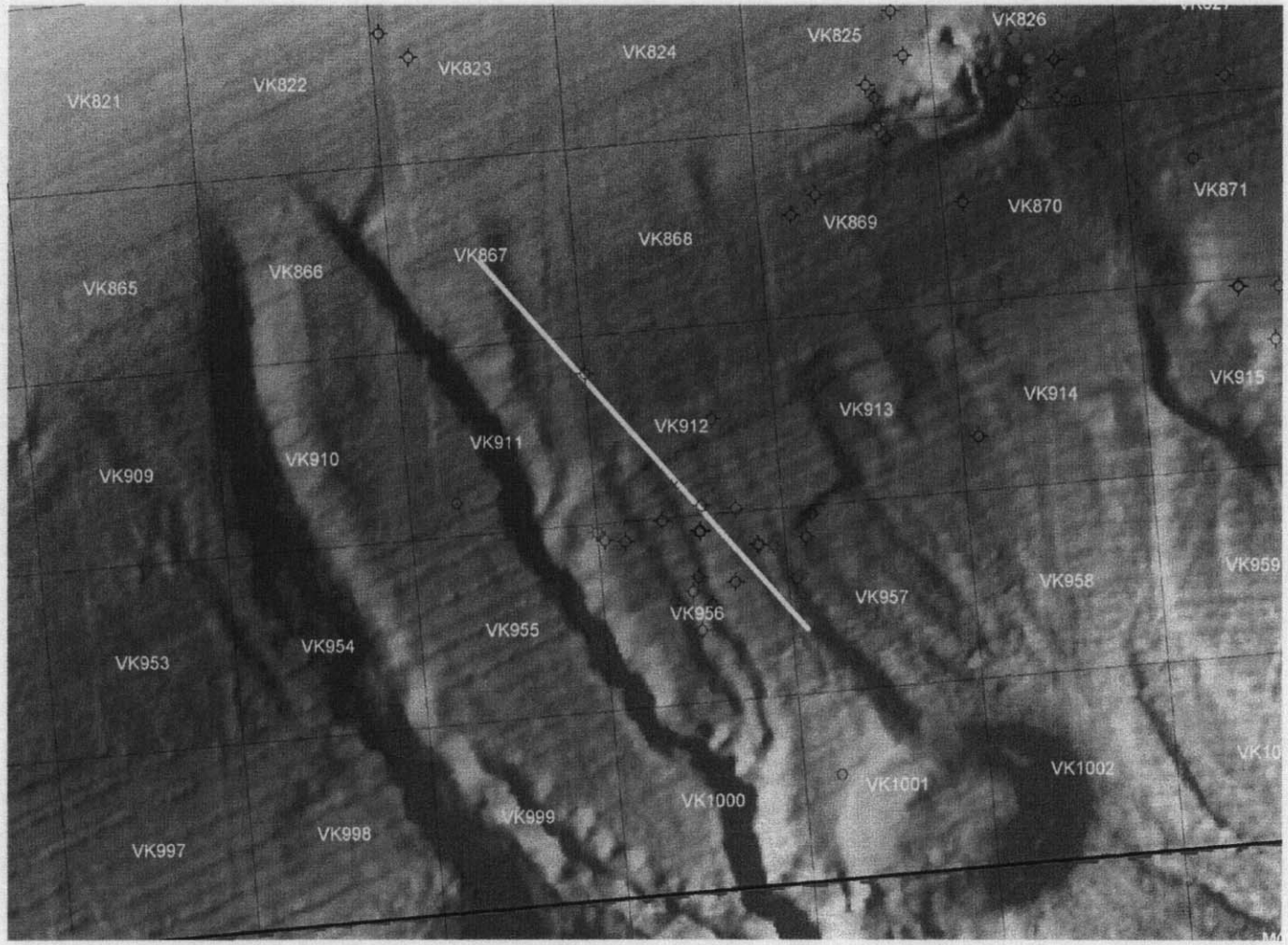

Figure 36. Location of the PGS multicomponent line in the Ram Powell area.

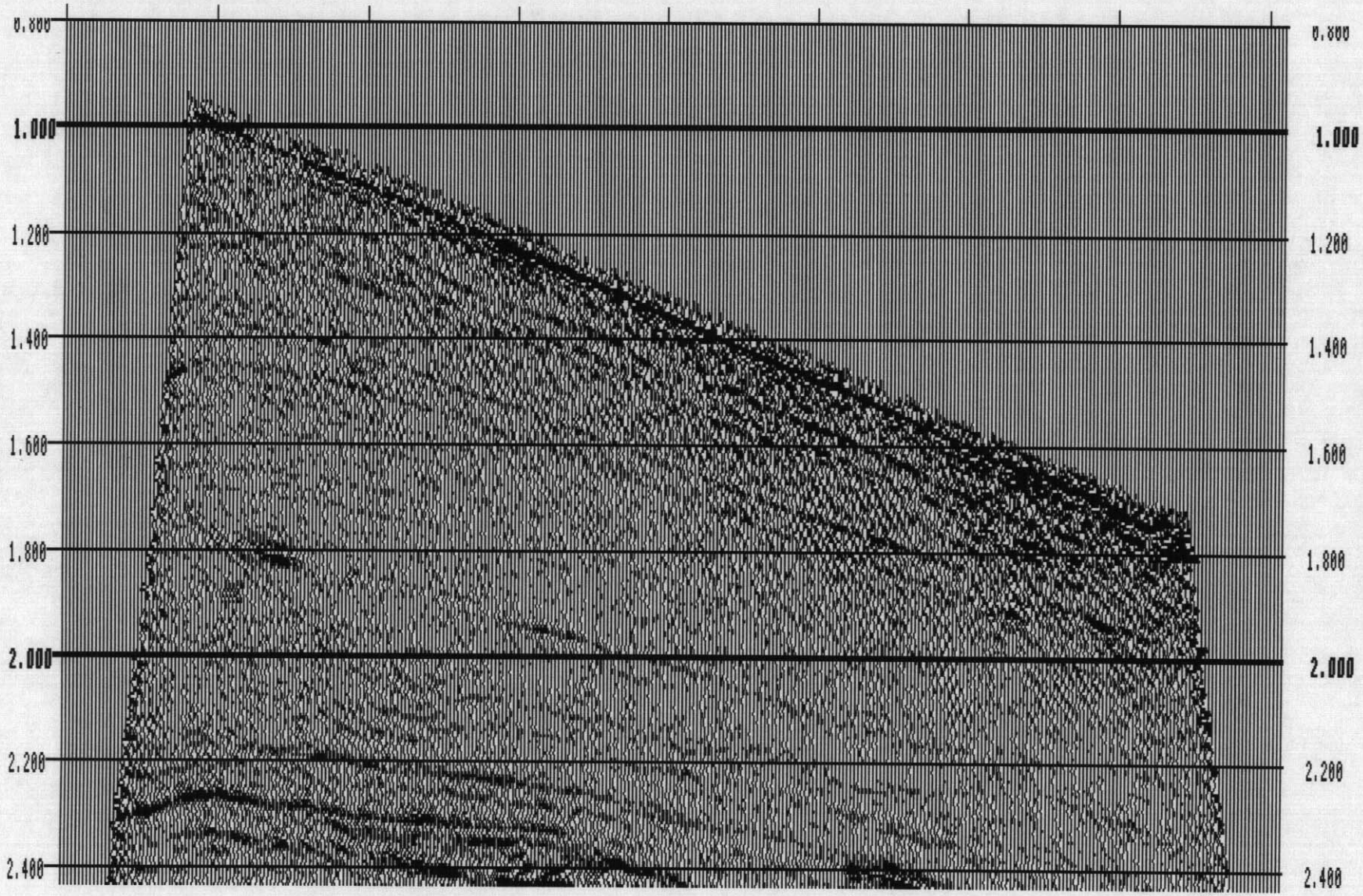

Figure 37. PP data from Ram Powell based on initial processing by PGS.

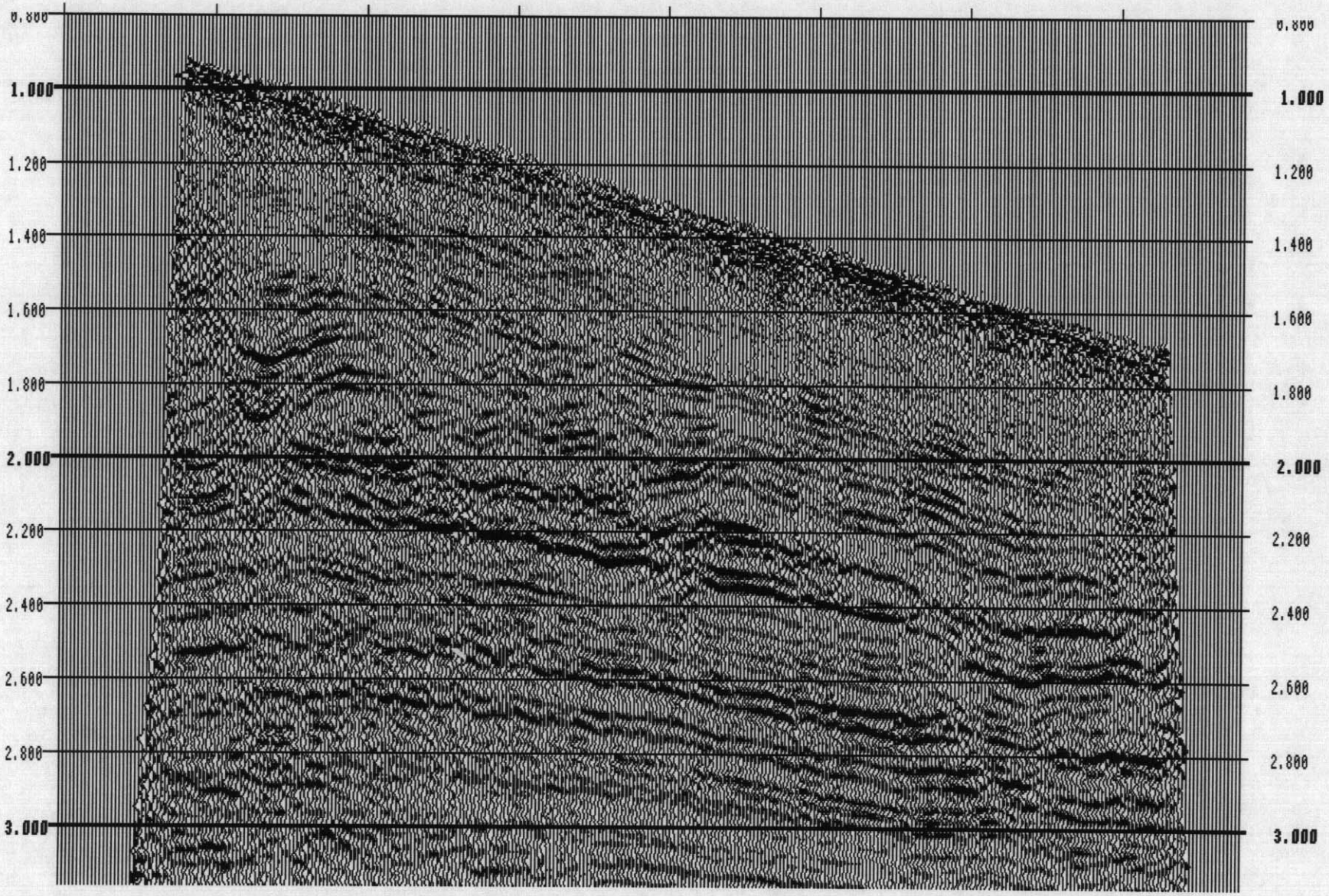

Figure 38. PS data from Ram Powell based on initial processing by PGS.

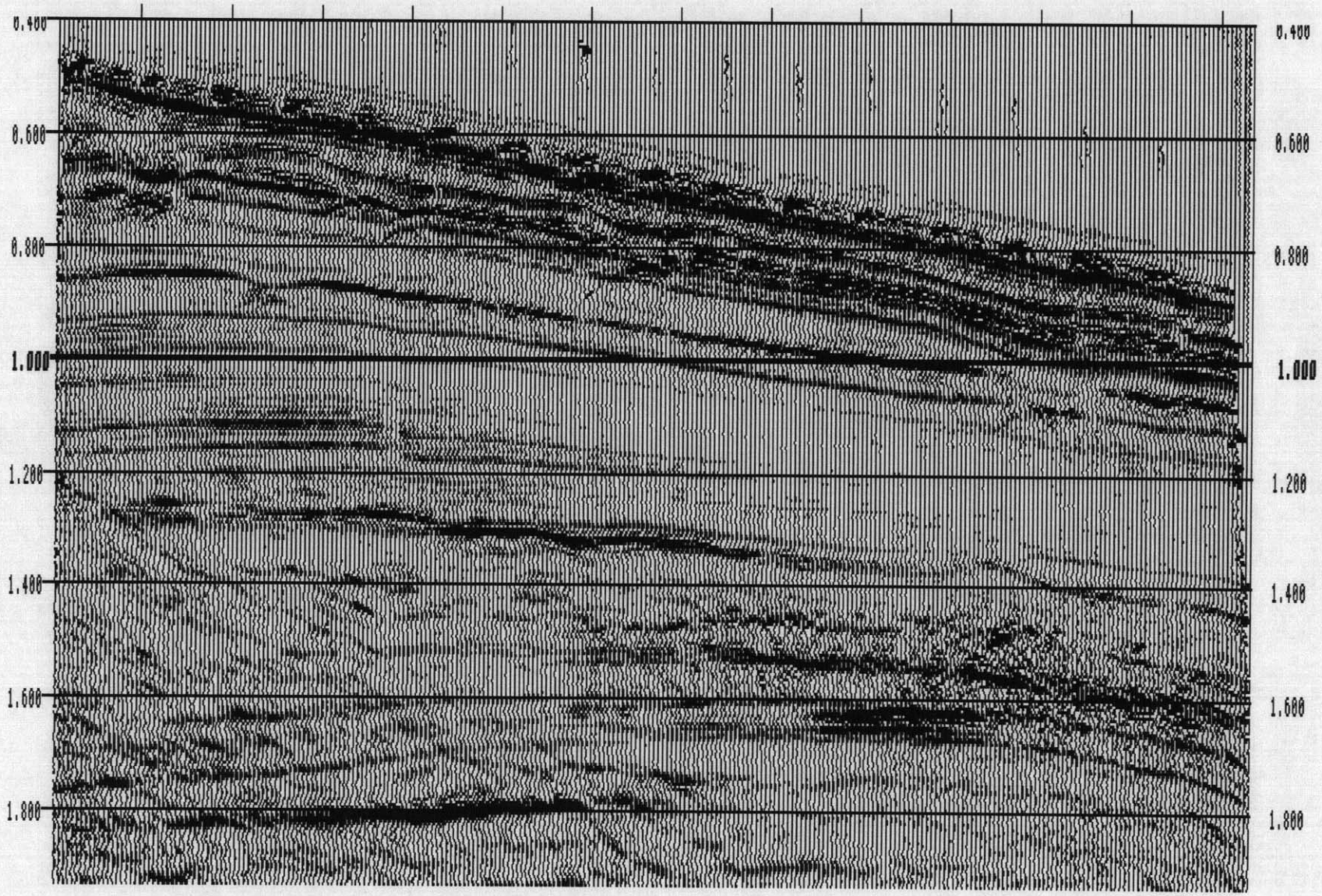

Figure 39. PP data from Ram Powell processed to enhance the shallow section.

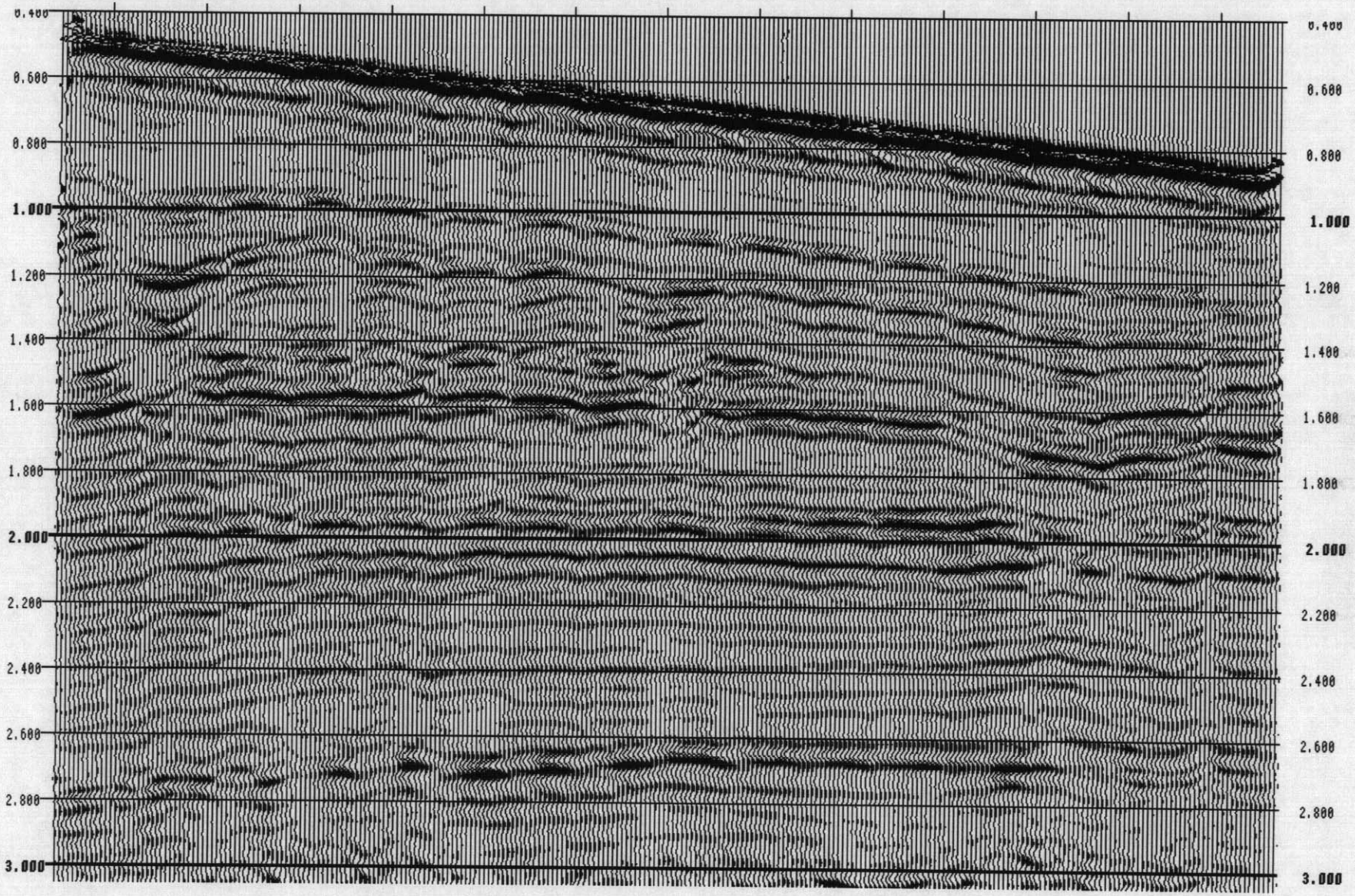

Figure 40. PS data from Ram Powell processed to enhance the shallow section.

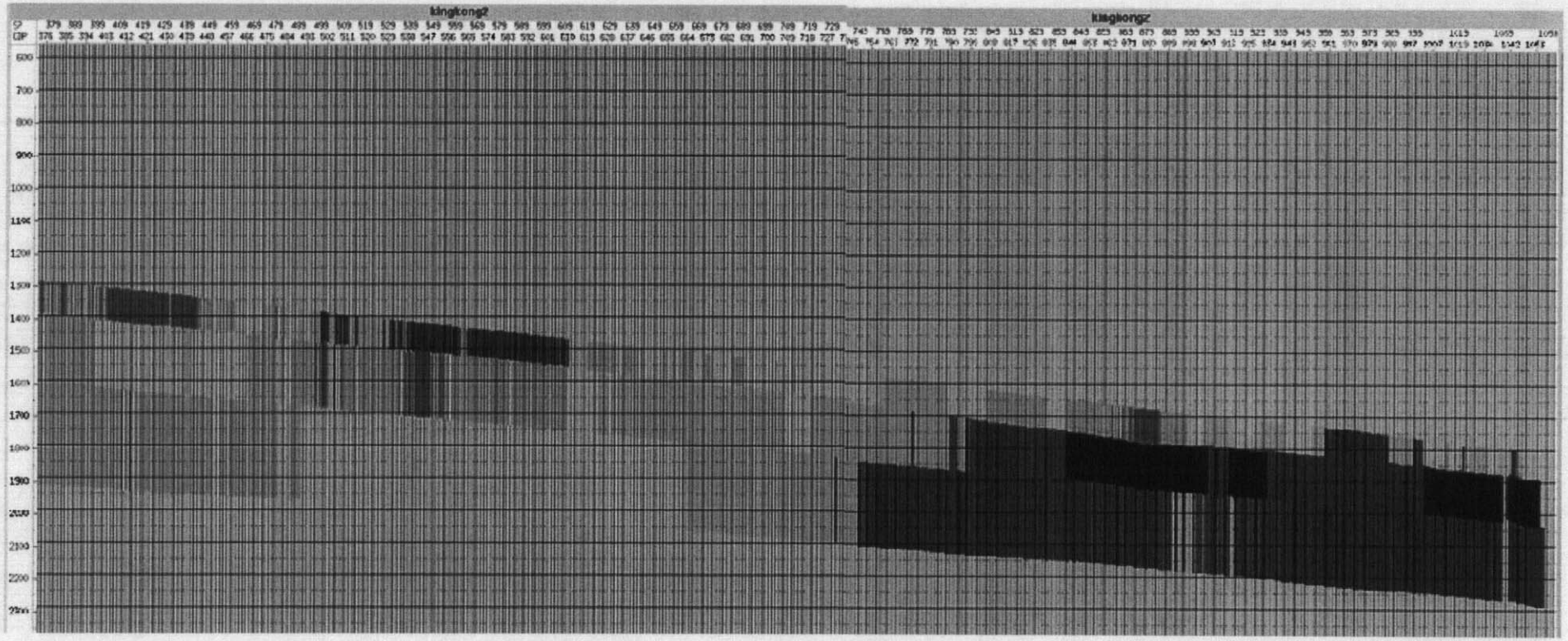

Figure 41. Deviation from mean Vp/Vs ratios (red = higher Vp/Vs) for the Ram Powell area. Notice the correlation between Vp/Vs and water depth suggesting pore pressure control.

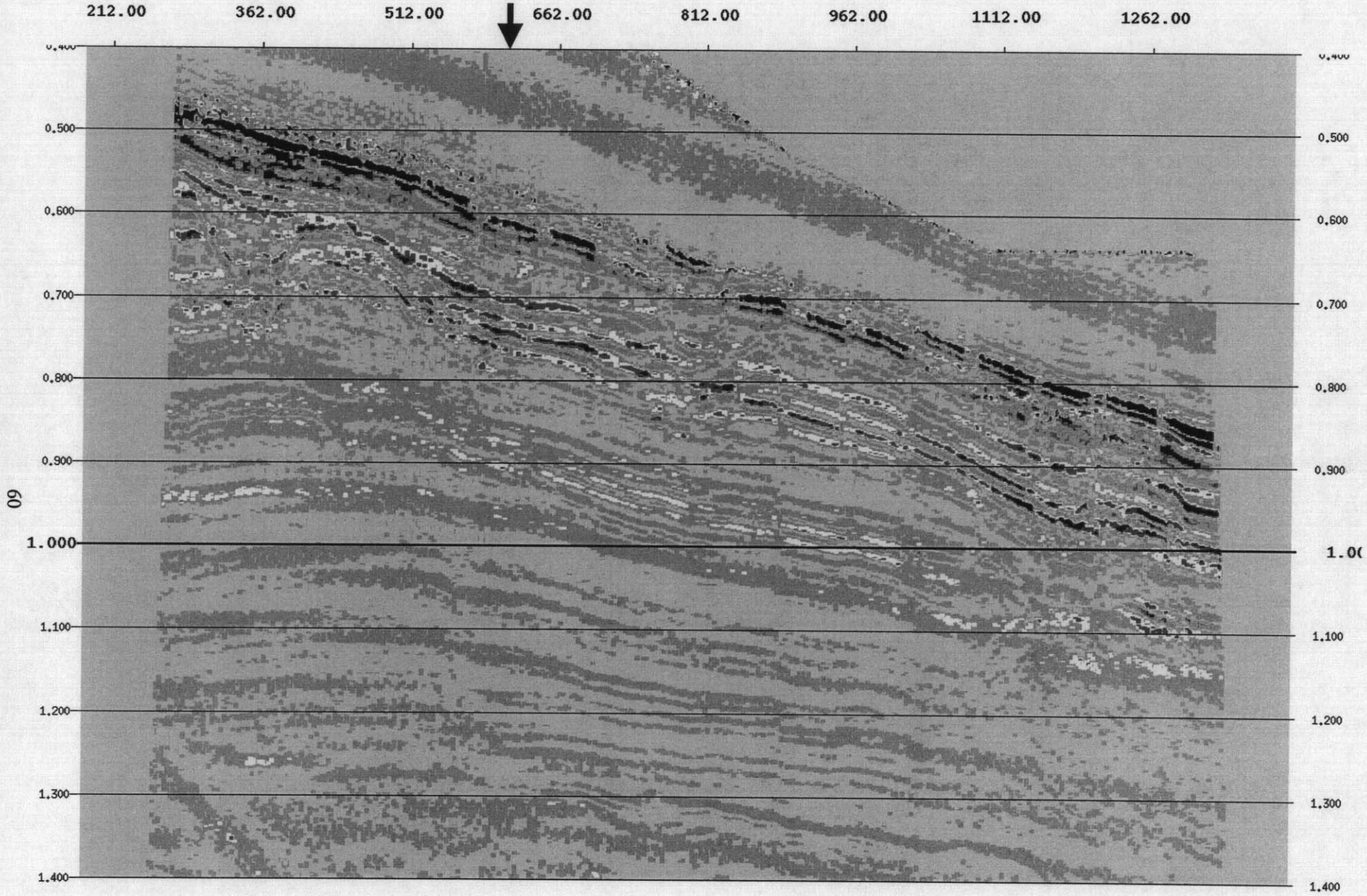

Figure 42. FFAVA plot of Ram Powell p-p data. The vertical arrow points to Well #912-1 location. The FFAVA anomalies are mainly confined to the shallow section. Note a shallow channel (~ 0.6 sec) near the left edge of the line.

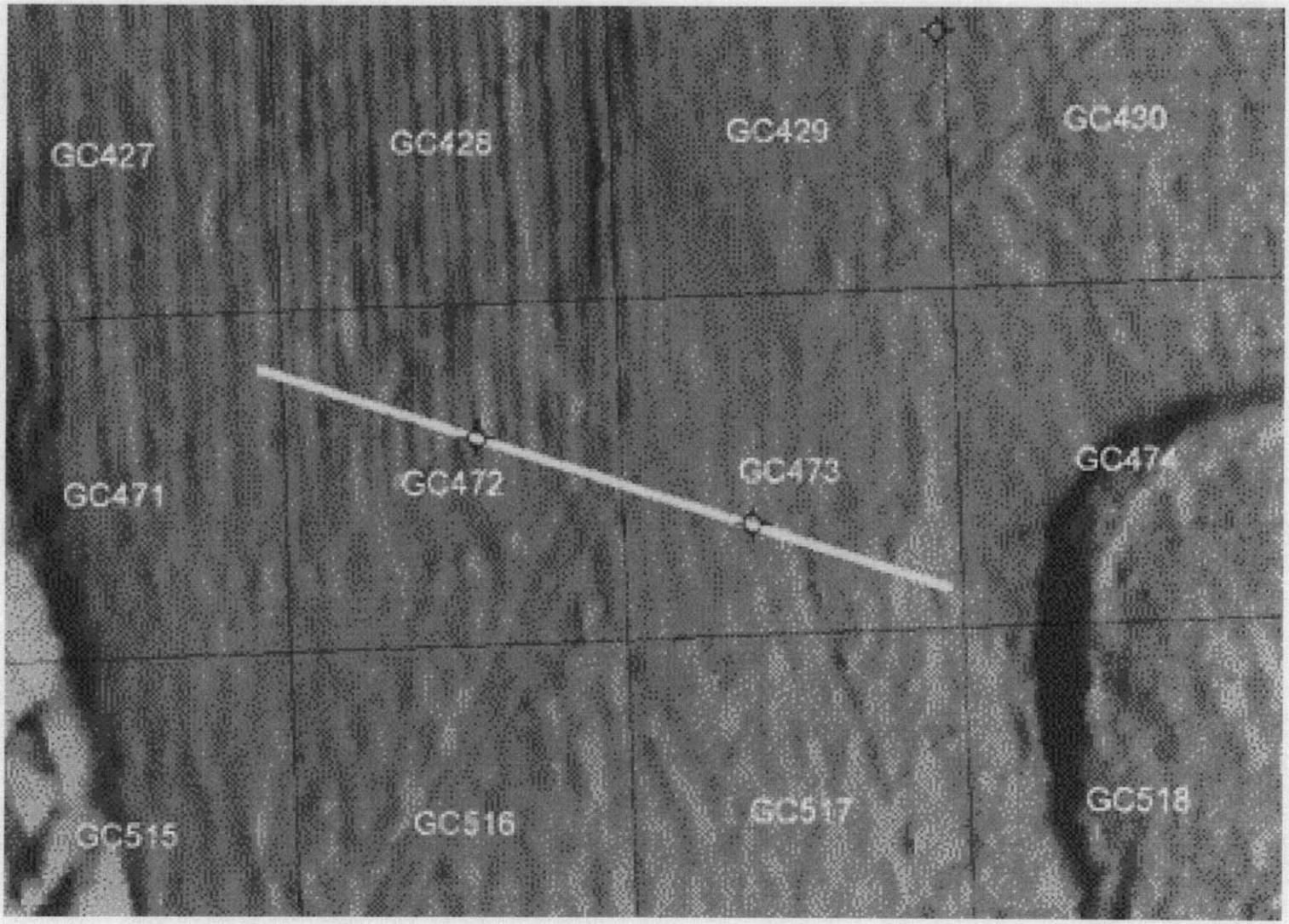

Figure 43. Location of the PGS multicomponent line in the King Kong area.

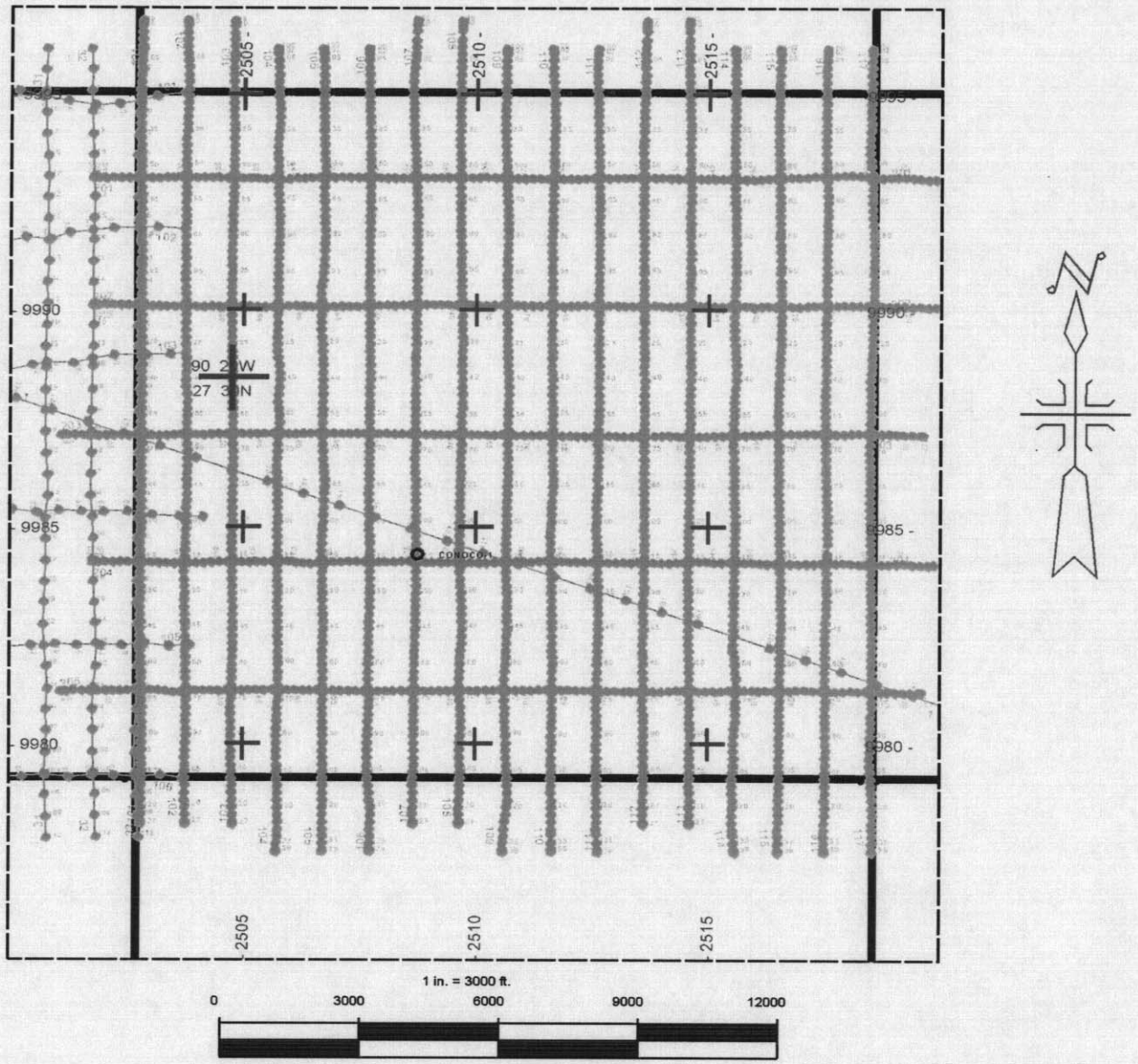

Figure 44. Map showing the location of hazard survey lines in Green Canyon Block 473. The NW-SE trending line is the PGS multicomponent line.

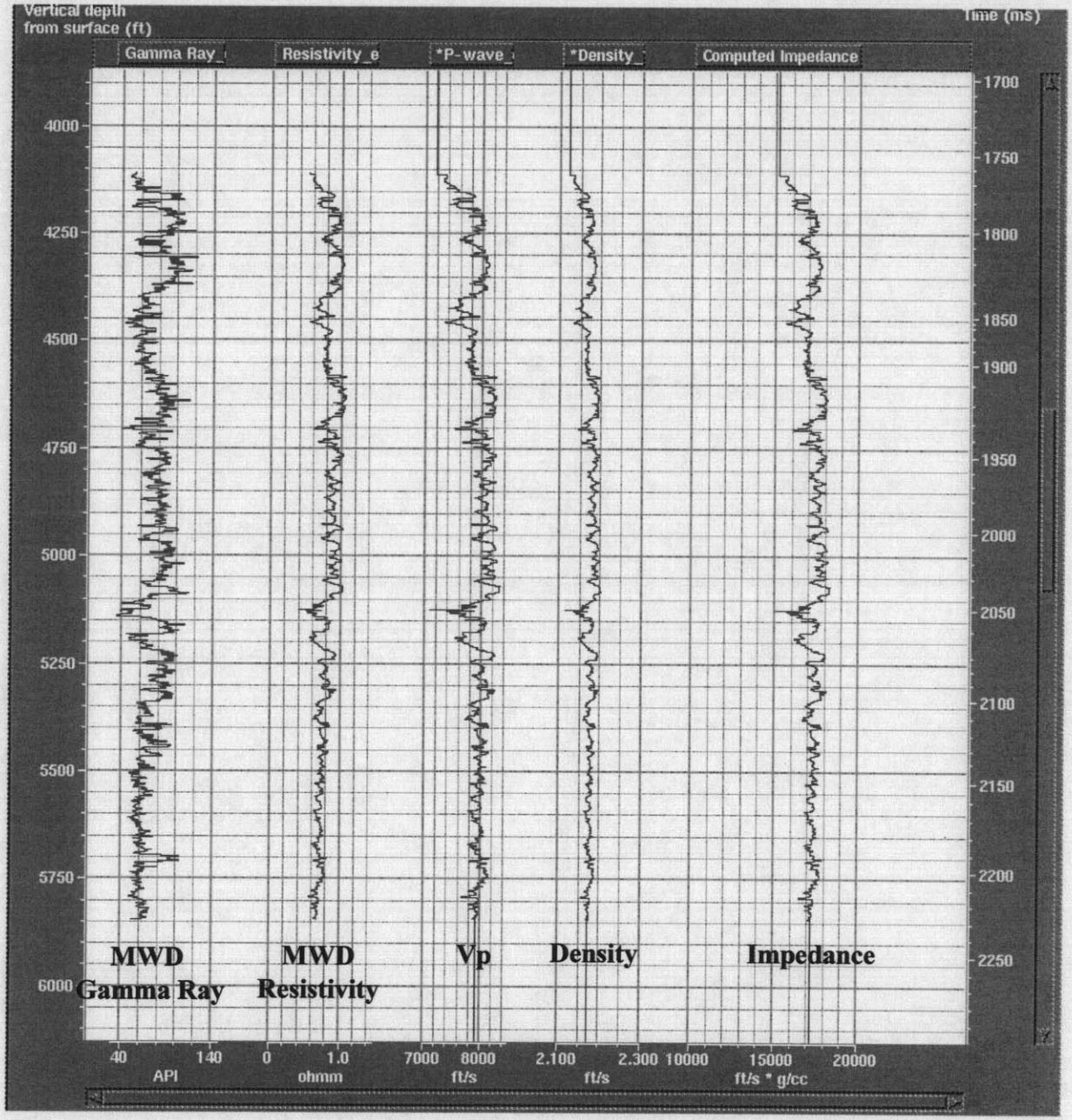

Figure 45. GC 473-1 MWD logs and calculated Vp, density, and impedance logs.

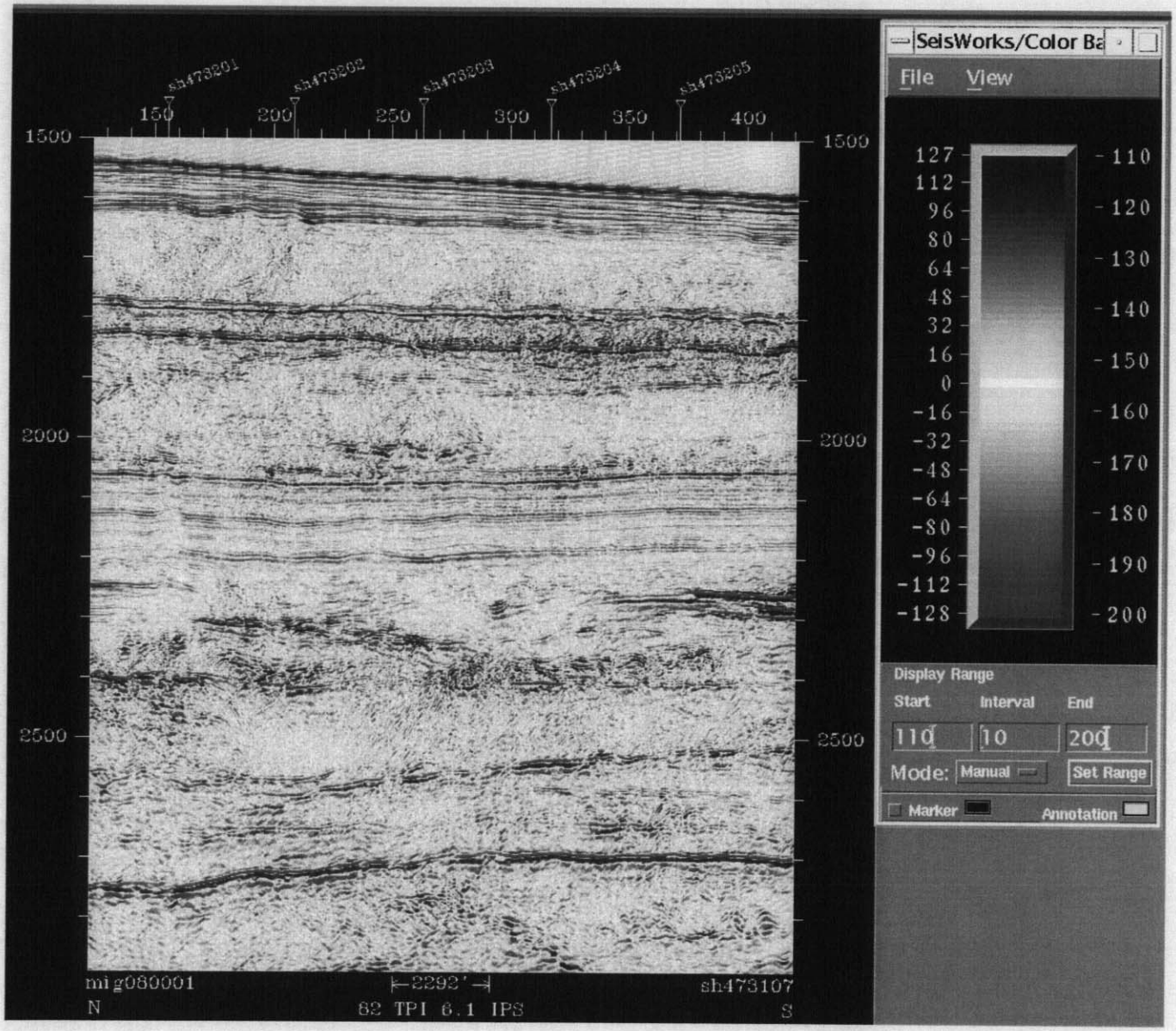

Figure 46. Shallow Hazard 2D Seismic Inline 107.

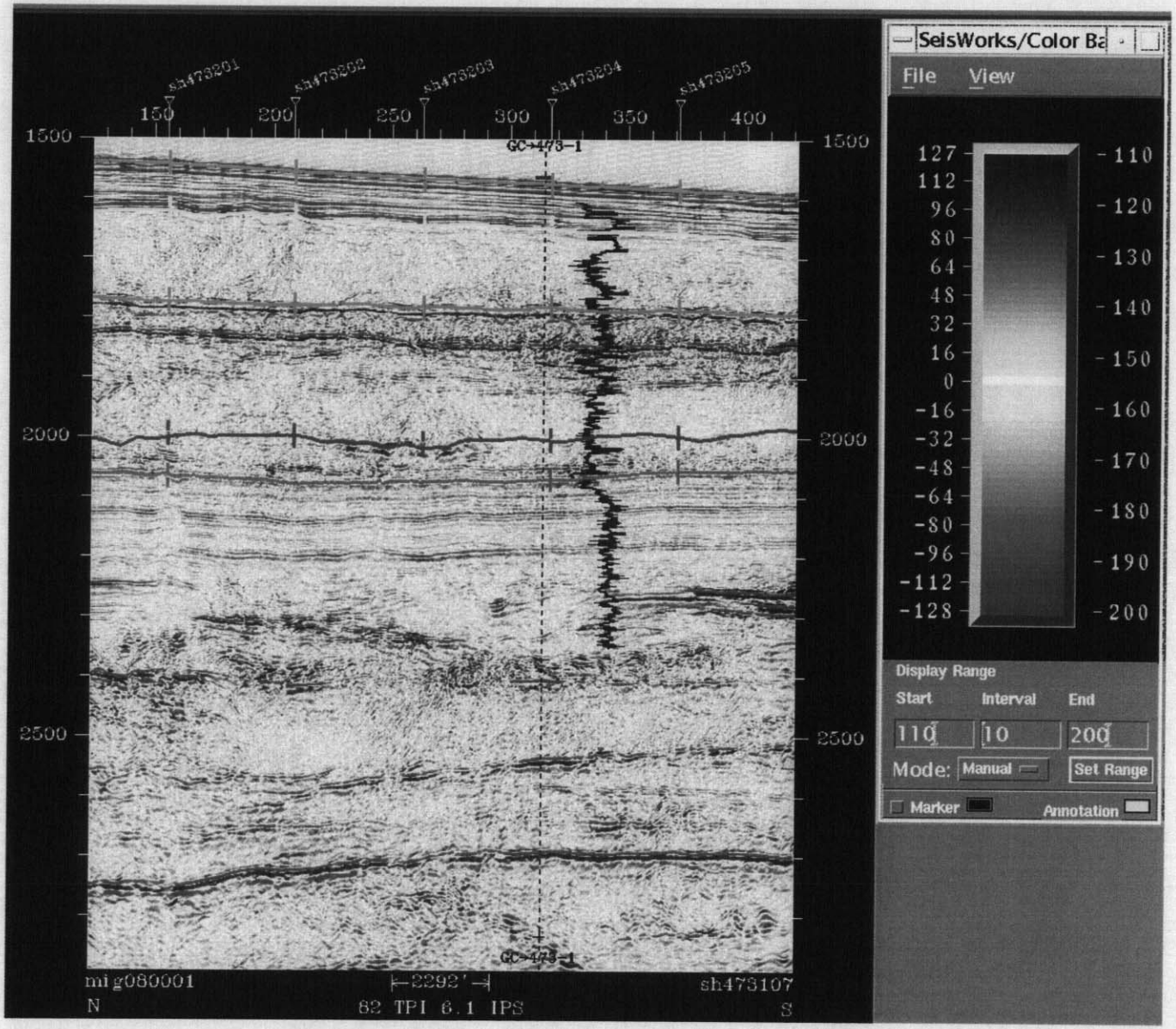

Figure 47. Interpreted Inline 107 with GC 473-1 MWD Gamma Ray Log.

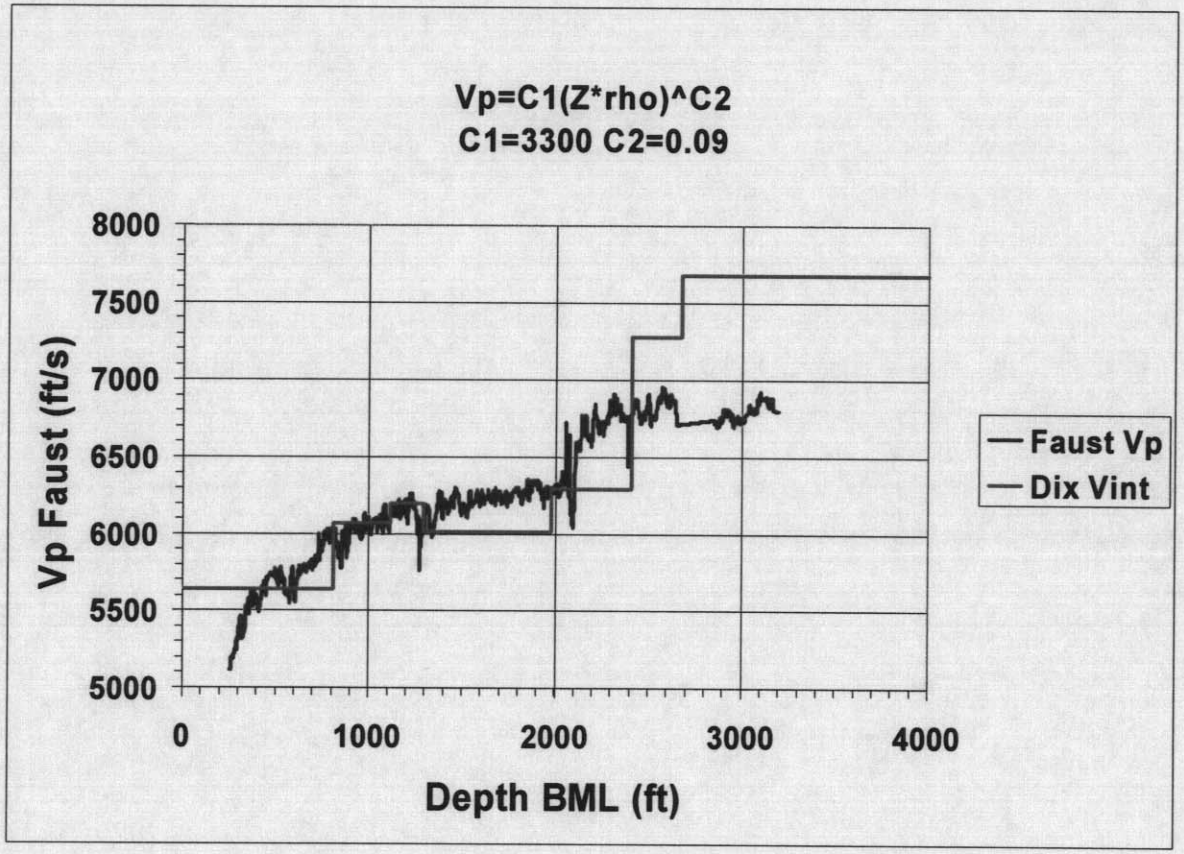

Figure 48. GC473#1 Faust Sonic: Calculated Vp derived from MWD Resistivity Log and Calibrated to Seismic Stacking Velocities.

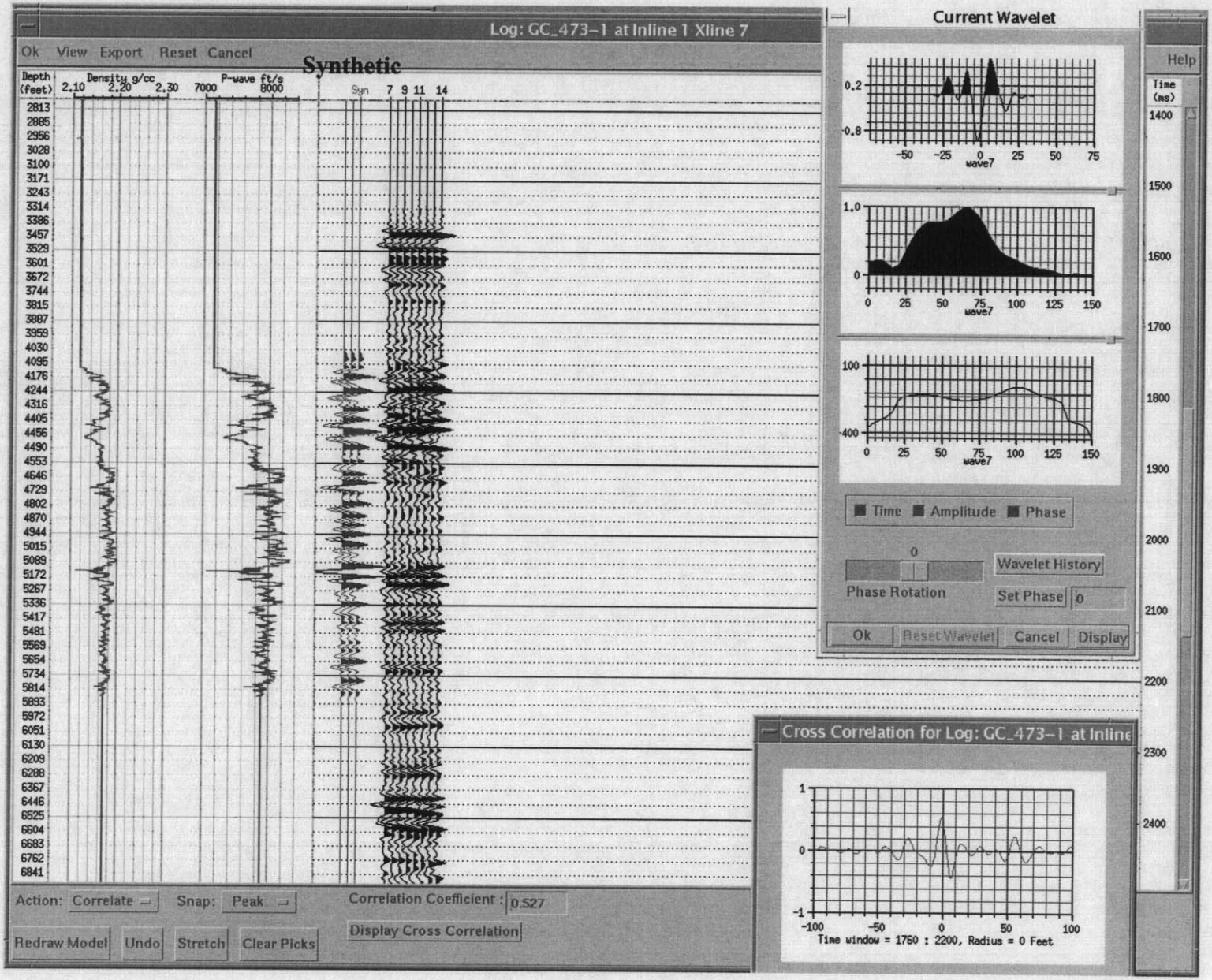

Figure 49. GC 473-1 well tie with shallow hazard seismic data.

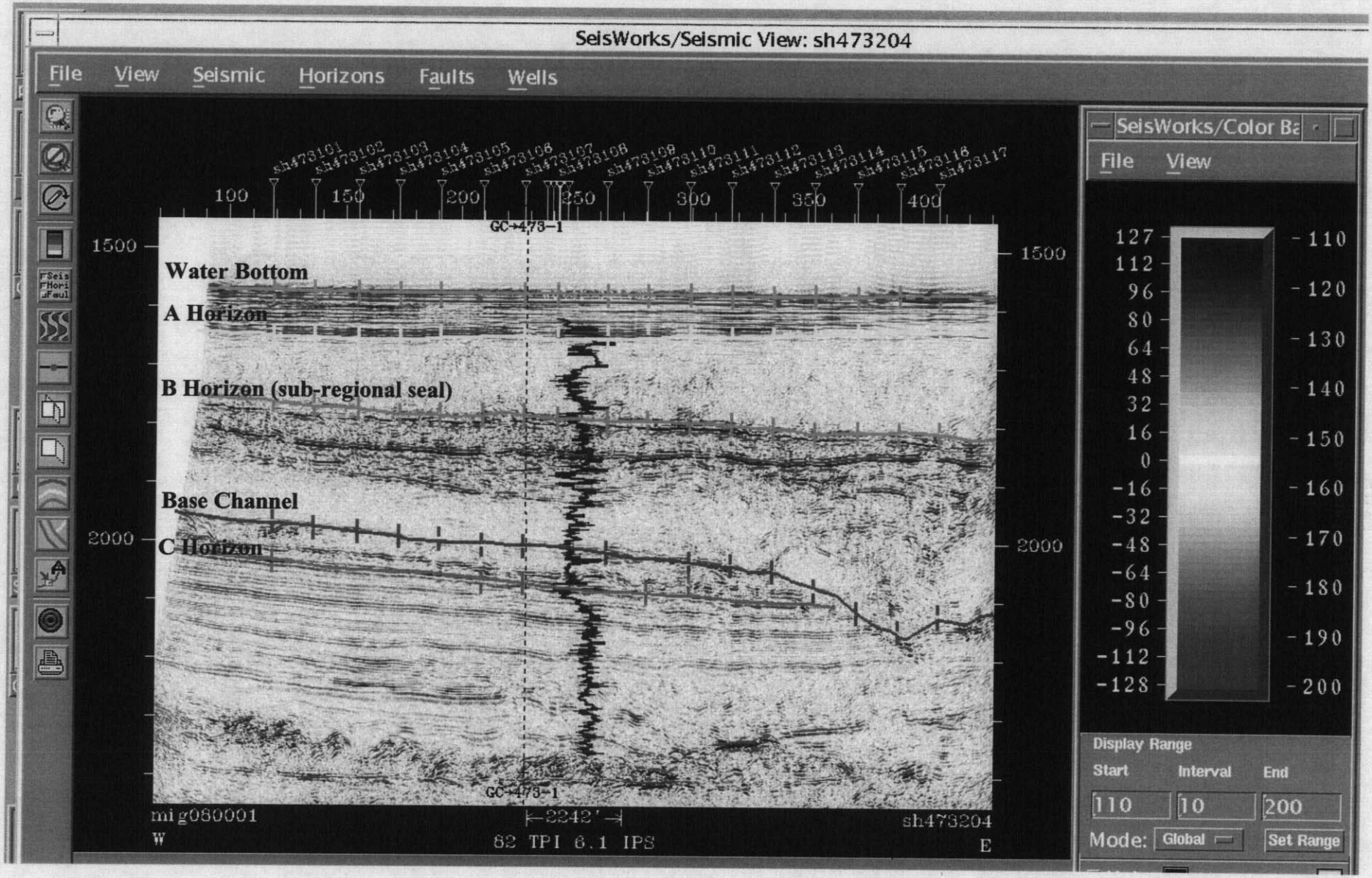

Figure 50. Interpreted Crossline 204 with GC 473-1 MWD Gamma Ray Log.

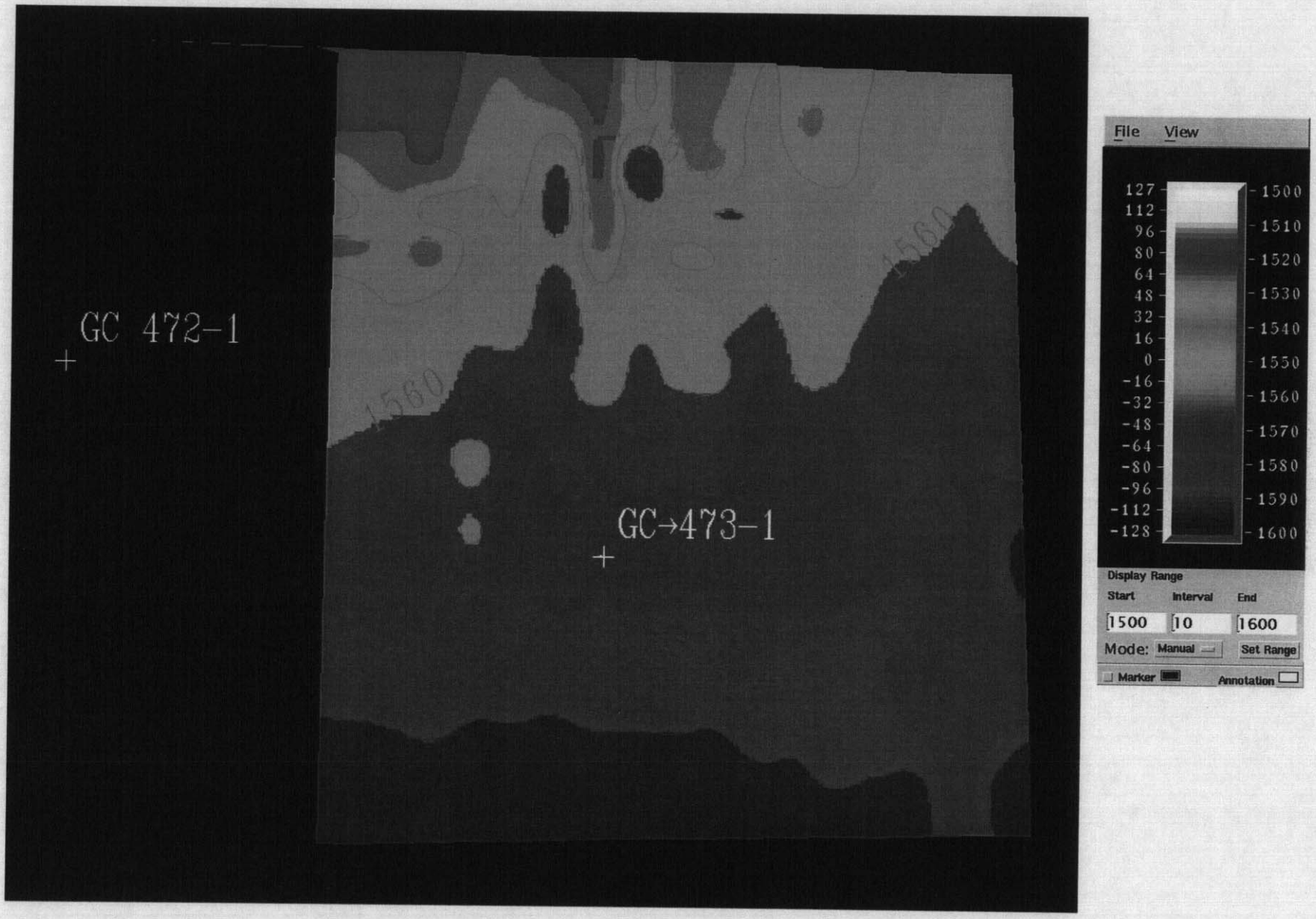

Figure 51. Water Bottom Time Structure Map for the King Kong area.

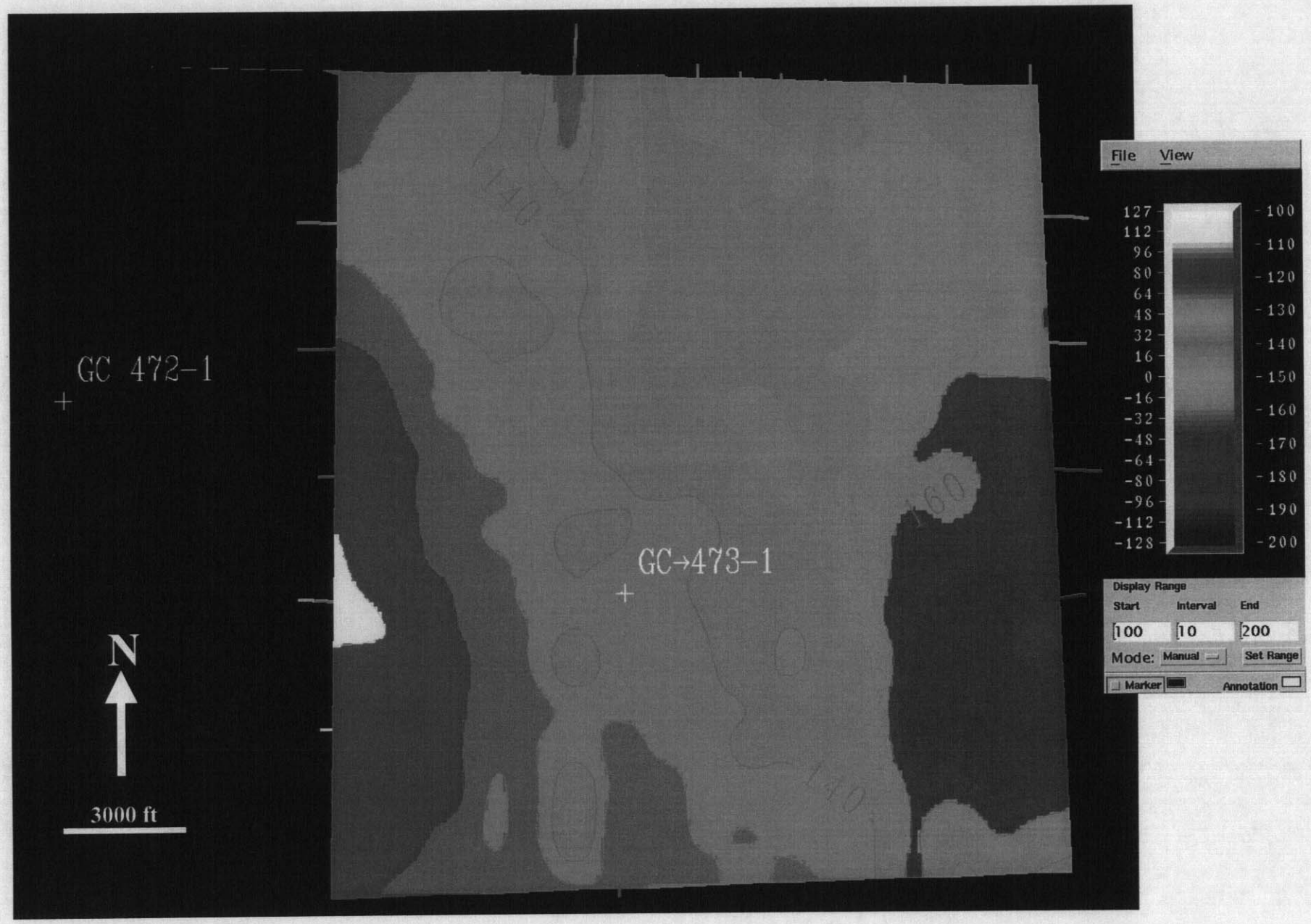

Figure 52. Isochron map of interval between B and A Horizons.

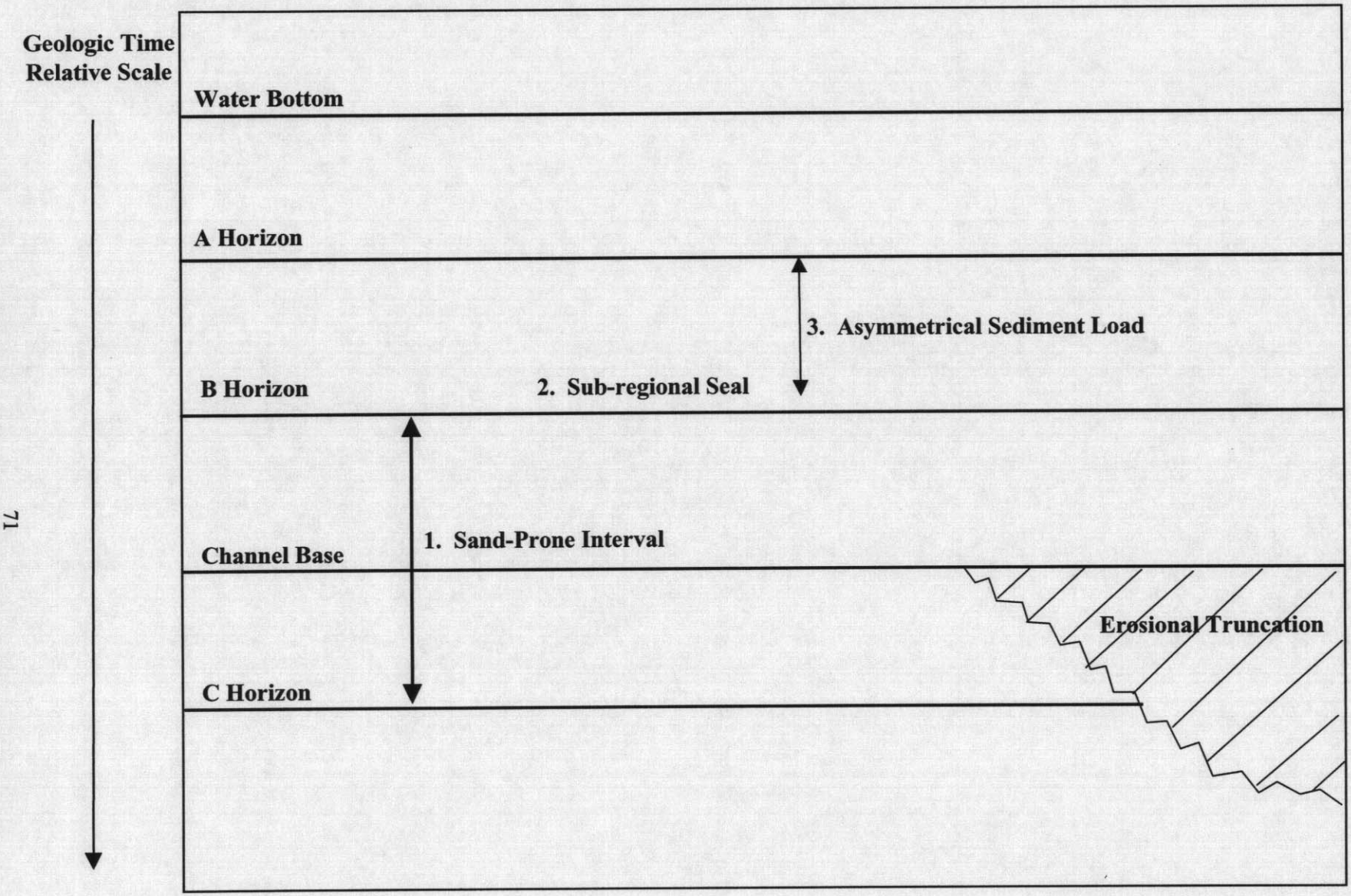

Figure 53. Schematic Chronostratigraphic Relationship Between Key SWF Components (Crossline 204).

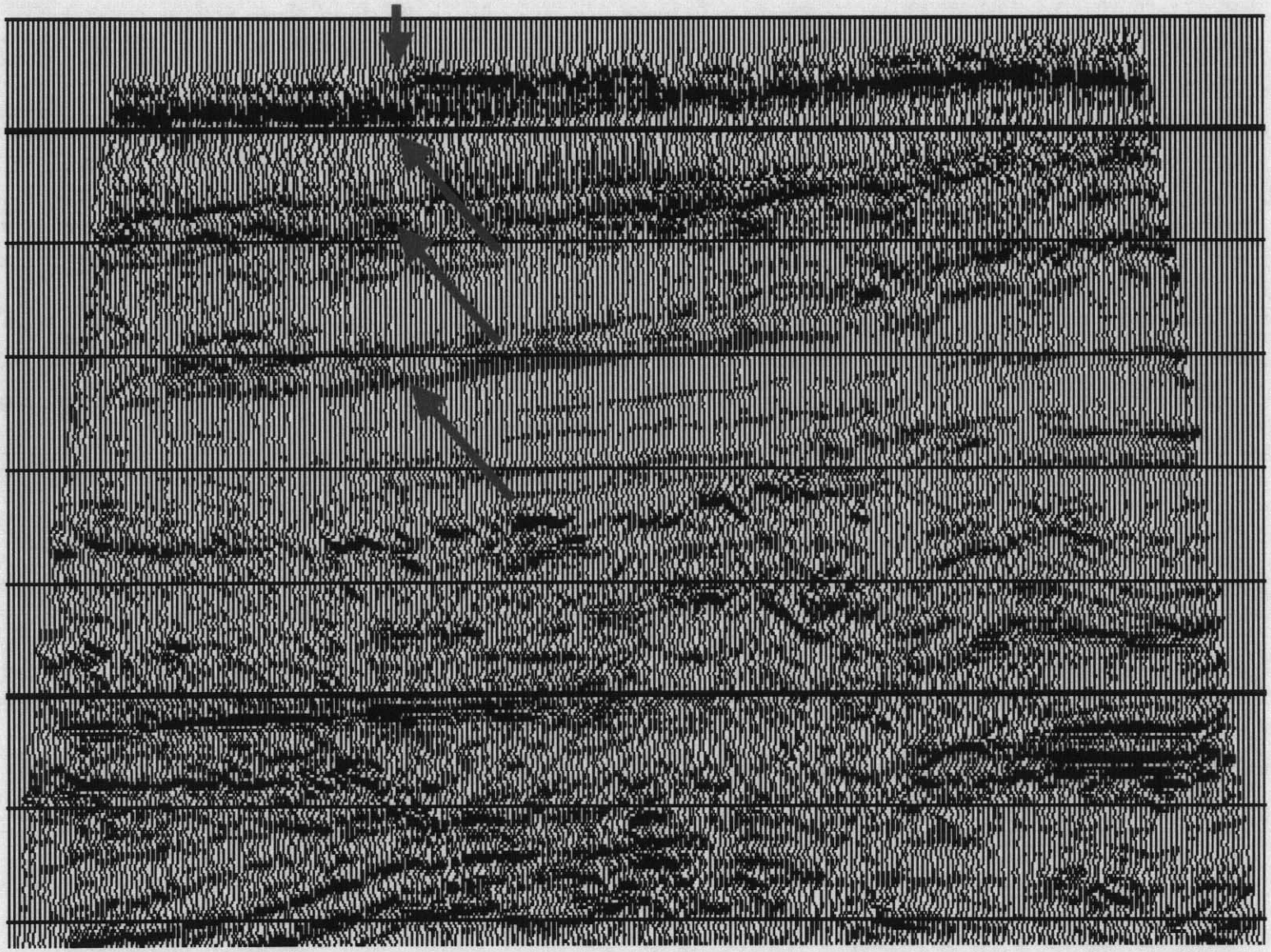

Figure 54. PP data from the King Kong area. The vertical arrow points to the well location. The slanting arrows point to equivalent horizons on the PS data shown in Figure 55.

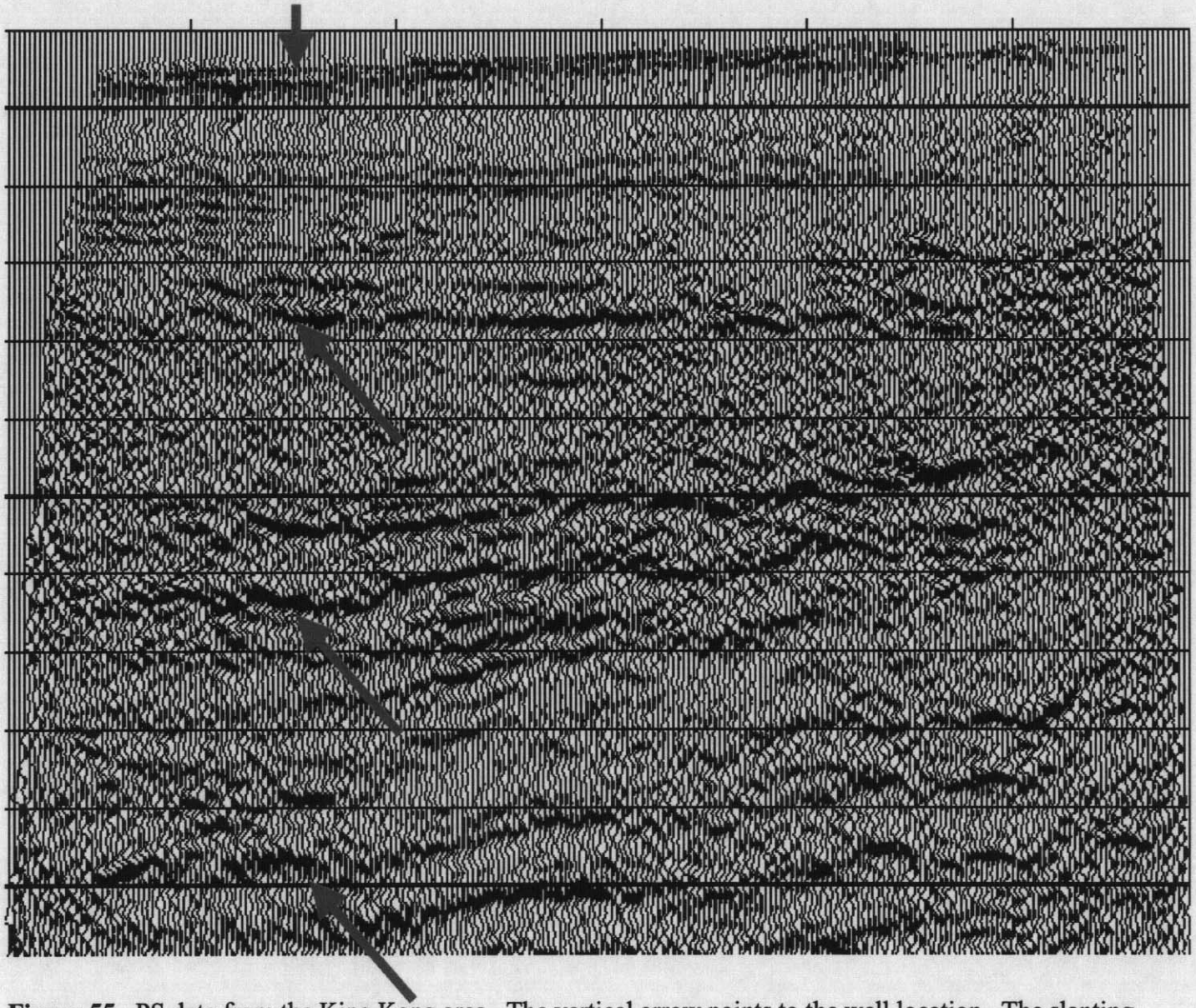

Figure 55. PS data from the King Kong area. The vertical arrow points to the well location. The slanting arrows point to equivalent horizons on the PP data shown in Figure 54.

Figure 56. PP data from King Kong processed to enhance the shallow section.

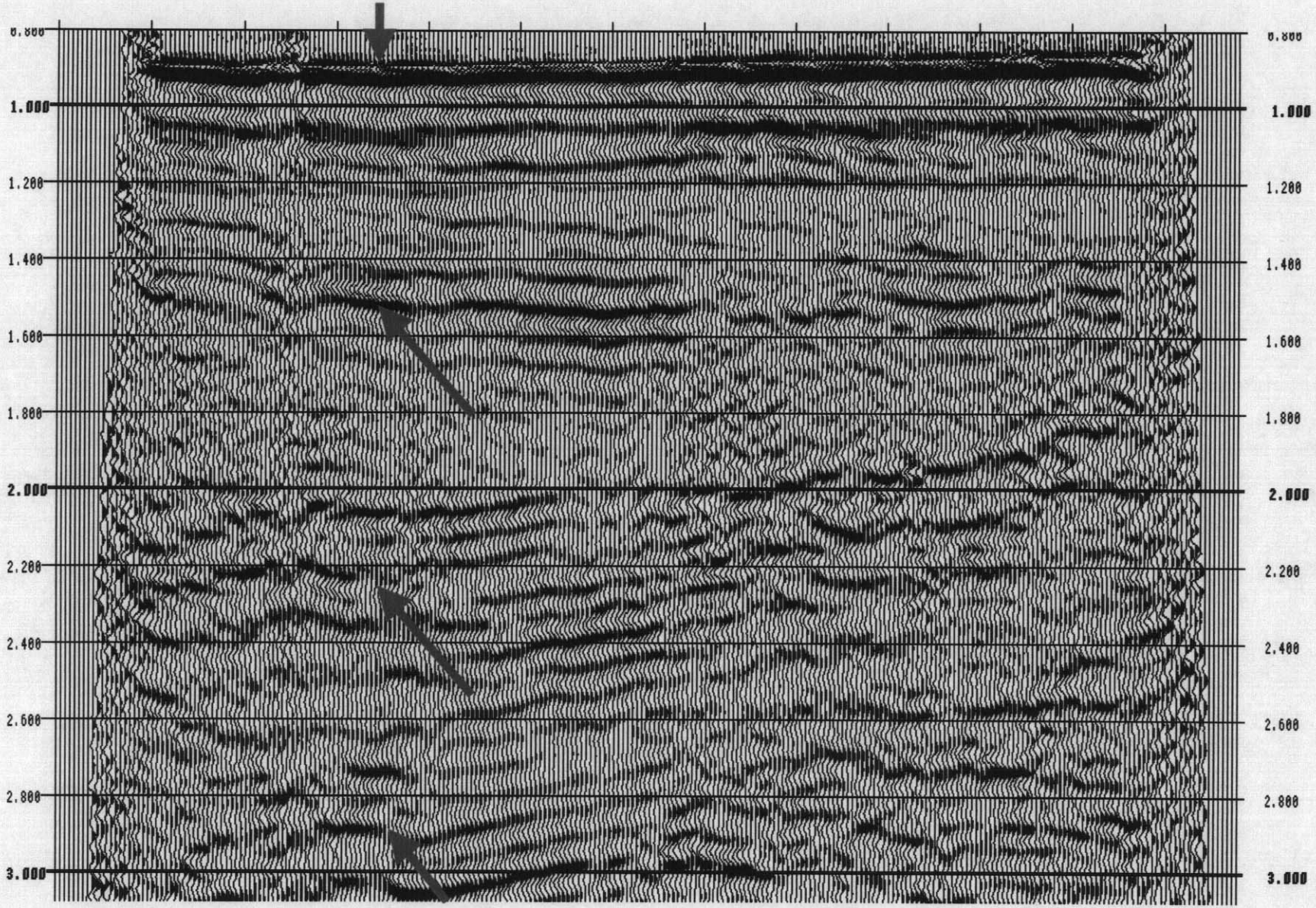

Figure 57. PS data from King Kong processed to enhance the shallow section.

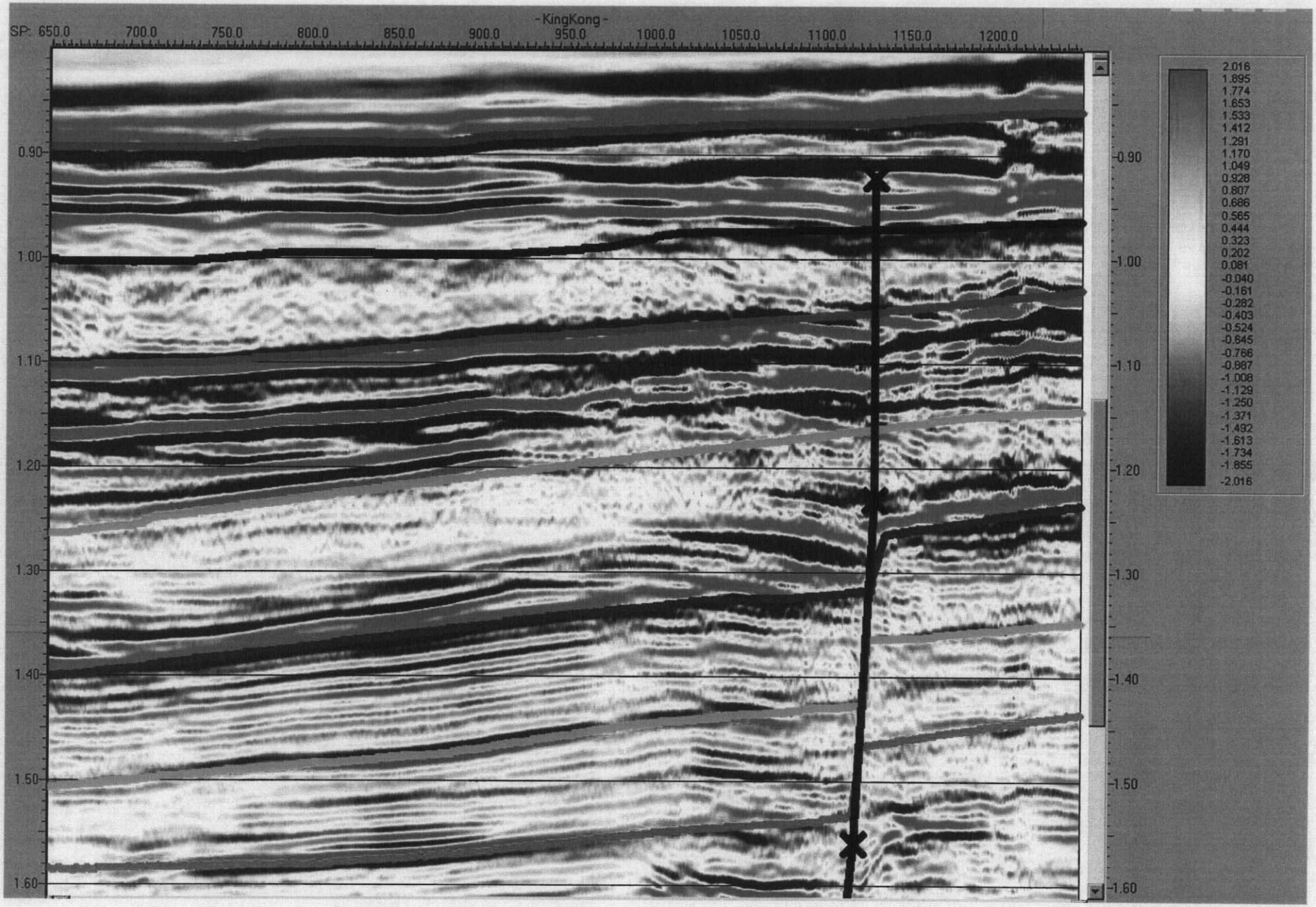

Figure 58. King Kong stacked PP section. Solid lines are correlated horizons.

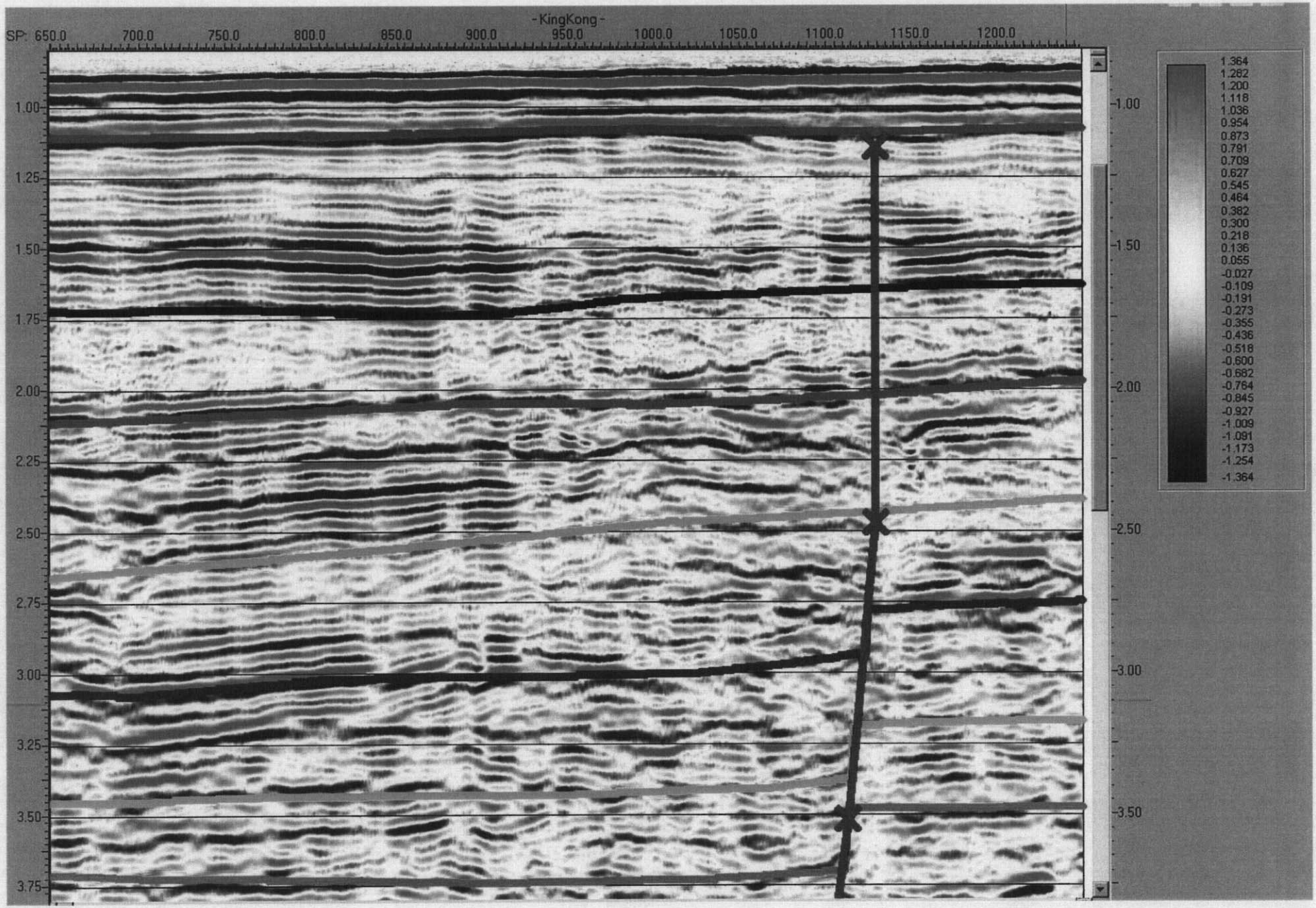

Figure 59. Stacked PS section. Colored lines correspond to horizons of the same color picked on the PP section assuming events are correlated properly.

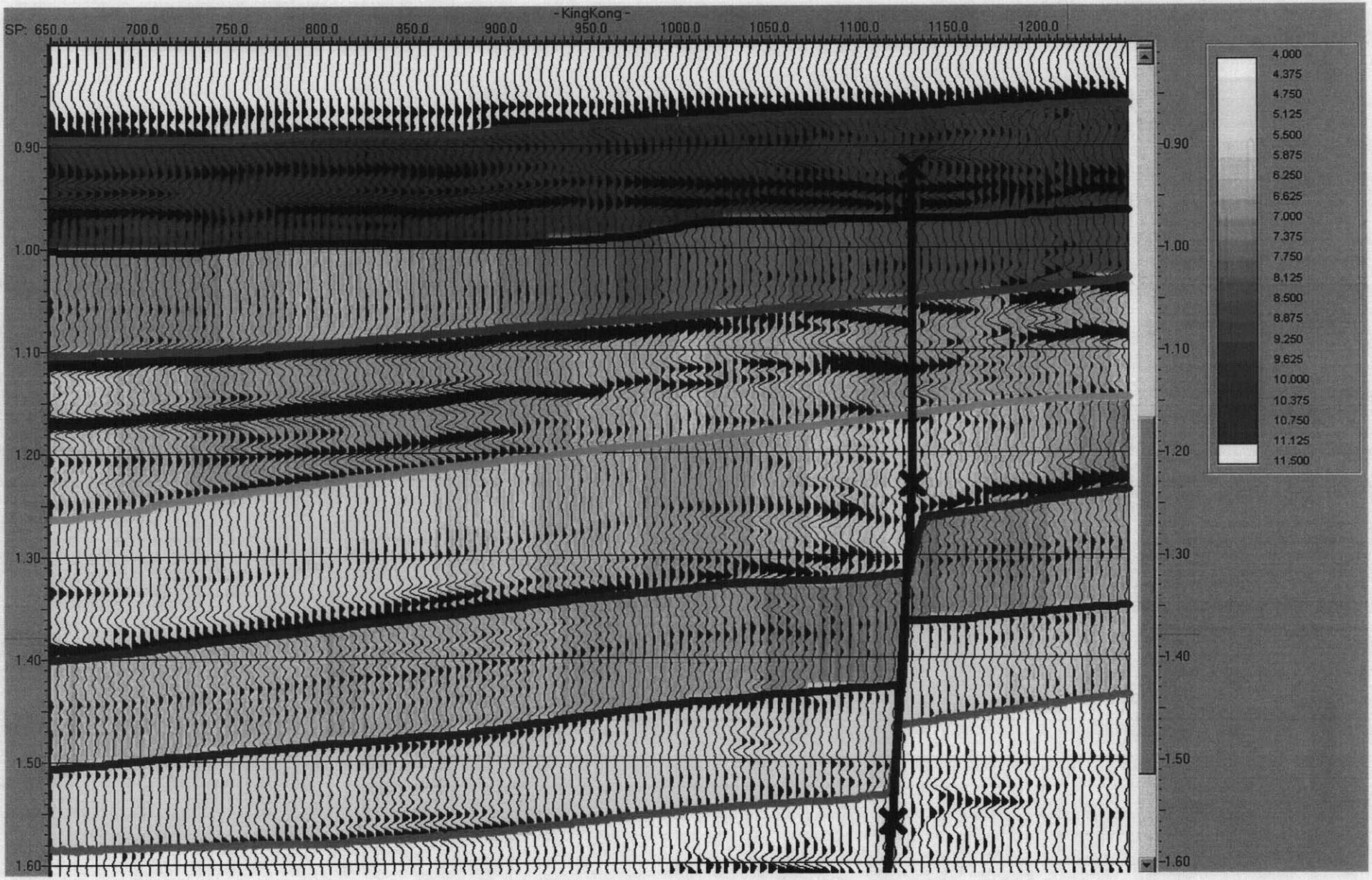

Figure 60. King Kong measured Vp/VS ratios from PP and P-S travel times represented in color overlain on the wiggle trace PP section. Vp/VS is very high (over 10) near the water bottom and decreases rapidly with increasing depth.

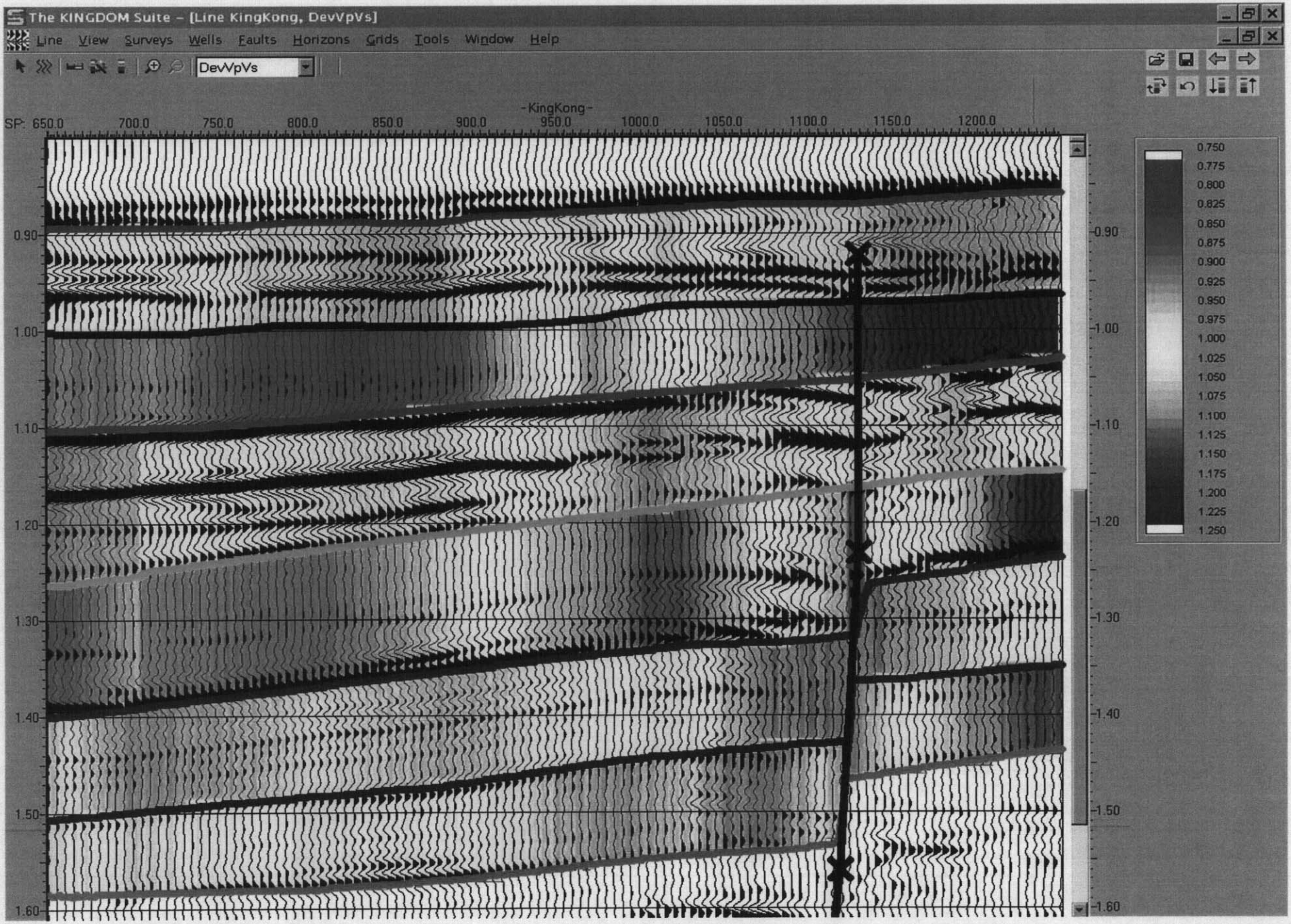

Figure 61. Fractional deviation from mean Vp/Vs for each interval, visually enhancing Vp/Vs anomalies.

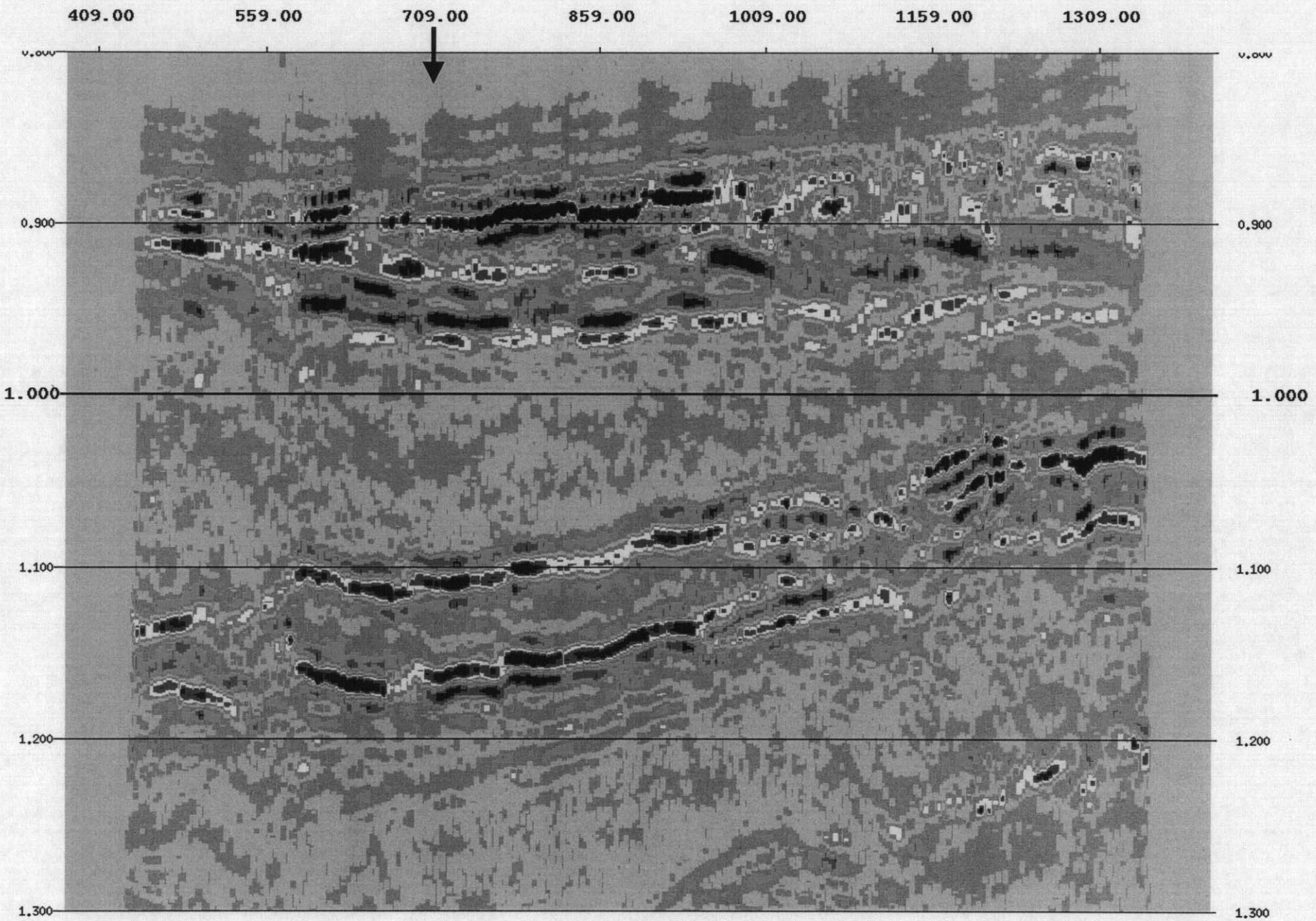

Figure 62. FFAVA plot of King Kong p-p data. The blue and red colors represent -ve and +ve anomalies, respectively. The vertical arrow shows the location of Well #473-1 which encountered a minor SWF.

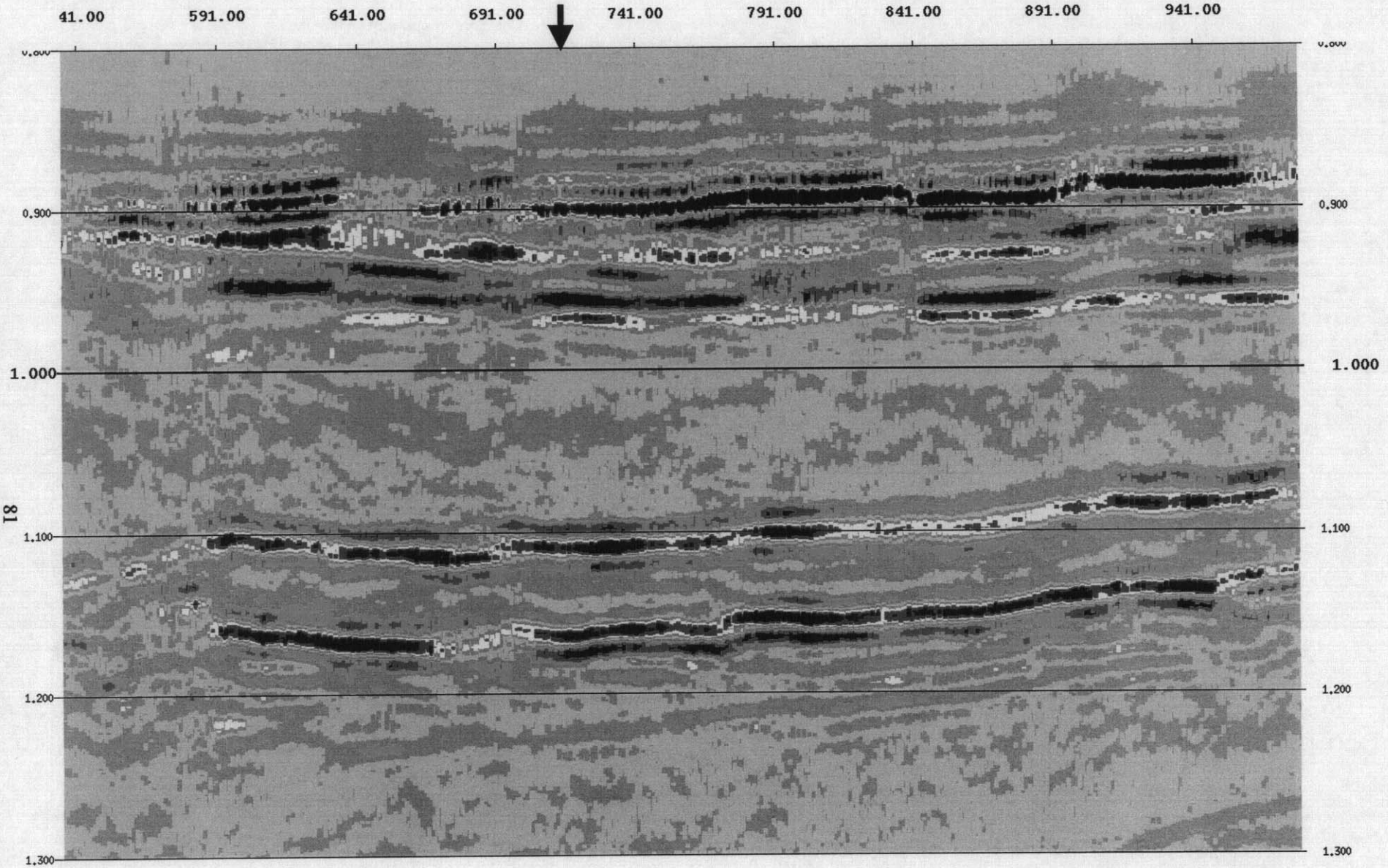

Figure 63. An expanded version of Figure 62. It shows the FFAVA anomalies more clearly in the potential SWF zones (0.86-0.98 sec and 1.07-1.17 sec intervals).

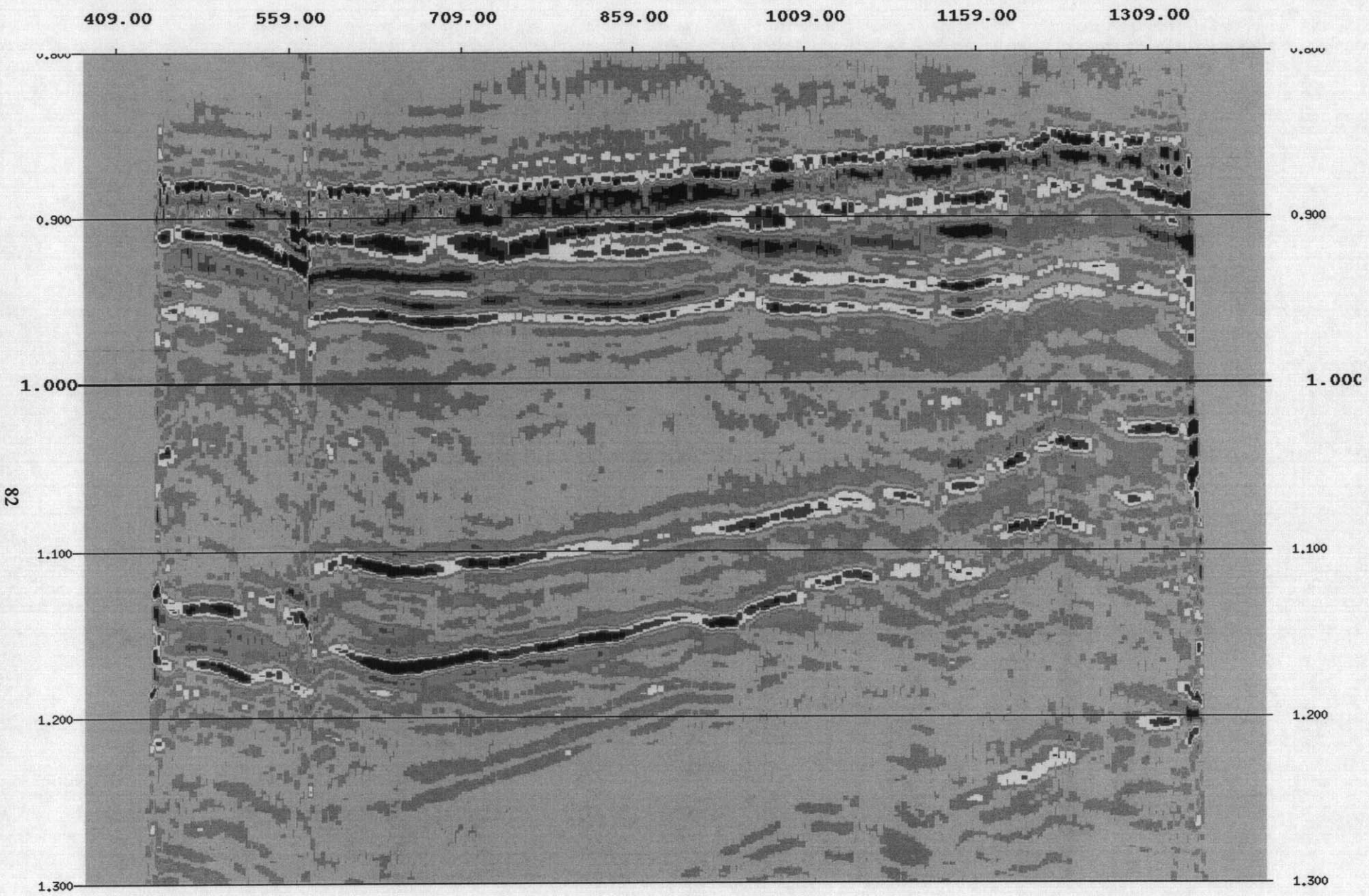

Figure 64. Zero-offset reflectivity plot of King Kong p-p data. The blue and red colors represent -ve and +ve reflectivity, respectively.

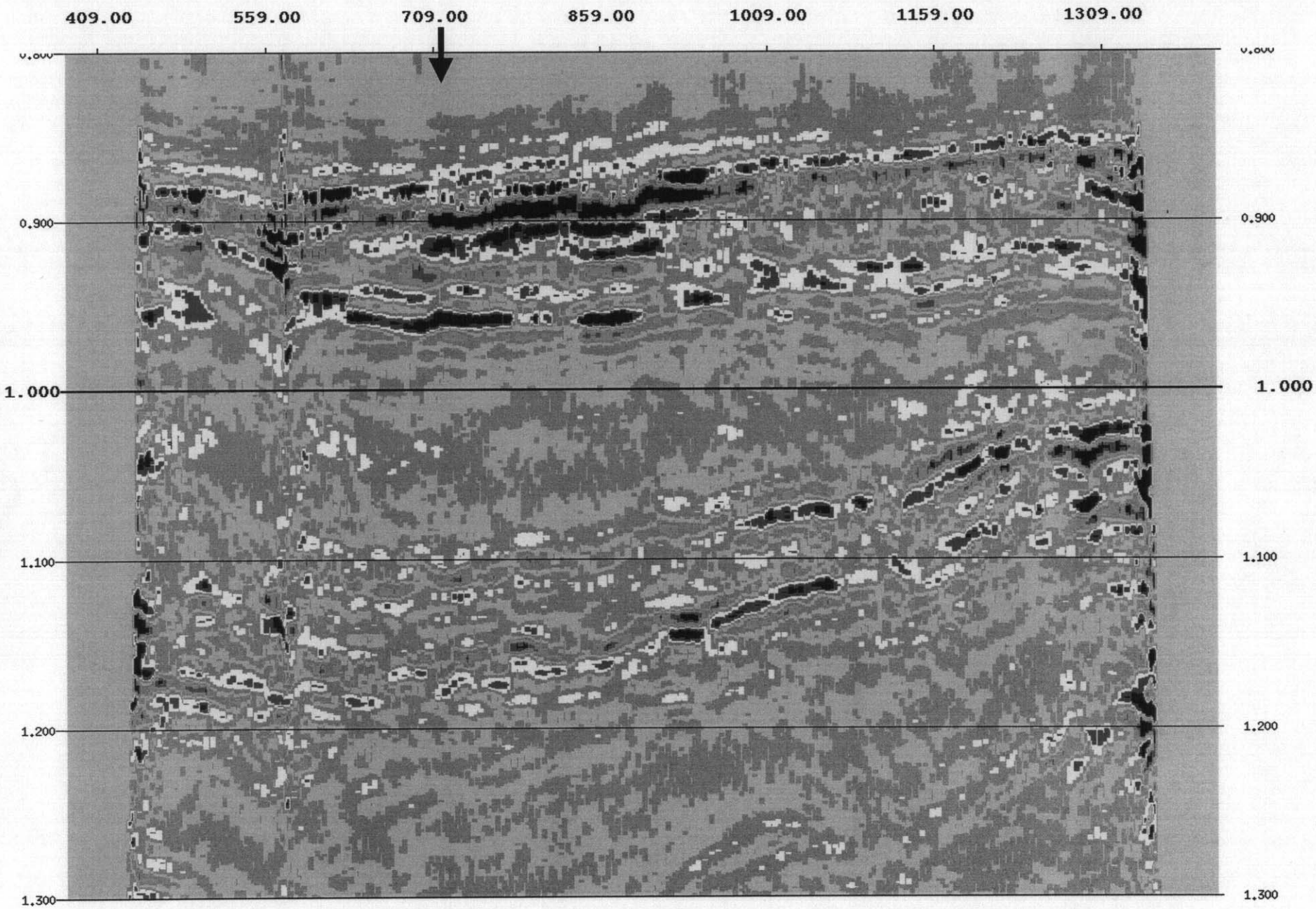

Figure 65. Plot of relative changes in Poisson's ratio for the King Kong p-p data. The blue colors represent Poisson's ratio greater than the background while the red colors represent values smaller than the background. A potential SWF zone extends from cdp numbers 700 to 950. Well #473-1 (vertical arrow) projects at cdp number 712.

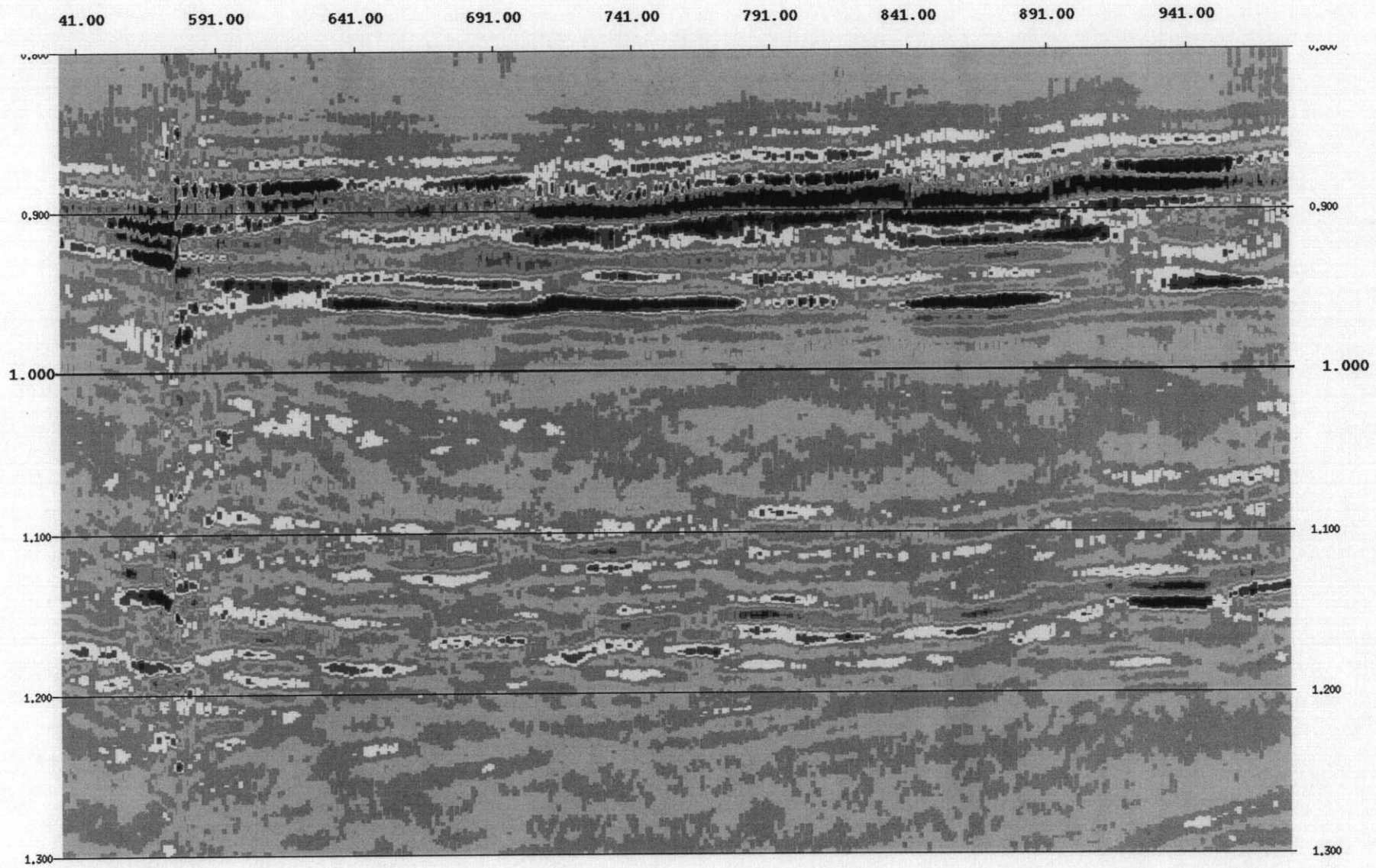

Figure 66. Expanded version of Figure 65. Note the absence of Poisson's ratio anomalies in the deeper sand package (1.07-1.17 sec).